

**Density Functional Studies of the Structure,
Properties and Applications of Copper and Iron
Complexes of 3,7-Diazabicyclo[3.3.1]nonane
Derivatives**

**INAUGURAL - DISSERTATION
zur
Erlangung der Doktorwürde
der
Naturwissenschaftlich-Mathematischen Gesamtfakultät
der
Ruprecht-Karls-Universität Heidelberg**

**vorgelegt von
Heidi Rohwer
aus Empangeni, Südafrika**

2006

INAUGURAL - DISSERTATION
zur
Erlangung der Doktorwürde
der
Naturwissenschaftlich-Mathematischen Gesamtfakultät
der
Ruprecht-Karls-Universität Heidelberg

vorgelegt von
Heidi Rohwer
aus Empangeni, Südafrika

2006

Tag der mündlichen Prüfung: 02.06.2006

**Density Functional Studies of the Structure,
Properties and Applications of Copper and Iron
Complexes of 3,7-Diazabicyclo[3.3.1]nonane
Derivatives**

Gutachter: Prof. Dr. Peter Comba
Dr. Katja Heinze

“Models are to be used, not believed”

paraphrased by H. Thiel in “Principles of Econometrics”

THANKS TO ...

Prof. Dr. Peter Comba, for the interesting subject material and the valuable discussions

Marlies von Schoenbeck-Schilli and Karin Stelzer, for taking care of all the technical details of my time at the University of Heidelberg

Present and past members of the Comba group, in particular *Bodo Martin, Marion Kerscher, Jochen Bautz, Karin Born, Andre Daubinet, Mate Tarnai, Rajaraman Gopalan and Mihail Atanisov*, for the scientific collaboration and the good work atmosphere

Members of the Graduate College 850, in particular the *members of the Organisational Committee 2004*, for an insight into other areas of research and an enjoyable three years

My father, my mother, my brother and my two sisters, for their love and support

My two grandmothers, for constantly reminding me of what is really important in life

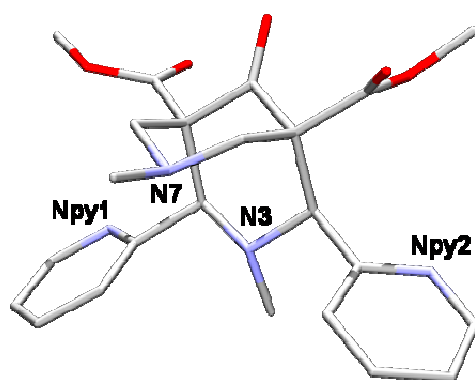
Family Lopez, for providing a home away from home

... and last but not least ...

Carlos Lopez de Laorden, for everything

Abstract

The 3,7-diazabicyclo[3.3.1]nonane (bispidine) derivatives are characterised by a highly rigid backbone, but an elastic coordination sphere. They are therefore able to coordinate a wide range of transition metals, while at the same time enforcing specific geometries in the corresponding complexes, and are particularly well suited for the coordination of the biologically relevant metals copper and iron. The main aim of this work was the application of density functional theory to the calculation of the structure, properties and applications of copper and iron complexes of 3,7-diazabicyclo[3.3.1]nonane derivatives.



The structure of the tetradentate bispidine ligand N₂py₂ (L¹)

A brief overview of the basic concepts important in bispidine coordination chemistry, as well as a discussion of the properties of substituted bispidine ligands and their corresponding metal complexes, is given in Chapter 1.

The first part of this work, Chapters 2 and 3, deals with the isomerism observed in the copper(I) and copper(II) complexes of a range of substituted bispidine derivatives based on L¹ above. The copper(I) complexes demonstrate structural isomerism of the metal centre, whereas for the copper(II) complexes various “Jahn-Teller” isomers have been isolated. The relative energies of the different geometric forms of the copper(I) complexes are shown to be dependent on the position of substitution on the pyridine ring (*ortho* or *meta*) and/or the size of the *ortho* substituent, and can be related to the stability of the corresponding oxidation products. The “Jahn-Teller” isomerism observed in the copper(II) complexes can also be

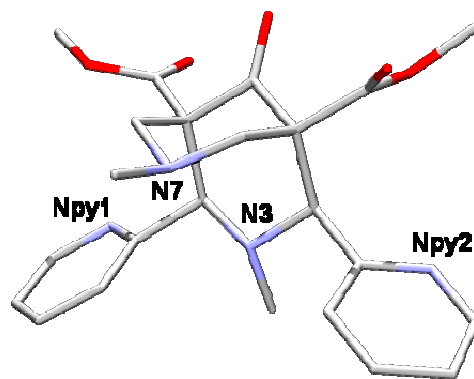
controlled by directed *ortho* substitution on the pyridine rings and by changing the size, electronic nature and denticity of the co-ligand.

Also in Chapter 3, the electronic structure of the copper(II) chloro complexes of tetradentate bispidines is examined more closely, in order to better understand the specific geometries enforced by the ligand backbone and how these geometries influence the reactivity of the corresponding complexes. In addition, the shortcomings of density functional theory in calculating the structures and properties of copper(II) bispidine complexes are addressed and a hybrid density functional approach is applied to help overcome these deficiencies.

The second part of this work deals with the application of the iron(II) bispidine complexes in the catalytic epoxidation and dihydroxylation of olefins in the presence of H_2O_2 . In Chapter 4, a computational study of possible mechanisms for the reaction of the iron(II) complex of L^1 with H_2O_2 in acetonitrile is undertaken. A mechanism based on the formation of Fe^{IV} -dihydroxo and Fe^{IV} -oxo intermediates is proposed, which is in agreement with the available experimental results for the catalysis. In Chapters 5 and 6, the electronic nature of the biologically relevant Fe^{IV} -oxo and Fe-O_2 complexes of tetradentate and pentadentate bispidine derivatives is explored. Significant results include the calculation of high-spin ground states for the Fe^{IV} -oxo complexes of tetradentate bispidines and the location of low-spin end-on local minima for hexacoordinate Fe-O_2 complexes of bispidine ligands, which are best described as Fe^{II} -superoxo species.

Zusammenfassung

Die 3,7-Diazabicyclo[3.3.1]nonan (Bispidin) Derivate verfügen über ein starres Ligandgerüst, weisen jedoch eine elastische Koordinationssphäre auf. Daher sind sie in der Lage, eine Reihe verschiedener Übergangsmetalle zu komplexieren, wobei spezifische Geometrien für die entsprechenden Koordinationsverbindungen erzwungen werden. Besondere Beachtung finden hierbei verschiedene Komplexe der biologisch relevanten Metalle Kupfer und Eisen. Das Hauptziel der vorliegenden Arbeit war die Berechnung von Strukturen and Eigenschaften von Kupfer- und Eisenkomplexen diverser 3,7-Diazabicyclo[3.3.1]nonan Derivate mittels Dichtefunktionaltheorie, um so auf mögliche Anwendungen zu schließen.



Die Struktur des vierzähligen Bispidin-Liganden N2py2 (L^1)

Ein kurzer Überblick sowohl über grundlegende Konzepte der Koordinationschemie mit Bispidinliganden, als auch über die Eigenschaften substituierter Bispidine und ihrer entsprechende Metalkomplexe, wird in Kapitel 1 gegeben.

Im ersten Teil dieser Arbeit (Kapitel 2 and 3) werden die bei Kupfer(I)- und Kupfer(II)-Komplexen mit einer Reihe substituierter Bispidin-Derivate (basierend auf L^1 , siehe oben) beobachteten Isomeren diskutiert. Während für die Kupfer(I)-Komplexe strukturelle Isomerie des Metalzentrums erkennbar ist, können bei den Kupfer(II)-Komplexen verschiedene "Jahn-Teller-Isomere" isoliert werden. Die relativen Energien der Kupfer(I)-Verbindungen mit unterschiedlichen Geometrien erweisen sich als abhängig von der Substituentenposition am Pyridinring (*ortho* oder *meta*) und/oder der Größe des *ortho*-

Substituenten und können mit der Stabilität der entsprechenden oxidierten Spezies korreliert werden. Die "Jahn-Teller-Isomerie" der Kupfer(II)-Komplexe lässt sich einerseits durch gezielte *ortho*-Substitution der Pyridinringe, andererseits durch eine Veränderung der Größe, der elektronischen Eigenschaften und der Zähigkeit des Kolliganden kontrollieren.

Um ein besseres Verständnis der spezifischen, vom Ligandengerüst erzwungenen Geometrien zu bekommen, und wie diese Geometrien Rückschlüsse auf die Reaktivität der entsprechenden Komplexe zulassen, wird auch in Kapitel 3 anhand der elektronischen Struktur von Kupfer(II)-Chloro-Komplexen mit vierzähligen Bispidinen genauer untersucht. Außerdem werden die Schwächen der Dichtefunktionaltheorie bei der Berechnung von Strukturen und Eigenschaften der Kupfer(II)-Verbindungen aufgezeigt und es wird die Möglichkeit angesprochen, diese Defizite durch die Anwendung von modifizierten Hybridfunktionalen zu negieren.

Gegenstand der Betrachtung im zweiten Teil dieser Arbeit ist die Anwendung von Eisen(II)-Bispidin-Komplexen in der katalytischen Oxidation von Olefinen mit Wasserstoffperoxid. Basierend auf DFT-Rechnungen werden in Kapitel 4 Untersuchungen zu möglichen Mechanismen der Reaktion von Eisen(II)-Komplexen mit L^1 , mit H_2O_2 angestellt. In Übereinstimmung mit experimentellen Ergebnissen wird ein Mechanismus postuliert, welcher auf der Bildung Fe^{IV} -dihydroxo- und Fe^{IV} -oxo-Intermediaten beruht. In den Kapiteln 5 und 6 werden die elektronischen Eigenschaften von biologisch relevanten Fe^{IV} -oxo- und FeO_2 -Komplexen von vier- und fünfzähligen Bispidin-Derivaten analysiert. Herausragende Ergebnisse hierbei waren zum Einen die Berechnung eines high-spin Grundzustandes für Fe^{IV} -oxo-Komplexe mit vierzähligen Bispidinen, zum Anderen das Auftreten eines lokalen Minimums für low-spin end-on hexacoordinierte FeO_2 -Komplexe mit Bispidin-Liganden, welche demnach eher als Fe^{II} -superoxo-Spezies definiert werden können.

Abbreviations

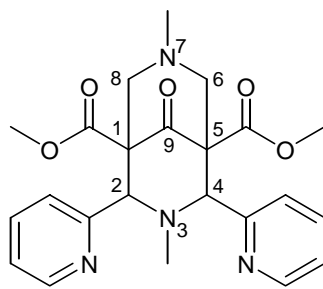
bispidine	3,7-diazabicyclo[3.3.1]nonane
DFT	Density Functional Theory
SP	Single Point
PCM	Polarised Continuum Model
PES	Potential Energy Surface
MPA	Mulliken Population Analysis
EDA	Energy Decomposition Analysis
TS	Transition State
RO	Restricted Open-shell
HF	Hartree-Fock
COSMO	Conductor-like Screening Model
MO	Molecular Orbital
EPR	Electron Paramagnetic Resonance
NMR	Nuclear Magnetic Resonance
UV-Vis	Ultraviolet-Visible
BLM	Bleomycin
ABLM	Activated Bleomycin
TPA	tris(2-pyridylmethyl)amine
N4py	<i>N,N</i> -bis(2-pyridylmethyl)- <i>N</i> -bis(2-pyridyl)methylamine
BPMEN	<i>N,N'</i> -dimethyl- <i>N,N'</i> -bis(pyridylmethyl)-1,2-diaminoethane
TPMEN	<i>N</i> -methyl- <i>N,N',N'</i> -tris(2-pyridylmethyl)-1,2-diaminoethane
MMO	Methane Monooxygenase
TauD	Taurine Dioxygenase
TMC	1,4,8,11-tetramethyl-1,4,8,11-tetraazacyclotetradecane
CCSD(T)	Coupled Cluster with Single, Double and Triple excitations
EXAFS	Extended X-ray Absorption Fine Structure
EDTA	Ethylenediaminetetraacetic acid
py	pyridine
ac	acetonitrile
ar	aromatic

Table of Contents

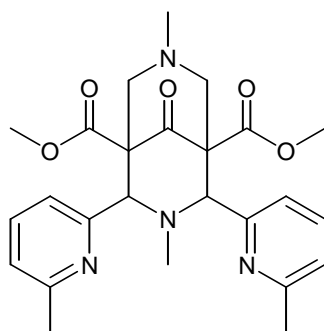
1. Introduction	1
1.1. References	6
2. Structural Isomerism in the Copper(I) Complexes of tetradentate 3,7-Diazabicyclo[3.3.1]nonane Derivatives	9
2.1. Introduction	9
2.2. Computational Methods	13
2.3. Results and Discussion	14
2.4. Conclusion	20
2.5. References	22
3. The Copper(II) Complexes of tetradentate 3,7-Diazabicyclo[3.3.1]nonane Derivatives: Isomerism, Electronic Structure and Spin Density Distribution	25
3.1. Introduction	25
3.2. Computational Methods	29
3.3. Results and Discussion	32
3.3.1. Geometries, isomerism and substrate binding strengths	32
3.3.2. Electronic structure of the $[\text{Cu}(\text{L})(\text{Cl})]^+$ complexes	45
3.3.3. Calibration of the DFT functional	48
3.4. Conclusion	58
3.5. References	60
4. A Mechanistic Study of the Reaction with H_2O_2 of the Iron(II) Complex of a tetradentate 3,7-Diazabicyclo[3.3.1]nonane Derivative	63
4.1. Introduction	63
4.2. Computational Methods	69
4.3. Results and Discussion	70
4.3.1. Preliminary calculations on $\text{L}^{\text{I}}\text{Fe}^{\text{II}}$ and H_2O_2	70
4.3.2. Primary Intermediate $[\text{L}^{\text{I}}\text{Fe}^{\text{II}}(\text{HOOH})(\text{CH}_3\text{CN})]^{2+}$	72
4.3.3. The Fe^{III} -hydroperoxo – Fe^{V} -oxo-hydroxo pathway (A)	75
4.3.4. The Fe^{IV} -dihydroxo – Fe^{IV} -oxo-aqua pathway (B)	81
4.3.5. The Fe^{II} -hydroperoxo – Fe^{IV} -oxo-hydroxo pathway (C)	88
4.4. Conclusion	95
4.5. References	97

5. The Electronic Structure of the Oxoiron(IV) Complexes of tetra- and pentadentate 3,7-Diazabicyclo[3.3.1]nonane Derivatives	101
5.1. Introduction	101
5.2. Computational Methods	104
5.3. Results and Discussion	106
5.4. Conclusion	116
5.5. References	117
6. The Electronic Nature of the Iron(III)-hydroperoxo and Iron(III)-peroxo Complexes of 3,7-Diazabicyclo[3.3.1]nonane Derivatives	121
6.1. Introduction	121
6.2. Computational Methods	123
6.3. Results and Discussion	124
6.4. Conclusion	134
6.5. References	135
Addendum A	137

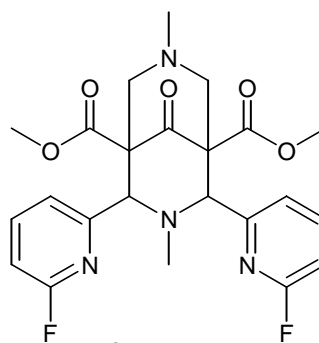
Ligand Index



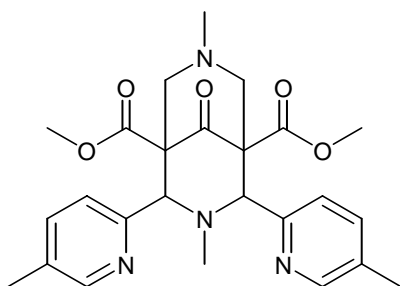
L¹ - N2py2



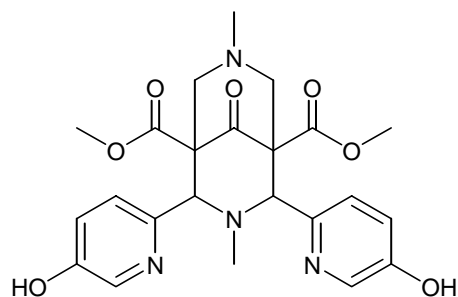
L² - N2py6Me2



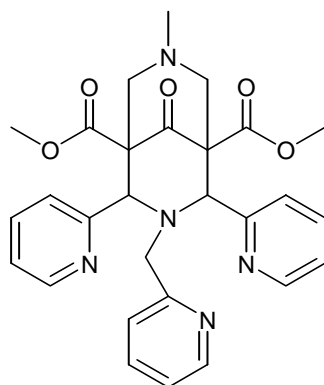
L³ - N2py6F2



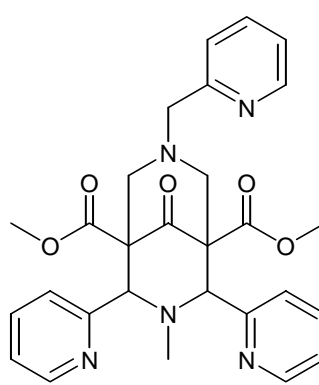
L⁴ - N2py5Me2



L⁵ - N2py5OH2



L⁶ - N2py3u



L⁷ - N2py3o

1. Introduction

Important concepts in coordination chemistry

All molecular properties are the result of the corresponding structures^[1]. In transition metal complexes the structure is determined by the oxidation and spin state of the metal centre, the electronic properties of the donor atoms and their geometric arrangement around the metal ion. The geometric arrangement of the donors is, in turn, determined by the ligand structure and denticity and the rigidity of the ligand backbone. In general therefore, the structure of a coordination compound is the result of a compromise between the preferences of the metal ion and ligand enforced geometries.

The coordination of a ligand to a metal ion induces strain on the ligand by the metal centre and strain on the metal centre by the ligand^[2]. The loss of steric energy in the ligand is compensated by the bonding energy that results from the metal ion–donor atom bond formation. In a fully preorganised ligand the structure of the metal-free ligand is identical to that of the coordinated ligand (has the same lowest energy conformation), so that there is no loss of steric strain upon bonding^[3]. It follows that preorganisation refers^[3] to a specific metal ion/ligand pair^[4] and involves the size and shape of the bonding cavity of the ligand and the preferences of the metal ion.

Related to the concept of preorganisation, is that of complementarity, which refers to the fit of a specific ligand conformation (not the minimum energy conformation) to a given metal-ion. Complexation of a ligand which is complementary, but not preorganised, therefore involves a conformational rearrangement of the ligand, which costs energy, but leads to the formation of a complex of lower energy than that which would be formed without the conformational rearrangement, due to the lack of steric strain upon the ligand in its binding conformation.

A high degree of preorganisation of a ligand for a specific metal ion maximises the stability of the resulting metal complex. However, maximum stability does not necessarily imply maximum discrimination. Metal-ion selectivity requires that the stability of a specific metal ion complex is maximised, while at the same time the stability of all other metal-ion complexes is minimised. The design of a metal-ion selective ligand must therefore involve a

1. Introduction

high degree of preorganisation for a specific metal-ion, as well as a high degree of mismatch for all other metal-ions. This requires not only a high degree of preorganisation, but also a lack of conformational flexibility and elasticity of the coordination sphere in the metal-coordinating conformation. Elasticity refers to the ease with which a specific ligand conformation can be distorted to accommodate a metal-ion and is not to be confused with ligand flexibility, which is related to the height of the energy barriers between different ligand conformations.

The main conformational flexibility of a ligand is due to rotations around single bonds. Ligand rigidity is therefore generally induced by the addition of multiple bonds, rings systems (particularly multiple fused ring systems) and sterically demanding substituents, all of which reduce the number of possible rotations around single bonds and thereby restrict the conformational freedom of the ligand. While rigid, metal-ion selective ligands can lead to exceptionally stable complexes, misfit between an inflexible ligand and a metal ion can lead to highly strained coordination geometries, which may be important in catalysis^[5].

Properties of the 3,7-diazabicyclo[3.3.1]nonane derivatives

The 3,7-Diazabicyclo[3.3.1]nonane (bispidine) backbone is derived from the natural product *Sparteine*, of which a number of 1:1 transition metal complexes are known^[6]. The bispidine ligands themselves are of interest in medicinal chemistry due to their analgesic properties^[7], but it is particularly their coordination chemistry which is of interest to this work.

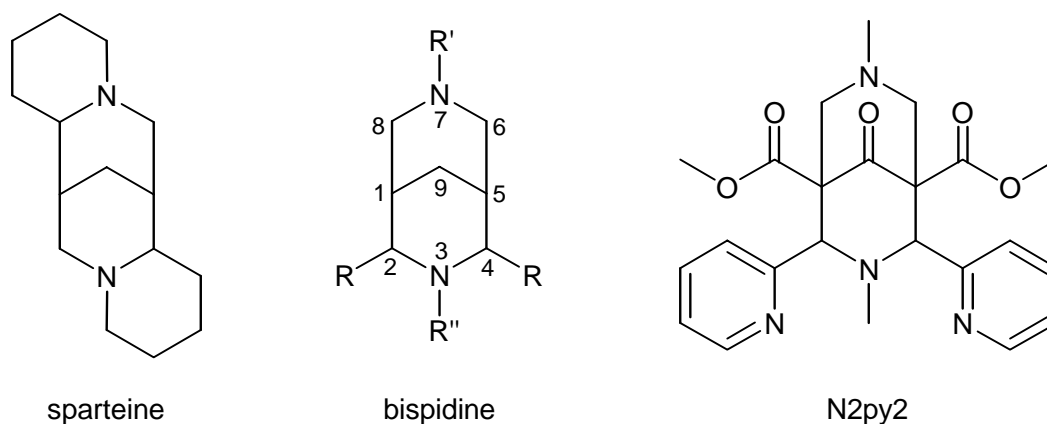


Figure 1.1. The structures of sparteine, the bispidine backbone and the C2/C4 substituted bispidine ligand N2py2 (L^1)

1. Introduction

While unsubstituted bispidines are themselves potential bidentate ligands, the ligand denticity can be increased to four by substitution at C2 and C4 (see Figure 1.1). By varying the steric and electronic properties of the substituents at C2 and C4 with pendant arms of different sizes and shapes and with different donor atoms, diverse coordination geometries can be obtained, allowing for the rational tuning of the properties of the corresponding metal complexes^[8]. In addition to the substitution at C2 and C4, further variation is possible at N3 and N7, forming as substitution products pentadentate and even hexadentate ligands^[9]. Here we focus our interest on bispidine ligands containing pyridine or substituted pyridine donors at C2/C4 and methyl or picolyl groups at N3 and N7. Tetradentate ligands formed by substitution at N3 and N7 without substitution at C2 and C4^[10], as well as bis-bispidine containing macrocyclic ligands^[11] are also known, but are not relevant to this work.

Here we focus our interest on bispidine ligands containing pyridine or substituted pyridine donors at C2/C4 and methyl or picolyl groups at N3 and N7. Tetradentate ligands formed by substitution at N3 and N7 without substitution at C2 and C4^[12], as well as bis-bispidine containing macrocyclic ligands^[13] are also known, but are not relevant to this work.

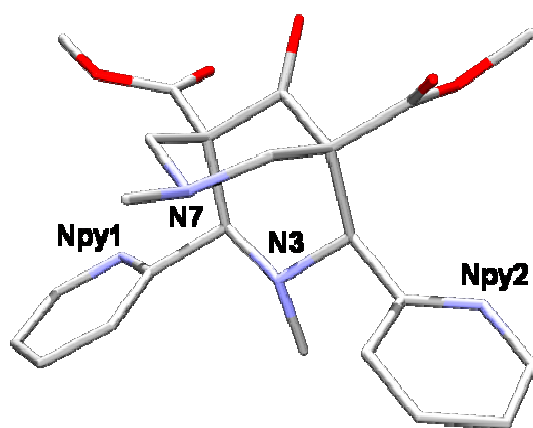


Figure 1.2. Crystal Structure of the tetradentate bispidine ligand N2py2 (L^1)^[13]

Due to two fused six-membered rings, bispidines can take on three possible conformations, namely the chair/chair, chair/boat and boat/boat. The preferred geometry is the chair/chair conformation, with the C2 and C4 substituents in an equatorial position^[14], as in the crystal structure of the tetradentate ligand N2py2^[15] (R = pyridine) shown in Figure 1.2. The two tertiary amine donors, N3 and N7, form part of the rigid ligand backbone and are highly

1. Introduction

preorganised for *cis*-coordination to small metal ions, while the two nitrogen donors of the pyridine rings are rotated away from the centre of the bispidine cavity by around 180° due to lone pair repulsions between the nitrogen donors. However, the rotation of the pyridine substituents around the C2/C4–R bond is a low energy process and in their metal coordinating conformation, bispidines are complementary for the tetradentate coordination of metal ions. In addition, the low energy torsion of the two pyridine rings allows for some variation of the metal-donor distances and provides the coordination sphere with the elasticity that leads to the observed lack of selectivity^[16].

Complexes of the bispidine ligands

Complexes of the bispidine ligands with manganese(II)^[17], iron(II)^[18], copper(I)^[13], copper(II)^[19], cobalt(II)^[20], cobalt(III)^[21], zinc(II)^[22], nickel(II)^[23] and chromium(III)^[20] have been synthesised and structurally characterised. These complexes have coordination numbers ranging from four to seven and corresponding geometries ranging from distorted tetrahedral, square-pyramidal, distorted octahedral to pentagonal-bipyramidal. The enforced coordination geometries of the bispidine complexes make them potentially interesting in the field of catalysis. The search for possible applications of the bispidine complexes has focussed mainly on the biologically relevant metals copper and iron, and these have shown activity in diverse fields, such as the catalytic azidiration of styrene^[24], olefin oxidation in the presence of H₂O₂^[25], oxygenation^[17,26] and catechol oxidase activity^[27]. Of particular interest to this work are the reactivity of the Cu(I) complexes towards molecular oxygen and the activity of the Fe(II) complexes in the catalytic oxidation of olefins with H₂O₂.

The high rigidity of the bispidine backbone is evident in the N3···N7 distances in crystal structures of the complexes, which remain fairly constant between 2.8 and 3.0 Å, regardless of the nature of the substituents, the denticity of the ligand and the nature and size of the metal ion. This is practically identical to the N3···N7 distance of 2.9 Å found in the crystal structure of the N2py2. The elasticity of the coordination sphere, on the other hand, is apparent in the Nar···Nar distances (where Nar refers to the aromatic donors substituted at C2 and C4), which vary between 3.9 and 5.0 Å and are ligand and metal-ion dependent.

1. Introduction

An important consequence, in terms of the properties of the corresponding complexes, of the rigid bispidine backbone and the substitution of aromatic donors at C2 and C4, is that the two remaining coordination sites *trans* to the tertiary amine donors N3 and N7 differ radically in their ability to bind substrates. Binding *trans* to N3 leads to the formation of short and strong metal–substrate bonds, while binding *trans* to N7 leads to longer and weaker bonds^[28].

In summary, the combination of the rigid ligand backbone and the elastic coordination sphere make the substituted bispidines a versatile class of ligands, able to complex a number of different transition metal ions. Furthermore, the geometries enforced by the bispidine backbone, lead to complexes with interesting and unusual properties, an effect which is important in the field of catalysis. Combined with the relative ease of substitution at various positions on the bispidine backbone, this allows for the rational tuning of the properties of the corresponding metal complexes. A prerequisite to this however, is a thorough understanding of the basic principles of structure and bonding in bispidine complexes. Density functional theory provides us with a useful tool for gaining a better understanding of the electronic nature of bispidine complexes (amongst others), and the information gained from such computational studies can, in turn, be applied to the rational tuning of the properties (and therefore also the catalytic activity) of these compounds.

1.1. References

-
- ¹ P. Comba, “Enforced coordination geometries - Preorganization, catalysis and beyond”, in *Chemistry at the Beginning of the Third Millennium*, L. Fabbrizzi, , Ed, Springer, Heidelberg, **2000**, 49
- ² P. Comba, *Coord. Chem. Rev.*, **1999**, 182, 343
- ³ P. Comba, *Coord. Chem. Rev.*, **1999**, 185, 81
- ⁴ R.D. Hancock, A.E. Martell, *Chem. Rev.*, **1989**, 89, 1875
- ⁵ P. Comba and W. Schiek, *Coord. Chem. Rev.*, **2003**, 238, 21
- ⁶ S.F. Mason, R.D. Peacock, *J. Chem. Soc., Dalton Trans.*, **1973**, 2, 226; E. Boschmann, G.A. Nypaver, J.P. Majors, S.M. Ealy, M. van Horn, *J. Coord. Chem.*, **1978**, 7, 141; C. Lorber, R. Choukroun, J-P. Costes, B. Donnadieu, *C.R. Chimie*, **2002**, 5, 251; B. Jasiewicz, E. Sikorska, I.V. Khmelinskii, B. Warzajtis, U. Rychlewska, W.I. Boczon, M. Sikorski, *J. Mol. Struct.*, **2004**, 707, 89
- ⁷ U. Holzgrabe, A. Cambareri, U. Kuhl, T. Siener, W. Brandt, W. Strassburger, E. Friderichs, W. Englberger, B. Kögel, M. Haurand, *Il Farmaco*, **2002**, 57, 531; U. Kuhl, W. Englberger, M. Haurand and U. Holzgrabe, *Arch. Pharm. Pharm. Med. Chem.*, **2000**, 333, 226
- ⁸ P. Comba, C. Lopez de Laorden and H. Pritzkow, *Helv. Chim. Acta*, **2005**, 88, 647
- ⁹ C. Bleiholder, H. Börzel, P. Comba, R. Ferrari, A. Heydt, M. Kerscher, S. Kuwata, G. Laurency, G.A. Lawrance, A. Lienke, B. Martin, M. Merz, B. Nuber, H. Pritzkow, *Inorg. Chem.*, **2005**, 44, 8145
- ¹⁰ G.D. Hosken, R.D. Hancock, *J. Chem. Soc. Chem. Commun.*, **1994**, 1363; G.D. Hosken, C.C. Allan, J.C.A. Boeyens, R.D. Hancock, *J. Chem. Soc., Dalton Trans.*, **1995**, 3705
- ¹¹ P. Comba, H. Pritzkow, W. Schiek, *Angew. Chem. Int. Ed.*, **2001**, 40, 13
- ¹² G.D. Hosken, R.D. Hancock, *J. Chem. Soc. Chem. Commun.*, **1994**, 1363; G.D. Hosken, C.C. Allan, J.C.A. Boeyens, R.D. Hancock, *J. Chem. Soc., Dalton Trans.*, **1995**, 3705
- ¹³ P. Comba, H. Pritzkow, W. Schiek, *Angew. Chem. Int. Ed.*, **2001**, 40, 13
- ¹⁴ P. Comba, B. Nuber and A. Ramlow, *J. Chem. Soc., Dalton Trans.*, **1997**, 347
- ¹⁵ H. Börzel, P. Comba, K.S. Hagen, C. Katsichtis and H. Pritzkow, *Chem. Eur. J.*, **2000**, 6, 914
- ¹⁶ P. Comba, M. Kerscher, M. Merz, V. Müller, H. Pritzkow, R. Remenyi, W. Schiek, Y. Xiong, *Chem. Eur. J.*, **2002**, 8, 5750
- ¹⁷ P. Comba, B. Kanellakopulos, C. Katsichtis, A. Lienke, H. Pritzkow and F. Rominger, *J. Chem. Soc., Dalton Trans.*, **1998**, 3997

- ¹⁸ H. Börzel, P. Comba, K.S. Hagen, Y.D. Lampeka, A. Lienke, M. Merz, H. Pritzkow, L.V. Tsymbal, *Inorg. Chim. Acta*, **2002**, 337, 407
- ¹⁹ H. Börzel, P. Comba, K.S. Hagen, M. Kerscher, H. Pritzkow, M. Schatz, S. Schindler, O. Walter, *Inorg. Chem.*, **2002**, 41, 5440; P. Comba, A. Hauser, M. Kerscher and H. Pritzkow, *Angew. Chem. Int. Ed.*, **2003**, 42, 4536
- ²⁰ P. Comba, B. Nuber and A. Ramlow, *J. Chem. Soc., Dalton Trans.*, **1997**, 347
- ²¹ P. Comba, S. Kuwata, M. Tarnai, H. Wadepl, *Chem. Commun.*, **2006**, *accepted*
- ²² P. Comba, M. Kerscher, M. Merz, V. Müller, H. Pritzkow, R. Remenyi, W. Schiek, Y. Xiong, *Chem. Eur. J.*, **2002**, 8, 5750
- ²³ C. Bleiholder, H. Börzel, P. Comba, R. Ferrari, A. Heydt, M. Kerscher, S. Kuwata, G. Laurenczy, G.A. Lawrance, A. Lienke, B. Martin, M. Merz, B. Nuber, H. Pritzkow, *Inorg. Chem.*, **2005**, 44, 8145
- ²⁴ P. Comba, M. Merz and H. Pritzkow, *Eur. J. Inorg. Chem.*, **2003**, 1711
- ²⁵ M.R. Bukowski, P. Comba, C. Limberg, M. Merz, L. Que, Jr., T. Wistuba, *Angew. Chem. Int. Ed.* **2004**, 43, 1283; M.R. Bukowski, P. Comba, A. Lienke, C. Limberg, C. Lopez de Lorden, R. Mas-Balleste, M. Merz, L. Que, Jr., *Angew. Chem.*, **2006**, *accepted*
- ²⁶ H. Börzel, P. Comba, C. Katsichtis, W. Kiefer, A. Lienke, V. Nagel, H. Pritzkow, *Chem. Eur. J.*, **1999**, 5, 1716
- ²⁷ H. Börzel, P. Comba and H. Pritzkow, *Chem. Commun.*, **2001**, 97; K. Born, P. Comba, A. Daubinet, *in preparation*
- ²⁸ H. Börzel, P. Comba, K.S. Hagen, Y.D. Lampeka, A. Lienke, M. Merz, H. Pritzkow, L.V. Tsymbal, *Inorg. Chim. Acta*, **2002**, 337, 407

2. Structural Isomerism in the Copper(I) Complexes of tetradentate 3,7-Diazabicyclo[3.3.1]nonane Derivatives

2.1. Introduction

Copper is an important element in both industrial^[1,2] and biological^[3,4,5] oxidation catalysis, and copper containing enzymes perform a variety of physiological functions, including the transport of dioxygen, oxidation and oxygenation^[6,7]. The functioning of these enzymes is usually based on the reversible binding of molecular oxygen by one or more Cu(I) centres, to form a variety of structurally diverse Cu-O₂ adducts^[8]. Possible 1:1 and 2:1 Cu-O₂ adducts formed upon the reaction of Cu(I) with molecular oxygen are shown in Figure 2.1.

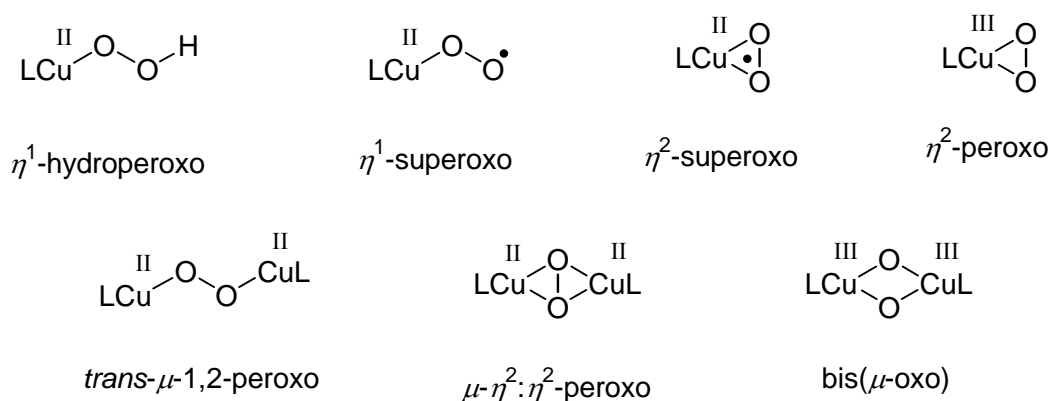


Figure 2.1. 1:1 and 2:1 Cu-O₂ species formed by reaction of Cu(I) complexes with O₂^[7]

Although side-on dicopper(II) $\mu\text{-}\eta^2\text{:}\eta^2\text{-peroxo}$ and dicopper(III) bis($\mu\text{-oxo}$) species may be more relevant in terms of natural systems, the end-on $\mu\text{-peroxo}$ ($\textit{trans-}\mu\text{-1,2-peroxo}$) bridged compounds are assumed to be important in oxygen transport and oxygen activation systems. The intrinsic thermal instability of these and other Cu-O₂ adducts, makes the choice of ligand extremely important in determining their stabilities. Oxygenation of copper(I) complexes with rigid tetradentate bispidine-type ligands (3,7-diazabicyclo[3.3.1]nonane derivatives) leads to unusually stable end-on $\mu\text{-peroxo}$ di-copper(II) compounds^[9,10,11].

2. The Copper(I) Complexes of tetradentate 3,7-Diazabicyclo[3.3.1]nonane Derivatives

While most approaches to obtain stable peroxo complexes have focused on the stabilisation of the oxidised product, the reaction can also be driven in the direction of the peroxo product by destabilising the copper(I) precursor. Two isomers of a copper(I) complex of the rigid tetradentate bispidine-type ligand L^1 have been reported and it has been postulated that the unusual stability of the corresponding copper(II)-peroxo complex, is due in part to the destabilisation of the copper(I) precursor.

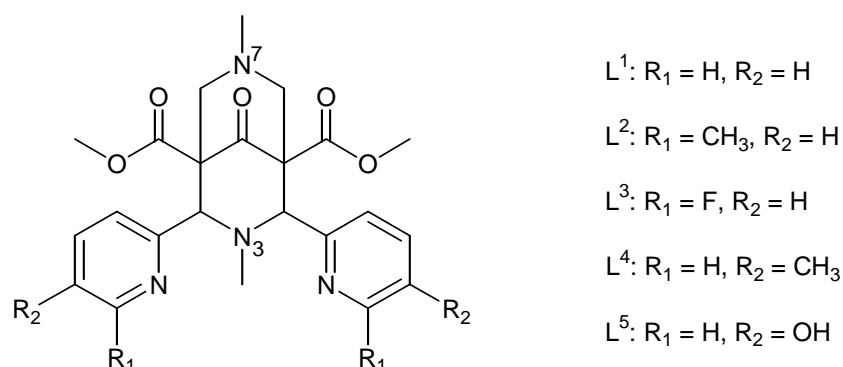


Figure 2.2. The bispidine ligand backbone and the ligands investigated

The ligands in question have rigid bispidine-type structures with two tertiary amine and two pyridine donors (Figure 2.2) and tend to enforce square-pyramidal or distorted *cis*-octahedral coordination geometries when one or two additional ligands are coordinated to the metal centre. In their metal coordinating configuration, the distance between the tertiary amine donor N7 and the plane defined by N3 and the two pyridine donors, is larger than the corresponding distance between N3 and the plane created by N7 with the two pyridine donors, making them highly complementary for the Jahn-Teller active copper(II) ion. Moreover, the coordination cavity is too inflexible to comfortably accommodate copper(I) in either a tetrahedral 4-coordinate geometry or a square pyramidal 5-coordinate geometry. The combination of these effects leads to the destabilisation of the copper(I) complexes with respect to their copper(II) counterparts, as can be seen from the low Cu(II)/Cu(I) redox potential of $[Cu(L^1)(CH_3CN)]^+$ ($E^\circ = -413$ mV vs. Ag/AgNO₃), and leads to an interesting form of structural isomerism.

2. The Copper(I) Complexes of tetradentate 3,7-Diazabicyclo[3.3.1]nonane Derivatives

Complexes with L^1 and L^2 have been experimentally characterised and the crystal structures are shown in Figure 2.3. The reaction of $[\text{Cu}(\text{CH}_3\text{CN})_4](\text{O}_3\text{SCF}_3)$ with L^1 yields a pale yellow product, while reaction with $[\text{Cu}(\text{CH}_3\text{CN})_4](\text{BF}_4)$ leads to a dark red compound. The crystal structures and elemental analyses indicate that these two products are isomers, the yellow product being the 4-coordinate form of $[\text{Cu}(L^1)(\text{CH}_3\text{CN})]^+$, in which one of the pyridine rings of the bispidine ligand remains uncoordinated (Figure 2.3(b)), and the red compound the 5-coordinate form (Figure 2.3(a)). Fluxionality is observed in the NMR spectra of these compounds, indicating that they are close in energy and that a fast dynamic equilibrium exists between them in solution. $[\text{Cu}(L^2)(\text{CH}_3\text{CN})]^+$, on the other hand, is found in the solid state only in the 4-coordinate form (Figure 2.3(c)), but NMR studies indicate the presence of a symmetric species in solution, which is characterised as the 4-coordinate $[\text{Cu}(L^2)]^+$ complex however (in which acetonitrile does not coordinate to the metal centre), rather than the 5-coordinate form of $[\text{Cu}(L^2)(\text{CH}_3\text{CN})]^+$ ^[12]. Exposure of $[\text{Cu}(L^1)(\text{CH}_3\text{CN})]^+$ to O_2 leads to the formation of a relatively stable $[\text{L}^1\text{Cu}^{\text{II}}\text{O}_2\text{Cu}^{\text{II}}\text{L}^1]^{2+}$ species, while the oxidation of $[\text{Cu}(L^2)(\text{CH}_3\text{CN})]^+$ leads to the slow formation of the corresponding Cu(II) complex, $[\text{Cu}(L^2)(\text{CH}_3\text{CN})]^{2+}$ and no stable peroxo complex.

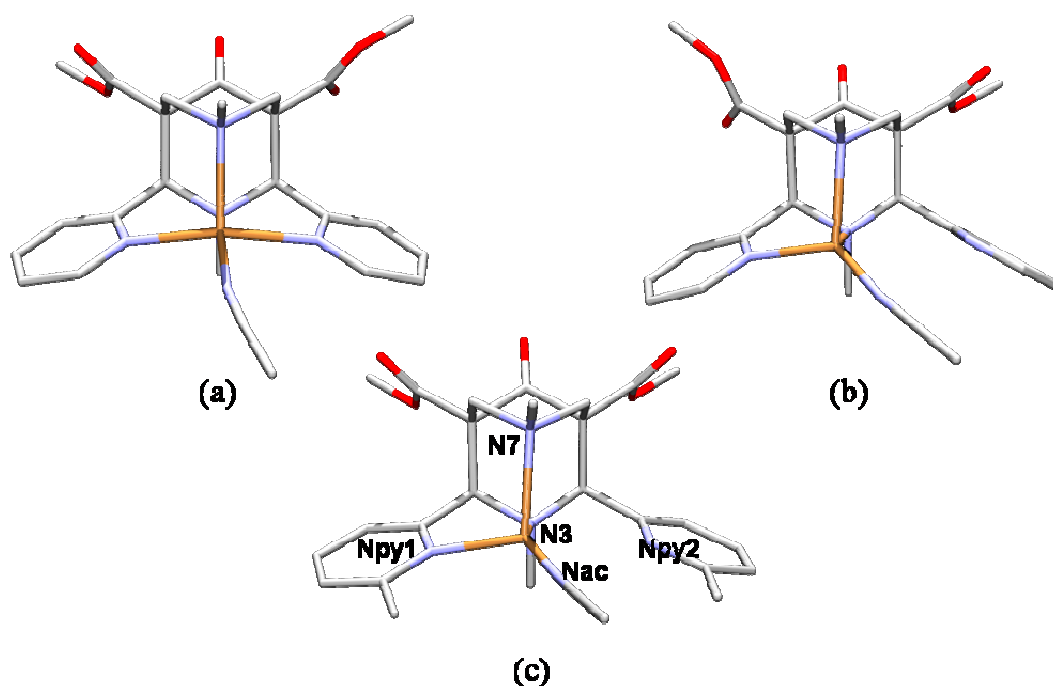


Figure 2.3. Crystal structures of (a) 5-coordinate $[\text{Cu}(L^1)(\text{CH}_3\text{CN})]^+$, (b) 4-coordinate $[\text{Cu}(L^1)(\text{CH}_3\text{CN})]^+$ and (c) 4-coordinate $[\text{Cu}(L^2)(\text{CH}_3\text{CN})]^+$

2. The Copper(I) Complexes of tetradentate 3,7-Diazabicyclo[3.3.1]nonane Derivatives

Here we report density functional theory (DFT) calculations on the copper(I)-acetonitrile complexes of a set of tetradentate bispidine ligands (L^1 – L^5 in Figure 2.2), in which the substituent, as well as the position of substitution, on the two pyridine rings has been varied in an attempt to better understand the factors governing this constitutional isomerism. We show that the relative energy of the two isomers is dependent on the size of the group R_1 , irrespective of its electronic effect, while the group R_2 is too far away from the coordination site to have a steric effect and can be used to tune the Cu(I)/Cu(II) redox potentials and thereby the reactivity towards molecular oxygen, by means of its electronic effects. While we concentrate here on the field of oxidation catalysis, the results may be transferred to the catalytic azidination of olefins, in which the relative stabilities of the Cu(I) and Cu(II) oxidation state also play a deciding role^[13].

2.2. Computational Methods

DFT calculations were performed with Gaussian03^[14] using Becke's 3-parameter hybrid exchange functional, in conjunction with the correlation functional of Lee, Yang and Parr (B3LYP)^[15]. This combination has been demonstrated to provide accurate geometries for a wide range of systems^[16] and to perform well in the particular case of transition metals^[17]. For the geometry optimisations the 6-311G+(d) basis set was used for heavy atoms and the 6-31G basis set for hydrogen atoms. Note that the 6-311G basis set, as defined in Gaussian03, in fact corresponds to a combination of basis sets, namely the Wachters-Hay all electron basis set^[18] for the first transition row using the scaling factor of Raghavachari and Trucks (diffuse functions added according to the recommendation of Raghavachari and Trucks)^[19], the McLean-Chandler (12s, 9p) \rightarrow (621111, 52111) basis set^[20] for second-row atoms and the 6-311G basis set^[21] for first-row atoms. Wave function stability tests were performed on selected optimised structures. Frequency calculations were performed on all optimised structures to verify that they are minima on the potential energy surface and zero-point energy corrections were added to the energies obtained from the geometry optimisations to obtain the final energies. Single point (SP) energies were calculated at the same level of theory as for the geometry optimisations, but including solvent effects via the Polarised Continuum Model (PCM)^[22] with acetonitrile as a solvent.

A simplified model system was used in all calculations, in which the ester groups at C1 and C5 on the ligand backbone (see Figure 1.1) were replaced by hydrogen atoms. Although the simplified ligand and some of the complexes have C_s symmetry, symmetry restraints were not used in the final optimisations.

2.3. Results and Discussion

Table 2.1 summarises the calculated and experimental (where available) geometric parameters for the $[\text{Cu}(\text{L})(\text{CH}_3\text{CN})]^+$ compounds of ligands L^1 to L^5 , as well as the relative energies of the 4- and 5-coordinate forms. For ligand L^1 both the 4- and 5-coordinate structures are minima on the potential energy surface, with the 5-coordinate structure being the global minimum. For ligands L^2 and L^3 , the 5-coordinate forms are destabilised to the extent that they become saddle points on the potential energy surface and are in fact transition states between the two 4-coordinate isomers.

The energy of the 5-coordinate structure is dependent on the size of the R_1 substituent in the *ortho* position on the pyridine rings. For L^2 ($\text{R}_1 = \text{CH}_3$) the energy barrier is 2.70 kJ/mol, for L^3 ($\text{R}_1 = \text{F}$) the energy barrier is lowered to 0.68 kJ/mol and for L^1 ($\text{R}_1 = \text{H}$), the 5-coordinate form is the global minimum, with an energy 1.75 kJ/mol lower than that of the 4-coordinate form. This on its own is interesting, given the preference that the spherically symmetrical d^{10} copper(I) ion demonstrates for tetrahedral geometries, and can be attributed to the preference of the bispidine backbone for square-pyramidal geometries and the destabilisation of the tetrahedral form due to the steric strain caused by the uncoordinated pyridine in the 4-coordinate form. For L^2 and L^3 , the steric strain of the substituent and the preference of the copper(I) centre for tetrahedral geometries overrides the preferences of the ligand and the steric strain of the uncoordinated pyridine, to give 4-coordinate, distorted tetrahedral geometries. The addition of solvent effects makes little difference to the calculated relative energies.

A comparison of the calculated geometries and the available experimental structures (4- and 5-coordinate $[\text{Cu}(\text{L}^1)(\text{CH}_3\text{CN})]^+$, 4-coordinate $[\text{Cu}(\text{L}^2)(\text{CH}_3\text{CN})]^+$) shows a good overall correspondence. While the bond distances are slightly overestimated for all the calculated structures, the qualitative trends are well reproduced. The average error in bond length is below 0.1 Å for all 3 structures and the largest error of 0.16 Å is found for the Cu–Npy1 bond (the bound pyridine) in the 4-coordinate isomer of $[\text{Cu}(\text{L}^1)(\text{CH}_3\text{CN})]^+$.

Table 2.1. Selected calculated and experimental geometric parameters for the [Cu(L)(CH₃CN)]⁺ complexes, for L¹-L⁵. Experimental values are given in bold and italics, * indicates that the structure is a transition state and not a minimum

Ligand	L ¹	L ¹	L ¹	L ¹	L ²	L ²	L ²	L ²	L ³	L ³	L ³	L ⁴	L ⁴	L ⁴	L ⁵	L ⁵
Parameters	5-coord	5-coord	4-coord	4-coord	5-coord*	4-coord	4-coord	5-coord*	4-coord	5-coord*	4-coord	5-coord	4-coord	5-coord	4-coord	5-coord
Bond distances (Å)																
Cu-N7	2.288	2.186	2.234	2.160	2.203	2.224	2.184	2.200	2.212	2.294	2.212	2.237	2.237	2.273	2.237	2.273
Cu-N3	2.418	2.292	2.228	2.203	2.166	2.223	2.203	2.217	2.258	2.417	2.258	2.255	2.255	2.397	2.255	2.397
Cu-Npy1	2.249	2.169	2.225	2.066	2.632	2.186	2.096	2.542	2.200	2.254	2.200	2.208	2.208	2.277	2.208	2.277
Cu-Npy2	2.249	2.247	2.745	3.118	2.632	3.188	2.897	2.542	2.993	2.254	2.254	2.790	2.790	2.278	2.790	2.278
Cu-Nac	1.993	1.936	1.935	1.873	1.918	1.920	1.900	1.921	1.918	1.991	1.918	1.933	1.933	1.982	1.933	1.982
Npy1...Npy2	4.225	4.212	4.709	4.945	5.093	4.750	4.912	4.236	4.737	4.288	4.236	4.225	4.225	4.212	4.225	4.212
N7...N3	3.103	2.973	3.023	2.914	3.001	2.925	3.010	3.102	3.021	3.092	3.021	3.103	3.103	2.973	3.103	2.973
Valence angles (°)																
N7-Cu-N3	82.46	83.15	84.58	83.77	86.56	84.91	83.63	85.82	84.65	82.299	84.65	84.519	84.519	82.88	84.519	82.88
Npy1-Cu-Npy2	139.85	145.07	142.45	144.30	144.21	142.07	143.60	143.57	141.67	140.02	141.67	142.52	142.52	140.59	142.52	140.59
N3-Cu-Nac	160.71	154.95	146.85	134.16	147.05	139.64	150.09	144.98	138.39	160.40	144.98	146.19	146.19	156.68	146.19	156.68
N7-Cu-Nac	116.84	121.46	123.32	118.49	126.38	120.93	110.76	129.21	124.56	117.30	124.56	122.90	122.90	120.44	122.90	120.44
Npy1-Cu-Nac	103.65	104.73	111.99	128.38	101.18	120.40	120.95	100.47	119.67	103.60	119.67	113.13	113.13	102.57	113.13	102.57
Npy2-Cu-Nac	103.64	97.43	91.10	76.28	101.18	84.99	86.61	100.47	83.61	103.54	83.61	90.05	90.05	102.53	90.05	102.53
Torsions angles (°)																
N3-C-C-Npy1	37.26	38.39	39.69	41.53	46.58	41.18	35.69	45.25	41.58	37.41	41.58	39.64	39.64	38.71	39.64	38.71
N3-C-C-Npy2	-37.26	-39.94	-44.54	-61.15	46.58	-55.60	-45.44	45.25	-51.01	-37.41	-51.01	-45.02	-45.02	-38.71	-45.02	-38.71
Relative Energies (kJ/mol)																
Gas phase	0.00	-	1.74	-	2.70	0.00	-	0.68	0.00	0.40	0.00	1.59	1.59	0.00	1.59	0.00
Solvent	0.00	-	1.98	-	3.08	0.00	-	2.81	0.00	6.60	0.00	7.58	7.58	0.00	7.58	0.00

This is an indication of a more general discrepancy, namely that the distortion of the calculated structure from an ideal tetrahedral geometry is much larger than that of the experimental structure, and can be seen also in the large (18°) difference between the $N3-C-C-N_{py2}$ torsion angles in the calculated and the experimental structures. In the experimental structure the unbound pyridine ring is rotated out of the plane created by $N3$, the copper ion and the bound pyridine (the torsion angle is 20° larger than the torsion angle of the bound pyridine, see Figure 2.3(b)), while in the calculated structure the difference between the bound and unbound torsion angles is only 5° . This leaves less space to accommodate the acetonitrile below the unbound pyridine in the calculated structure and leads to a distortion from ideal tetrahedral geometry. Interestingly, the unbound pyridine ring in the crystal structure of L^2 is not twisted out of plane (see Figure 2.3(c)), but has an $N3-C-C-N_{py2}$ torsion angle similar to that of the calculated 4-coordinate structure of L^1 . The calculated geometry of L^2 , on the other hand, shows the twisted away pyridine ring observed in the 4-coordinate crystal structure of L^1 , although not to the same extent. This is demonstrated in Figure 2.4, in overlay plots of the calculated and experimental structures of the 4-coordinate isomers of $[Cu(L^1)(CH_3CN)]^+$ and $[Cu(L^2)(CH_3CN)]^+$.

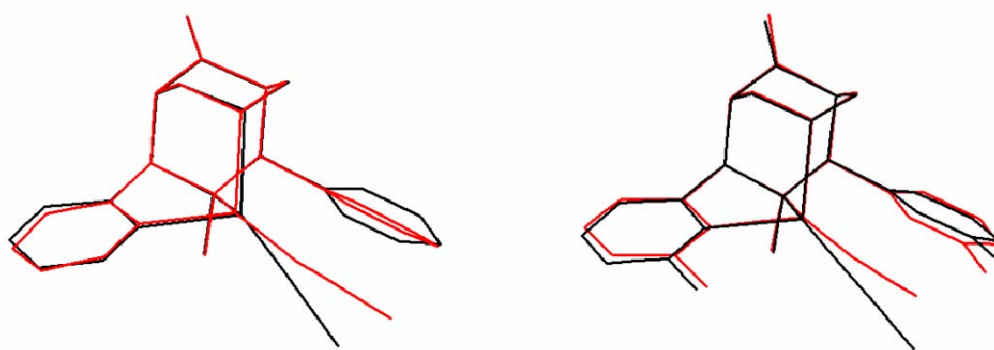


Figure 2.4. Overlay of the calculated and experimental structures of the 4-coordinate isomers of $[Cu(L^1)(CH_3CN)]^+$ and $[Cu(L^2)(CH_3CN)]^+$

To further investigate this discrepancy, rigid potential energy surface (PES) scans were performed for the 4-coordinate complexes of L^1 and L^2 , varying the torsion angle of the unbound pyridine in steps of 5° . It was found that the increase in total energy upon rotation of

the pyridine by 10° out of plane in either direction is only 1kJ/mol. Given these small energy losses on rotation of the pyridine ring, the shallowness of the PES in the region of the metal centre and the small energy barriers between minima, it seems likely that the twisting of the pyridine ring in the 4-coordinate L^1 structure is merely a crystal packing effect and that the calculated minimum is the actual minimum in the gas phase and in solution. This would also agree with the observation that there is a fast dynamic equilibrium between the 4- and 5-coordinate isomers of L^1 in solution, which would be facilitated by the unbound pyridine ring remaining in plane with the metal centre and the bound pyridine.

Two important facts emerge, namely that the PES of the metal coordination sphere is exceptionally shallow, with two or more minima separated by transition states with energy barriers of less than 5 kJ/mol; and that the relative energy of the minima and the transition states can be controlled by choice of substituent in the *ortho* position on the pyridine rings. Furthermore, it seems as if the electronic effect of the R^1 substituent plays a negligible role in the stabilisation/destabilisation of these minima and saddle points, compared to the much larger steric effect so close to the coordination centre.

To test this supposition two further ligands, L^4 and L^5 (see Figure 2.2), substituted in the *meta* position rather than in the *ortho*, were introduced, and the relative energy of the two geometric forms were calculated. Ligand L^4 , with $R_1 = H$ and $R_2 = CH_3$, is an isomer of L^2 ($R_1 = CH_3$ and $R_2 = H$), allowing for a direct comparison of steric effects on the potential energy surface, and ligand L^5 has $R_1 = H$ and $R_2 = OH$. Thus we have a comparison of two ligands with similar electronic effects but different steric effects (L^2 and L^4), as well as two ligands with similar (and minimal) steric effects, but different electronic effects (L^4 and L^5). For L^4 we indeed find the 5-coordinate form to be the global minimum, as for L^1 . The difference in energy between this and the 4-coordinate form is also in the same region as for L^1 (1.19 kJ/mol). Relative to the global minimum of L^2 , both isomers are destabilised (see Table 2.1), indicating that *ortho* substitution is slightly favoured over *meta* substitution, despite the steric effects. For L^5 , only a 5-coordinate isomer could be located and attempts to optimize a 4-coordinate geometry by initially restraining the N3-C-C-Npy torsion angles to the values found for L^1 , resulted in convergence to a 5-coordinate structure as soon as the

restraints were removed. The similar energetics of L^1 and L^4 (and the dissimilar energetics of L^2 and L^4) confirms that a 4-coordinate minimum can only be induced by destabilisation of the 5-coordinate minimum and only by *ortho* substitution on the pyridine rings.

Since the presence of a symmetrical $[\text{Cu}(L^2)]^+$ complex (tetradentate copper(II) bispidine complex without a coordinated solvent molecule) could be deduced from NMR studies in solution (acetonitrile)^[12], it was of interest to determine the energy of this species relative to that of the corresponding $[\text{Cu}(L^2)(\text{CH}_3\text{CN})]^+$ complex. In addition to the optimisations of the $[\text{Cu}(L)(\text{CH}_3\text{CN})]^+$ complexes therefore, optimised structures of the $[\text{Cu}(L)]^+$ complexes of L^1 , L^2 , L^4 and L^5 were obtained and their energies relative to the corresponding $[\text{Cu}(L)(\text{CH}_3\text{CN})]^+$ complexes were determined, both in the gas phase and in solution. The optimised geometries of $[\text{Cu}(L)]^+$ and energies of the ($[\text{Cu}(L)]^+ + \text{CH}_3\text{CN}$) combination relative to the corresponding $[\text{Cu}(L)(\text{CH}_3\text{CN})]^+$ complex are given in Table 2.2. For $[\text{Cu}(L^3)]^+$ no minimum could be located.

Table 2.2. Selected geometric parameters and relative energies of the $[\text{Cu}(L)]^+$ complexes, for L^1 , L^2 , L^4 and L^5

Ligand	L^1	L^2	L^4	L^5
Bond lengths (Å)				
Cu-N7	2.339	2.350	2.341	2.319
Cu-N3	2.279	2.266	2.276	2.275
Cu-Npy*	2.010	2.019	2.011	2.016
Npy...Npy	3.920	3.942	3.923	3.928
N7...N3	3.166	3.167	3.166	3.166
Bond angles (°)				
N7-Cu-N3	86.56	86.59	86.58	87.14
Npy-Cu-Npy	154.31	154.88	154.51	153.86
Bond torsions (°)				
N3-C-C-Npy*	37.45	37.29	37.47	38.15
Relative Energies (kJ/mol)				
Gas phase	50.26	35.40	46.95	52.43
Solvent	14.34	5.05	18.72	13.70

*The complexes have C_s symmetry, so the parameters for Npy1 and Npy2 are identical

2. The Copper(I) Complexes of tetradentate 3,7-Diazabicyclo[3.3.1]nonane Derivatives

The geometries of all the $[\text{Cu}(\text{L})]^+$ fragments are relatively similar and, as expected, they are much higher in energy than the $[\text{Cu}(\text{L})(\text{CH}_3\text{CN})]^+$ complexes in the gas phase. In solution however, the relative stabilities of the $[\text{Cu}(\text{L})]^+$ complexes changes dramatically. Particularly interesting is that the destabilisation of the $[\text{Cu}(\text{L}^2)]^+$ complex relative to the corresponding acetonitrile complex is only 5.05 kJ/mol, whereas for $[\text{Cu}(\text{L}^1)]^+$ this energy difference is 14.36 kJ/mol. This is in agreement with the experimental observation that both $[\text{Cu}(\text{L}^2)(\text{CH}_3\text{CN})]^+$ and $[\text{Cu}(\text{L}^2)]^+$ are observed in the NMR in solution, whereas for L^1 only the $[\text{Cu}(\text{L}^1)(\text{CH}_3\text{CN})]^+$ complex is observed. The relative energies of $[\text{Cu}(\text{L}^4)]^+$ and $[\text{Cu}(\text{L}^5)]^+$ both in the gas phase and in solution, are close to those of $[\text{Cu}(\text{L}^1)]^+$ and significantly different from $[\text{Cu}(\text{L}^2)]^+$.

The copper(I) complexes of *ortho* substituted ligands therefore have two possible geometric forms, 4-coordinate $[\text{Cu}(\text{L})(\text{CH}_3\text{CN})]^+$ and 4-coordinate $[\text{Cu}(\text{L})]^+$, whereas the complexes of unsubstituted and *meta* substituted ligands demonstrate 4- and 5-coordinate isomerism of $[\text{Cu}(\text{L})(\text{CH}_3\text{CN})]^+$. The two possible geometries of the copper(I) complexes of the isomers L^2 and L^4 are shown in Figure 2.5, along with the relative energies.

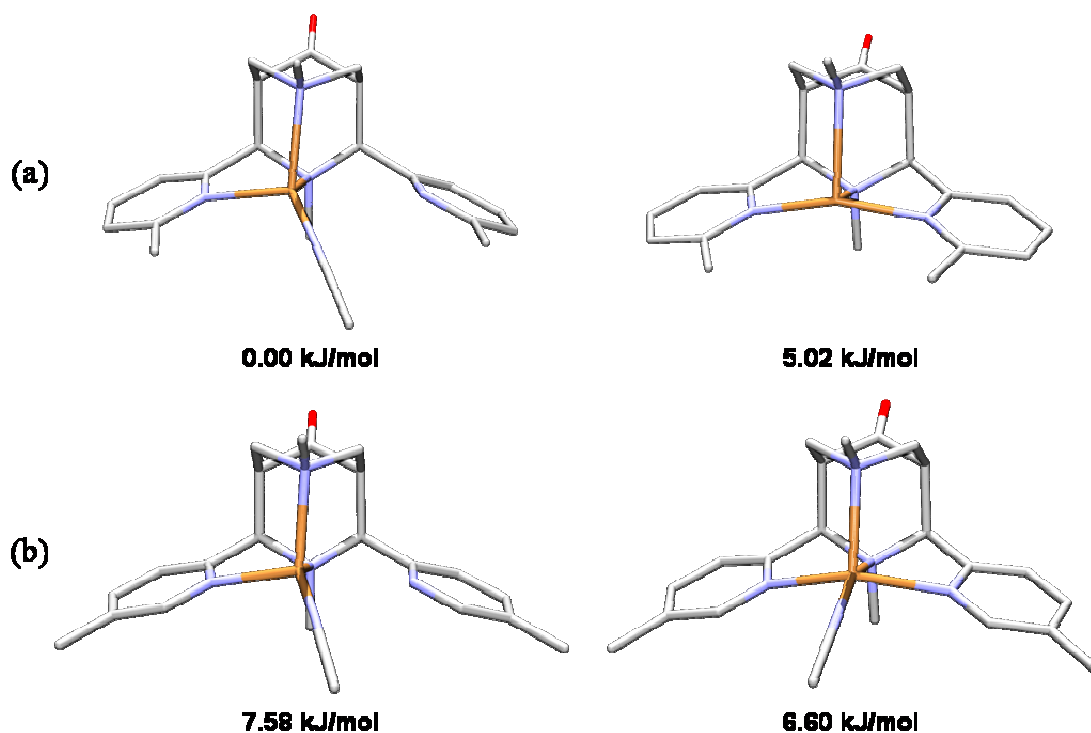


Figure 2.5. The two geometric forms of the copper(I)-complexes of (a) L^2 and (b) L^4 , including the relative energies

2.4. Conclusion

The calculations indicate that any *ortho* substituent on the pyridine rings will destabilise the 5-coordinate geometry of the $[\text{Cu}(\text{L})(\text{CH}_3\text{CN})]^+$ complexes and lead to a 4-coordinate ground state. However, the calculations also show that the potential energy surfaces of these complexes are extremely shallow in the region of the metal coordination centre, with relative energies between the 4-coordinate minima and the 5-coordinate minima/transition states of less than 5 kJ/mol. These minimal energy differences can therefore not affect the formation of the corresponding oxygenation product, $[\text{LCu}^{\text{II}}\text{O}_2\text{Cu}^{\text{II}}\text{L}]^{2+}$, directly. We propose however, that the same steric effects that lead to the stabilisation of a 4-coordinate geometry in the copper(I) precursor, will lead to the destabilisation of the corresponding copper(II) oxygenation product. The existence of a 5-coordinate minimum on the potential energy surfaces of the $[\text{Cu}(\text{L})(\text{CH}_3\text{CN})]^+$ complexes and/or the relative energy of this minimum to the 4-coordinate geometry, can therefore be used to predict the stability of the corresponding $[\text{LCu}^{\text{II}}\text{O}_2\text{Cu}^{\text{II}}\text{L}]^{2+}$ complex. $[\text{Cu}(\text{L})(\text{CH}_3\text{CN})]^+$ complexes with a 5-coordinate ground state will yield stable oxygenation products when exposed to oxygen (as for L^1), whereas $[\text{Cu}(\text{L})(\text{CH}_3\text{CN})]^+$ complexes with a 4-coordinate ground state will lead to slow oxidation of the reactant to the corresponding $[\text{Cu}(\text{L})(\text{CH}_3\text{CN})]^{2+}$ complex and no oxygenation products (as for L^2). Since even the smallest *ortho* substituent possible (fluorine) stabilises a 4-coordinate ground state, Cu(I) complexes of *ortho* substituted ligands will not form stable *trans*- μ -1,2-peroxo Cu(II) complexes.

This is supported by the known crystal structures of Cu(II) bispidine complexes and the supposition that one of the reasons for the exceptional stability of the bispidine *trans*- μ -1,2-peroxo Cu(II) complexes is the strong in-plane bonding of the peroxo unit *trans* to the tertiary amine donor N3. Whereas the acetonitrile ligand is coordinated *trans* to N3 in the crystal structure of $[\text{Cu}(\text{L}^2)(\text{CH}_3\text{CN})]^{2+}$, larger co-ligands coordinate *trans* to N7, as is seen in the crystal structures of $[\text{Cu}(\text{L}^2)(\text{H}_2\text{O})]^{2+}$ and $[\text{Cu}(\text{L}^2)(\text{Cl})]^+$. $[\text{Cu}(\text{L})(\text{CH}_3\text{CN})]^+$ complexes with *ortho* substituted pyridine rings therefore, will not be able to accommodate the peroxo unit in the favourable *trans* N3 position (see Chapter 3 for a discussion of the

2. The Copper(I) Complexes of tetradentate 3,7-Diazabicyclo[3.3.1]nonane Derivatives

reasons why *trans* N3 coordination is favourable), and oxidation to $[\text{Cu}(\text{L}^2)(\text{CH}_3\text{CN})]^{2+}$ (in which the acetonitrile can be accommodated *trans* to N3) will be favoured.

It is possible, however, to influence the electron density on the metal (and thereby also the redox potential and the reactivity towards O_2), by substitution in the *meta* position. Substitution of electron donating groups in the *meta* position does not lead to a destabilisation of the 5-coordinate geometry, while at the same time increasing the electron density in the pyridine rings and thereby destabilising Cu(I) with respect to Cu(II).

In addition to the 4-coordinate $[\text{Cu}(\text{L})(\text{CH}_3\text{CN})]^+$ complexes of *ortho* substituted ligands, a further structural form is observed, namely a 4-coordinate $[\text{Cu}(\text{L})]^+$ species, in which both pyridine rings of the bispidine ligand are coordinated to the metal centre and no acetonitrile is coordinated. This species is highly unstable in the gas phase, but within 10 kJ/mol of the 4-coordinate $[\text{Cu}(\text{L})(\text{CH}_3\text{CN})]^+$ complex in solution. For unsubstituted or *meta* substituted ligands this structural form is destabilised by more than 10 kJ/mol with respect to the corresponding 5-coordinate $[\text{Cu}(\text{L})(\text{CH}_3\text{CN})]^+$ complex, even in solution. These calculated energy differences are in good agreement with NMR studies of the copper(I) complexes of L^1 and L^2 in acetonitrile.

2.5. References

-
- ¹ R.A. Sheldon, J.K. Kochi, *Metal-Catalyzed Oxidations of Organic Compounds*, Academic Press, New York, **1981**
- ² K.A. Jørgensen, *Chem. Rev.*, **1989**, 89, 431
- ³ N. Kitajima, Y. Moro-oka, *Chem. Rev.*, **1994**, 94, 737
- ⁴ E.A. Lewis, W.B. Tolman, *Chem. Rev.*, **2004**, 104, 1047
- ⁵ J. Reedijk, *Bioinorganic Catalysis, 2nd Ed.*, **1999**
- ⁶ K.D. Karlin, D-H. Lee, H.V. Obias and K.J. Humphreys, *Pure & Appl. Chem.*, **1998**, 70, 855
- ⁷ E.I. Solomon, F. Tuzcek, D.E. Root and C. Brown, *Chem. Rev.*, **1994**, 827
- ⁸ L.M. Mirica, X. Ottenwaelder and T.D. Stack, *Chem. Rev.*, **2004**, 104, 1013
- ⁹ H. Börzel, P. Comba, C. Katsichtis, W. Kiefer, A. Lienke, V. Nagel and H. Pritzkow, *Chem. Eur. J.*, **1999**, 5, 1716
- ¹⁰ H. Börzel, P. Comba, K.S. Hagen, C. Katsichtis and H. Pritzkow, *Chem. Eur. J.*, **2000**, 6, 914
- ¹¹ H. Börzel, P. Comba, K.S. Hagen, M. Kerscher, H. Pritzkow, M. Schatz, S. Schindler and O. Walter, *Inorg. Chem.*, **2002**, 41, 5440
- ¹² M. Kerscher, *PhD Thesis*, Ruprecht-Karls Universität Heidelberg, **2003**
- ¹³ P. Comba, M. Merz and H. Pritzkow, *Eur. J. Inorg. Chem.*, **2003**, 1711
- ¹⁴ *Gaussian 03, Revision B.03*, M. J. Frisch, G. W. Trucks, H. B. Schlegel, G. E. Scuseria, M. A. Robb, J. R. Cheeseman, J. A. Montgomery, Jr., T. Vreven, K. N. Kudin, J. C. Burant, J. M. Millam, S. S. Iyengar, J. Tomasi, V. Barone, B. Mennucci, M. Cossi, G. Scalmani, N. Rega, G. A. Petersson, H. Nakatsuji, M. Hada, M. Ehara, K. Toyota, R. Fukuda, J. Hasegawa, M. Ishida, T. Nakajima, Y. Honda, O. Kitao, H. Nakai, M. Klene, X. Li, J. E. Knox, H. P. Hratchian, J. B. Cross, C. Adamo, J. Jaramillo, R. Gomperts, R. E. Stratmann, O. Yazyev, A. J. Austin, R. Cammi, C. Pomelli, J. W. Ochterski, P. Y. Ayala, K. Morokuma, G. A. Voth, P. Salvador, J. J. Dannenberg, V. G. Zakrzewski, S. Dapprich, A. D. Daniels, M. C. Strain, O. Farkas, D. K. Malick, A. D. Rabuck, K. Raghavachari, J. B. Foresman, J. V. Ortiz, Q. Cui, A. G. Baboul, S. Clifford, J. Cioslowski, B. B. Stefanov, G. Liu, A. Liashenko, P. Piskorz, I. Komaromi, R. L. Martin, D. J. Fox, T. Keith, M. A. Al-Laham, C. Y. Peng, A. Nanayakkara, M. Challacombe, P. M. W. Gill, B. Johnson, W. Chen, M. W. Wong, C. Gonzalez, and J. A. Pople, *Gaussian, Inc., Pittsburgh PA, 2003*

- ¹⁵ C. Lee, W. Yang, R. Parr, *Phys. Rev. B*, **1988**, 37, 785-789; A.D. Becke, *J. Chem. Phys.*, **1993**, 98, 5648
- ¹⁶ C.W. Bauschlicher, *Chem. Phys. Lett.*, **1995**, 246, 40
- ¹⁷ S. Nui, M.B. Hall, *Chem. Rev.*, **2000**, 100, 353
- ¹⁸ A.J. Wachters, *J. Chem. Phys.*, **1970**, 52, 1033; P.J. Hay, *J. Chem. Phys.*, **1977**, 66 4377
- ¹⁹ K. Raghavachari, G.W. Trucks, *J. Chem. Phys.*, **1989**, 91, 1062
- ²⁰ A.D. McLean, G.S. Chandler, *J. Chem. Phys.*, **1980**, 72 5639; R. Krishnan, J.S. Binkley, R. Seeger, J.A. Pople, *J. Chem. Phys.*, **1980**, 72, 650
- ²¹ R.C. Binning, Jr., L.A. Curtiss, *J. Comp. Chem.*, **1990**, 11 1206; L.A. Curtiss, M.P. McGrath, J-P. Blaudeau, N.E. Davis, R.C. Binning Jr., L. Radom, *J. Chem. Phys.*, **1995**, 103, 6104; M.P. McGrath, L. Radom, *J. Chem. Phys.*, **1991**, 94, 511
- ²² M.T. Cancès, B. Mennucci and J. Tomasi, *J. Chem. Phys.*, **1997**, 107, 3032; M. Cossi, V. Barone, B. Mennucci and J. Tomasi, *Chem. Phys. Lett.*, **1998**, 286, 253; B. Mennucci and J. Tomasi, *J. Chem. Phys.*, **1997**, 106, 5151; M. Cossi, G. Scalmani, N. Rega and V. Barone, *J. Chem. Phys.*, **2002**, 117, 43

3. The Copper(II) Complexes of tetradentate 3,7-Diazabicyclo[3.3.1]nonane Derivatives: Isomerism, Electronic Structure and Spin Density Distribution

3.1. Introduction

Due to the rigidity of the bispidine backbone, tetradentate 3,7-diazabicyclo[3.3.1]nonane derivatives, in their metal coordinating configuration, are highly complementary for the Jahn-Teller active copper(II) ion. The resulting complexes have square-pyramidal (monodentate co-ligands such as Cl^- , CH_3CN or H_2O , tccH^-)^[1,2,3,4] or distorted *cis*-octahedral (bidentate co-ligands such as NO_3^- , tcc^{2-})^[3,4] geometries (where tccH_2 = tetrachlorocatechol), in which the Jahn-Teller elongated axis is determined by the choice of co-ligand and/or substitution *ortho* to the nitrogen donors on the pyridine rings.

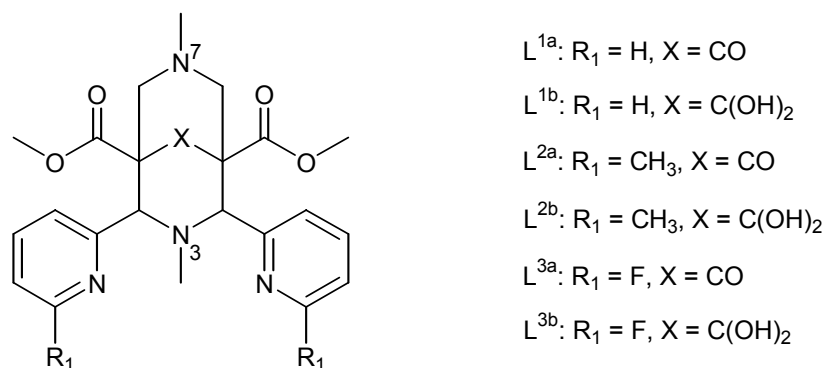


Figure 3.1. The basic ligand structure and the ligands investigated

The $[\text{Cu}(\text{L})(\text{Cl})]^+$ complexes of the ligands L^{1b} and L^{2b} (see Figure 3.1) have been synthesised and their crystal structures determined^[1,2]. L^{1b} in particular, is well suited for the coordination of copper(II) and the resulting complex, $[\text{Cu}(\text{L}^{1b})(\text{Cl})]^+$, is exceptionally stable. The experimentally observed structure, shown in Figure 3.2, is square-pyramidal, with the two pyridine donors, the tertiary amine donor N3 and Cl^- coordinated in the equatorial plane, and the Cu–N7 bond axial and Jahn-Teller elongated. In contrast to this is the experimental structure of $[\text{Cu}(\text{L}^{2b})(\text{Cl})]^+$, in which the Cl^- is coordinated *trans* to N7, leading also to a

square-pyramidal structure, but one in which the Cu–N3 bond is in the axial position and the Jahn-Teller stabilisation is quenched by the demands of the rigid ligand backbone. This quenching of the Jahn-Teller effect can be clearly seen by comparing the Cu–N7/Cu–N3 ratio in $[\text{Cu}(\text{L}^{1\text{b}})(\text{Cl})]^+$ to the Cu–N3/Cu–N7 ratio in $[\text{Cu}(\text{L}^{2\text{b}})(\text{Cl})]^+$ (see Figure 3.2).

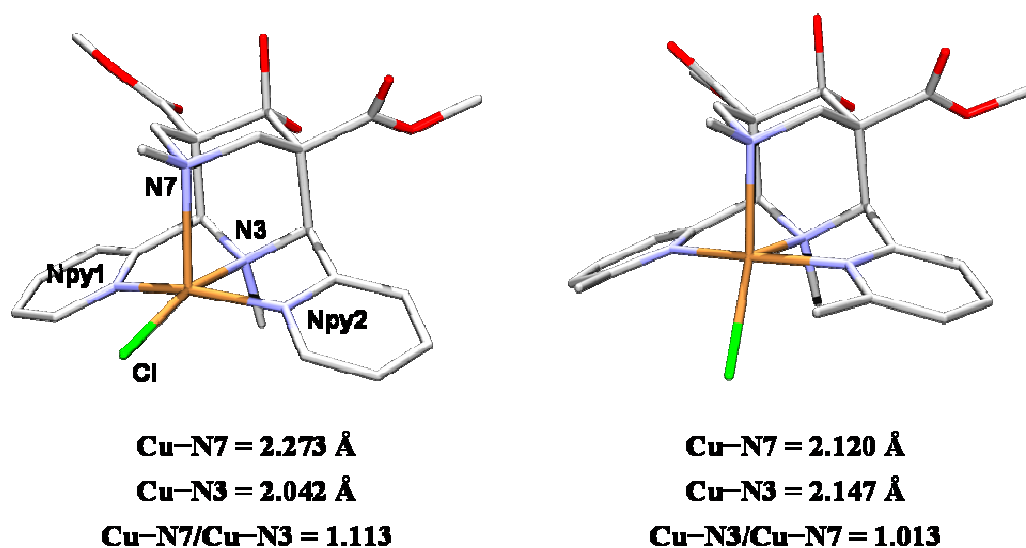


Figure 3.2. Crystal structures of $[\text{Cu}(\text{L}^{1\text{b}})(\text{Cl})]^+$ and $[\text{Cu}(\text{L}^{2\text{b}})(\text{Cl})]^+$

X-ray crystal structures of $[\text{Cu}(\text{L}^{2\text{b}})(\text{H}_2\text{O})]^{2+}$ [4] and $[\text{Cu}(\text{L}^{2\text{a}})(\text{CH}_3\text{CN})]^{2+}$ [2] are also known and the structure of $[\text{Cu}(\text{L}^{2\text{b}})(\text{H}_2\text{O})]^{2+}$ is similar to that of $[\text{Cu}(\text{L}^{2\text{b}})(\text{Cl})]^+$, with the water molecule bound *trans* to N7. In contrast is the structure of $[\text{Cu}(\text{L}^{2\text{a}})(\text{CH}_3\text{CN})]^{2+}$, in which the sterically less demanding acetonitrile is bound *trans* to N3, like the chloride in $[\text{Cu}(\text{L}^{1\text{b}})(\text{Cl})]^+$, but with an N7–Cu–Nac angle (ac = acetonitrile) significantly smaller than the N7–Cu–Cl angle in $[\text{Cu}(\text{L}^{1\text{b}})(\text{Cl})]^+$ (90.94° vs. 109.95°), indicating a distortion of the square-pyramidal geometry due to the steric interaction of the methyl groups with the acetonitrile co-ligand.

In contrast to the square-pyramidal structures found for complexes with the co-ligands Cl^- , H_2O and CH_3CN , are the crystal structure of $[\text{Cu}(\text{L}^{1\text{b}})(\text{NO}_3)]^+$ and $[\text{Cu}(\text{L}^{2\text{b}})(\text{NO}_3)]^+$ [4]. Due to the bidentate coordination of the nitrate ion, the crystal structure of $[\text{Cu}(\text{L}^{1\text{b}})(\text{NO}_3)]^+$ has a distorted octahedral geometry with an elongated Cu–N7 bond (as in $[\text{Cu}(\text{L}^{1\text{b}})(\text{Cl})]^+$). The steric interaction of the methyl groups with the nitrate ion in $[\text{Cu}(\text{L}^{2\text{b}})(\text{NO}_3)]^+$ again leads to a change in the Jahn-Teller axis, but this time to a structure with elongated Cu–Npy bonds. Possible reasons for this are discussed in Section 3.3.1.

3. The Copper(II) Complexes of tetradentate 3,7-Diazabicyclo[3.3.1]nonane Derivatives

For the ligand L^{2b} therefore, all three “Jahn-Teller isomers” can be isolated, with the elongated axis lying along the Cu–N7 ($[\text{Cu}(L^{2a})(\text{CH}_3\text{CN})]^{2+}$), Cu–N3 ($[\text{Cu}(L^{2b})(\text{H}_2\text{O})]^{2+}$ and $[\text{Cu}(L^{2b})(\text{Cl})]^+$) and Cu–Npy ($[\text{Cu}(L^{2b})(\text{NO}_3)]^+$) bonds respectively, simply by changing the size and/or denticity of the co-ligand^[4].

It is important to note that, in all the crystal structures but that of $[\text{Cu}(L^{2a})(\text{CH}_3\text{CN})]^{2+}$, the C=O group at C9 on the bispidine backbone (see Figure 1.1) has been hydrolysed to $\text{C}(\text{OH})_2$. This is common when non-anhydrous solvents are used in the synthesis of the complexes. Note that the copper(I) acetonitrile complexes discussed in Chapter 1, which are air and moisture sensitive, are prepared in a protected atmosphere with anhydrous acetonitrile as solvent and therefore all contain the original, ketone-substituted ligand. It is known that the ketone group at C9 leads to a decrease in the nucleophilicity of the amine donors and one therefore expects a decrease in the bond distances to the metals centre when this group is hydrolysed^[5]. For this reason, both forms of the ligand (see Figure 3.1) are considered here.

In the first section, the Jahn-Teller isomerism in the copper(II) complexes of tetradentate bispidine ligands with Cl^- , H_2O , CH_3CN and NO_3^- as co-ligand, is investigated. The potential energy surface around the metal coordination centre is explored, as well as the effect on the metal centre of hydrolysis of the C=O group at C9 of the bispidine backbone. The nature of the binding sites *trans* to the tertiary amine donors N3 and N7 are investigated more closely. We show that the geometry favoured by the bispidine, regardless of the size, nature and denticity of the co-ligand, is one in which the Cu–X bond (where X is the co-ligand) is approximately co-planar with the two pyridine rings and the Cu–N7 bond is elongated, in agreement with experiment and with previous computational studies^[6]. However, geometries with elongated Cu–N3 or Cu–Npy bonds can be induced by choice of co-ligand and/or substitution in the *ortho* position on the pyridine rings.

In the second section, the electronic structure of the $[\text{Cu}(L)(\text{Cl})]^+$ complexes, in particular the spin density distribution in the complex and the molecular orbitals of the valence shell, is investigated, in order to better understand the geometries enforced by the bispidine ligand. The results indicate that there may be some bonding interaction between the π -bonding

3. The Copper(II) Complexes of tetradentate 3,7-Diazabicyclo[3.3.1]nonane Derivatives

orbitals of the pyridine rings and the p-orbitals of the co-ligand, which could play a role in determining the orientation of the Cu–X unit with respect to the pyridine rings.

Finally, the inability of the hybrid DFT methods to predict the correct relative energies of the Jahn-Teller isomers of the $[\text{Cu}(\text{L})(\text{Cl})]^+$ complexes is addressed, and a modified hybrid density functional approach is used to adjust the ground-state atomic spin density in $[\text{Cu}(\text{L}^{\text{a}})(\text{Cl})]^+$ to the “experimental” spin density (determined from EPR spectroscopy). The experimentally calibrated functional is then applied to the calculation of the relative energies of isomers in the $[\text{Cu}(\text{L})(\text{Cl})]^+$ complexes.

An important result is that the modified functional does not lead to an improvement of the relative energies and gives overall poorer geometries in comparison to functionals containing Becke’s 3-parameter hybrid exchange functional. The reasons for this are explored and are concluded to lie largely in the incorrect prediction of the copper bond distances to the tertiary amines N3 and N7. The correct choice of correlation functional and the inclusion of solvent effects, leads to a significant improvement in the results.

3.2. Computational Methods

Initial DFT calculations were performed with Gaussian03^[7] using the B3LYP functional^[8]. For the geometry optimisations, the same basis set combination as used for the copper(I) complexes in Chapter 1, was used (refer to Section 2.2). Wave function stability tests were performed on selected optimised structures and all optimised structures were verified as true minima by frequency calculations. For the $[\text{Cu}(\text{L})(\text{Cl})]^+$ complexes, SP energy calculations were performed on the optimised geometries at the B3LYP/6-311G+(3df,2pd) level. This increase in the size of the basis set and the number of polarisation functions was found to have a minimal effect on the relative energies and SP calculations were not performed for the remaining compounds. The energies discussed here are therefore those calculated with the 6-311G+(d)/6-31G (heavy atoms/hydrogen) combination. The model system defined in Section 2.2 was also used throughout.

The ligands containing a C=O group at C9 are convenient from the computational point of view, due to the possibility of decreasing the computational cost by imposing C_s symmetry on the corresponding complexes. It is known that the ketone group at C9 leads to a decrease in the nucleophilicity of the amine donors and one therefore expects an increase in the bond distances to the metals centre, but the effect of this modification on the potential energy surfaces was not known. For this reason calculations were performed on the $[\text{Cu}(\text{L})(\text{Cl})]^+$ complexes using both forms of the ligand. When this was found to have a negligible effect on relative energies and the position of potential energy minima (see Section 3.3.1 and Table 3.1) the ligand with a C=O group at C9 was used in all further calculations.

The effect of the functional on the relative energies, geometries and spin densities was studied using a 6-31G(d) basis set and various common functionals implemented in Gaussian03 (see Section 3.3.3 below for details). Since the structures had been shown to be minima on the potential energy surface, frequency calculations were not performed and the energies quoted in this section are therefore without zero-point or thermal corrections. For the non-standard functionals, the adjustment of the amount of density functional exchange and correlation was achieved using the IOP keywords of the Gaussian03. The options 76, 77 and

3. The Copper(II) Complexes of tetradentate 3,7-Diazabicyclo[3.3.1]nonane Derivatives

78 of Overlay 3 were used to construct the density functional from local and non-local density functional exchange, local and non-local density functional correlation and Hartree-Fock exchange, according to equations (1) and (2) for BLYP and BP86 respectively, where $a = (\% E_{XHF})/100$. For the functionals with LYP correlation, the amount of non-local exchange was fixed at 0.72 (the experimentally calibrated value for B3LYP) and only the local exchange was varied, whereas for the BP86 functional, both the non-local and local DF exchange were varied, in analogy to the recent study on $CuCl_4$ ^[9].

$$E_{XC}(BLYP) = E_{CLSDA} + 0.72\Delta E_{XB88} + aE_{XHF} + (1-a)E_{XLSDA} + 0.81\Delta E_{CLYP} \quad (1)$$

$$E_{XC}(BP86) = E_{CLSDA} + (1-a)\Delta E_{XB88} + aE_{XHF} + (1-a)E_{XLSDA} + \Delta E_{CP86} \quad (2)$$

Spin densities were calculated using the Mulliken's Population Analysis (MPA)^[10] method. The decision to use only a double- ξ basis set and to employ only one of many possible population analysis methods is not arbitrary. Since the aim of this section is to adjust the functional empirically, the use of a relatively simple and time effective computational setup is justified.

Selected geometry optimisations were repeated with the ADF software package^[11], using the BP86 functional and a triple- ξ basis set. The energy decomposition analysis (EDA)^[12] was also performed with ADF at the same level of theory. In an EDA, the interaction energy between fragments of a molecule (ΔE_{int}) is decomposed into three main components, according to equation (3).

$$\Delta E_{int} = \Delta E_{elstat} + \Delta E_{Pauli} + \Delta E_{orb} \quad (3)$$

The ΔE_{elstat} term describes the electrostatic interaction between the fragments, ΔE_{Pauli} refers to the closed shell Pauli repulsive interaction and ΔE_{orb} is the electronic stabilization term, calculated in the final step of the EDA analysis, when the Kohn-Sham orbitals are allowed to relax to their final form.

3. The Copper(II) Complexes of tetradentate 3,7-Diazabicyclo[3.3.1]nonane Derivatives

Molecular orbitals and Mulliken spin densities were plotted using the program gOpenmol^[13] and unless otherwise indicated, an contour level of 0.04 was used. Frequencies were studied using the program GaussView for Windows^[14].

Unless explicitly stated otherwise, the results discussed below are those calculated with Gaussian03 using the B3LYP functional (as outlined above).

3.3. Results and Discussion

3.3.1. Geometries, isomerism and substrate binding strengths

Cu(II) complexes with Cl⁻ as co-ligand

Calculations with ligands L¹, L² and L³, indicate that the electronically favoured coordination geometry of the bispidone ligand is the square-pyramidal structure with the Cl⁻ coordinated *trans* to N3 and the Cu–N7 bond elongated, in agreement with experiment^[1,2]. Indeed, the same geometry is observed in the pentacoordinate complexes of L¹ with other metals such as Cu(I) and Zn(II). Substitution at the *ortho* position on the pyridine rings leads to a distortion of this minimum and gives rise to a second minimum, in which the Cl⁻ coordinates *trans* to N7 and the Cu–N3 bond is forced into the axial position.

Calculated and experimental geometric parameters for the [Cu(L)(Cl)]⁺ complexes are summarised in Table 3.1. The experimental structures are well reproduced, with the exception of a slight overestimation of the bond lengths and an incorrect prediction of the Cu–N7/Cu–N3 ratio in [Cu(L^{2b})(Cl)]⁺. For L¹ the only minimum is the *trans* N3 structure, which is in agreement with the known crystal structure of [Cu(L^{1b})(Cl)]⁺. For L² and L³ both a *trans* N3 and a *trans* N7 isomer are found. The two calculated *trans* N7 structures are almost identical, with N7–Cu–Cl angles of 166.90° (L^{2a}) and 165.66° (L^{3a}) respectively (see Figure 3.3(a)), and the calculated *trans* N7 isomer of [Cu(L^{1b})(Cl)]⁺ is in good agreement with the known crystal structure of this complex. Interesting are the changes in the structure of the *trans* N3 isomers when going from L^{1a} to L^{3a} to L^{2a} (increasing size of the R₁ group). There is a steady decrease in the N7–Cu–Cl angle from 106.57° (L^{1a}) to 98.99° (L^{3a}) to 94.70° (L^{2a}) and a corresponding decrease in the Npy–Cu–Npy angle, from 157.51° for L^{1a}, to 147.35° and 147.26° for L^{3a} and L^{2a} respectively. This distortion of the square-pyramidal geometry towards trigonal-bipyramidal seems to be a result of an attempt of the co-ligand and the increasingly more sterically demanding R₁ group to avoid each other and is demonstrated in an overlay plot of the three structures, shown in Figure 3.3(b).

Table 3.1. Selected calculated and experimental geometric parameters for the $[\text{Cu}(\text{L})(\text{Cl})]^{2+}$ complexes, for $\text{L}^{1a/b}$ - $\text{L}^{3a/b}$ (see Figure 3.1). Experimental values are given in bold and italics

Ligand	L^{1a}	L^{1b}	L^{1b}	L^{2a}	L^{2b}	L^{2b}	L^{2a}	L^{2b}	L^{2a}	L^{2b}	L^{3a}	L^{3b}	L^{3a}	L^{3b}
Parameters	<i>trans</i> N3	<i>trans</i> N3	<i>trans</i> N3	<i>trans</i> N7	<i>trans</i> N7	<i>trans</i> N7	<i>trans</i> N3	<i>trans</i> N3	<i>trans</i> N7	<i>trans</i> N7	<i>trans</i> N7	<i>trans</i> N3	<i>trans</i> N3	<i>trans</i> N3
Bond distances (Å)														
Cu-N7	2.450	2.441	2.273	2.216	2.254	2.120	2.426	2.398	2.178	2.170	2.357	2.331	2.357	2.331
Cu-N3	2.098	2.094	2.042	2.209	2.213	2.147	2.058	2.056	2.268	2.265	2.087	2.082	2.087	2.082
Cu-Npy1	2.058	2.057	2.021	2.048	2.093	2.061	2.198	2.205	2.127	2.127	2.200	2.209	2.200	2.209
Cu-Npy2	2.058	2.057	2.024	2.048	2.092	2.064	2.198	2.204	2.127	2.126	2.200	2.208	2.200	2.208
Cu-Cl	2.223	2.228	2.232	2.262	2.259	2.221	2.209	2.212	2.220	2.223	2.187	2.189	2.187	2.189
Npy1...Npy2	4.037	4.036	3.971	4.060	4.139	4.084	4.218	4.226	4.177	4.179	4.223	4.232	4.223	4.232
N7...N3	3.034	3.026	2.921	3.024	3.037	2.930	3.032	3.019	3.036	3.027	3.015	3.003	3.015	3.003
Cu-N7/Cu-N3	1.168	1.165	1.113	1.003	1.018	0.987	1.179	1.166	0.960	0.958	1.129	1.119	1.129	1.119
Valence angles (°)														
N7-Cu-N3	83.30	83.34	85.03	86.22	85.68	86.71	84.67	84.99	86.11	86.05	85.25	85.55	85.25	85.55
Npy-Cu-Npy	157.51	157.71	158.13	164.93	163.11	163.83	147.26	146.85	158.19	158.52	147.35	146.79	147.35	146.79
N7-Cu-Npy	94.40	94.46	95.66	90.73	90.40	90.73	99.94	100.23	91.12	91.14	98.99	99.39	98.99	99.39
N3-Cu-Cl	170.13	169.78	165.02	106.88	109.08	112.97	179.37	179.72	108.23	108.11	175.87	175.12	175.87	175.12
N7-Cu-Cl	106.57	106.89	109.95	166.90	165.24	160.31	94.70	95.28	165.66	165.84	98.88	99.33	98.88	99.33
Npy-Cu-Cl	98.62	98.44	96.32	90.99	91.76	92.02	102.00	101.89	91.59	91.50	101.93	101.84	101.93	101.84
Torsion angles (°)														
N3-C-C-Npy1	33.13	32.66	33.65	45.62	45.61	45.23	26.64	26.18	48.39	48.14	30.19	29.48	30.19	29.48
N3-C-C-Npy2	-33.13	-32.66	-37.21	-45.62	-45.48	-46.02	-26.64	-26.24	-48.39	-48.07	-30.19	-29.57	-30.19	-29.57
Relative Energies (kJ/mol)														
Gas phase	0.00	0.00	-	10.85	11.09	-	0.00	0.00	5.00	5.25	0.00	0.00	0.00	0.00

Previous calculations have shown that the role of the bispidine backbone is to stabilise a square-pyramidal local minimum on the potential energy surface of a representative unrestricted model system $[\text{Cu}(\text{NH}_3)_2(\text{imine})_2(\text{Cl})]^+$ [6]. The effect of adding bulky substituents in the *ortho* position has a destabilising effect on this minimum, leading to a distortion in the direction of the trigonal-bipyramidal global minimum of the unrestricted model system.

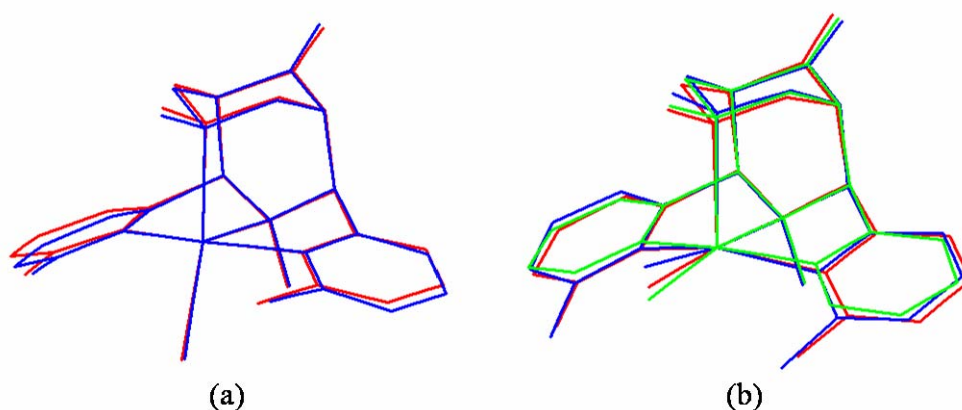


Figure 3.3. Overlay plot of the (a) *trans* N7 (L^{2a} , L^{3a}) and (b) *trans* N3 (L^{1a} , L^{2a} , L^{3a}) isomers of the $[\text{Cu}(\text{L})(\text{Cl})]^+$ complexes, green – L^{1a} , red – L^{3a} , blue – L^{2a}

The relative energies of the *trans* N3 and *trans* N7 isomers are also given in Table 3.1, for the ligands L^2 and L^3 . While the calculations predict the existence of a *trans* N7 isomer for L^2 and L^3 , with relatively good structural agreement for $[\text{Cu}(L^{2b})(\text{Cl})]^+$, this isomer is calculated to be less stable than the *trans* N3 isomer by 11 and 5 kJ/mol respectively, although this is the only geometry observed experimentally. An increase in the size of the basis set makes less than 1 kJ/mol difference in the relative energies. This problem and possible reasons for it are discussed in detail in the following two sections.

A *trans* N7 isomer is not found for L^1 and a potential energy surface scan, incrementing the N7–Cu–Cl angle of $[\text{Cu}(L^{1b})(\text{Cl})]^+$ between 90° and 180° in steps of 5° indicates that there is not even a shallow local minimum for *trans* N7 coordination. However, the possibility cannot be excluded that the reason for this lies, at least partially, in the artificial destabilisation of *trans* N7 isomer by the DFT calculations, manifest in the incorrect relative energies for L^2 and L^3 , and that a shallow minimum does exist which cannot be found at the current level of theory. An estimate of the energy of this hypothetical “isomer” can be obtained by optimising

the geometry of $[\text{Cu}(\text{L}^{\text{lb}})(\text{Cl})]^+$ while keeping the N7-Cu-Cl angle fixed at 166° . This leads to a structure with an energy 40 kJ/mol higher than that of the *trans* N3 minimum. Since the relative energies of the two isomers of $[\text{Cu}(\text{L}^{\text{2b}})(\text{Cl})]^+$ are incorrectly predicted by around 10 kJ/mol, this implies a destabilisation of the electronically favoured *trans* N3 geometry due to the steric effect of *ortho* substitution on the pyridine rings, of around 50 kJ/mol (depending on the size of the substituent).

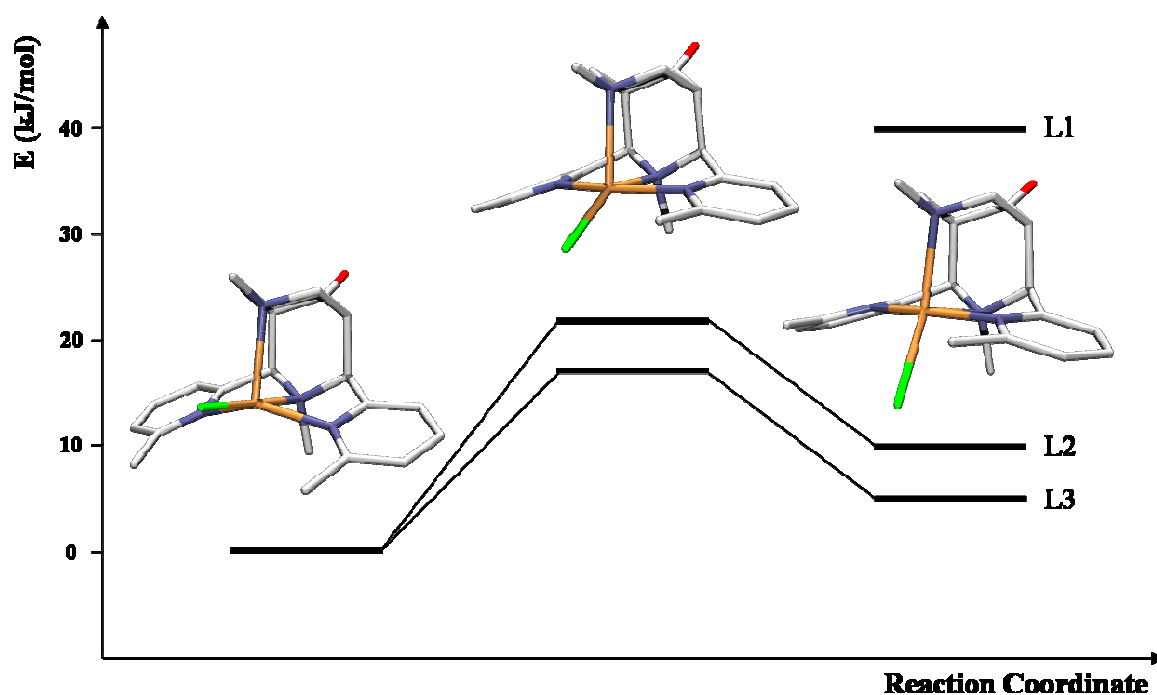


Figure 3.4. Schematic Representation of the PES of the $[\text{Cu}(\text{L})(\text{Cl})]^+$ complexes of L^{1a} , L^{2a} and L^{3a} , showing both isomers and the transition state for $[\text{Cu}(\text{L}^{\text{2a}})(\text{Cl})]^+$

Transition states between the *trans* N7 and *trans* N3 isomers of $[\text{Cu}(\text{L}^{\text{2a}})(\text{Cl})]^+$ and $[\text{Cu}(\text{L}^{\text{3a}})(\text{Cl})]^+$ were also optimised and the energy barriers are 22 and 17 kJ/mol respectively. The lower energy barrier for L^{3a} is probably due to the smaller steric repulsion between the co-ligand and the fluorine substituents. The geometries of the two transition states are similar, as is to be expected, with N7-Cu-Cl angles of 128.5° and 132.7° respectively. Figure 3.4 shows a schematic representation of the potential energy surface of $[\text{Cu}(\text{L})(\text{Cl})]^+$, for L^{1a} , L^{2a} and L^{3a} , including the optimised geometries of both isomers and the transition state for $[\text{Cu}(\text{L}^{\text{2a}})(\text{Cl})]^+$.

3. The Copper(II) Complexes of tetradentate 3,7-Diazabicyclo[3.3.1]nonane Derivatives

The above calculations were repeated with the software package ADF and the results agree both qualitatively and quantitatively with the Gaussian03 calculations^[15]. In particular, the *trans* N3 isomers are calculated to be more stable than the *trans* N7 isomers, by 10 and 6 kJ/mol for L^{2a} and L^{3a} respectively, with energy barriers of 24 and 21 kJ/mol. The restricted optimisation of a *trans* N7 “isomer” for [Cu(L^{1a})(Cl)]⁺ gives a destabilisation of 58 kJ/mol (compared to a Gaussian03 value of 40 kJ/mol).

The effect of the hydrolysed ligand backbone on the geometries and relative energies are shown in Table 3.1. The main changes are found in the bond distances, while variations in the angular geometry are negligible. In particular the non-bonded N3...N7 and Npy...Npy distances remain fairly constant. The general effect of the hydrolysis of the carbonyl group is, as expected, to decrease the copper–bispidine bond distances. This effect is most pronounced for the Cu–N7 bond distances in the *trans* N3 structures (the Jahn-Teller axis). The Cu–Cl bond distance is relatively unaffected, as is the orientation of the Cl⁻ with respect to the pyridine rings (an important effect in the stability of the complex).

The relative energies between the two isomers of [Cu(L²)(Cl)]⁺ and [Cu(L³)(Cl)]⁺ changes by less than 1 kJ/mol upon hydrolysis of the carbonyl group. Also, the spin density on the copper centre is virtually unaffected by the hydrolysis and the spin densities on the ligands are only slightly affected (see Section 3.3.3). In conclusion therefore, the changes in geometry and, more importantly, in electronic structure and relative energies between complexes with the original and the hydrolysed ligand, are negligible, making the ketone-based ligands valid and useful models for computational studies.

The location of both a *trans* N3 and a *trans* N7 isomer for L² and L³, provides the opportunity of comparing directly the binding strength of substrates in the respective positions, within the same complex. This is of interest in understanding the nature of the bonding in bispidine complexes in general, as well as the influence of the substrate binding site on the stability.

The simplest approach is to compare the bond lengths and stretching frequencies of the Cu–Cl bonds in the two isomers. The Cu–Cl stretching vibration in [Cu(L^{1a})(Cl)]⁺ has a frequency of 348.58 cm⁻¹. The analogous vibrational frequency in the *trans* N3 isomer with L^{2a} is lowered to 339.65 cm⁻¹, while that of the *trans* N7 isomer is at 304.54 cm⁻¹ ($\Delta\nu=35.11$ cm⁻¹). For L^{3a}

3. The Copper(II) Complexes of tetradentate 3,7-Diazabicyclo[3.3.1]nonane Derivatives

the vibrational frequencies are 351.71 and 327.78 cm^{-1} for the *trans* N3 and *trans* N7 isomers respectively ($\Delta\nu=25.93 \text{ cm}^{-1}$). For both ligands therefore, the Cu–Cl stretching vibration is significantly higher in energy in the *trans* N3 isomers than in the *trans* N7, indicating that substrate binding is stronger in this position. This is also reflected in the Cu–Cl bond lengths, which are around 0.05 Å shorter in the *trans* N3 than in the *trans* N7 isomers of L^2 and L^3 .

An estimate for the Cu–Cl bond energy can also be obtained by removing the Cl^- ion in the optimised structures of $[\text{Cu}(\text{L})(\text{Cl})]^+$ and calculating the energy of the CuL^{2+} fragment for the two isomers. When this is done for L^{2a} an energy difference of 16 kJ/mol is obtained, with the *trans* N7 CuL^{2+} fragment more stable. Since the energy of the *trans* N7 isomer is 11 kJ/mol higher than that of the *trans* N3 isomer, this implies that the binding strength of the Cl^- *trans* to N3 is 27 kJ/mol higher than *trans* to N7.

The strain energy of the ligand in the two isomers of $[\text{Cu}(\text{L}^{2a})(\text{Cl})]^+$ was also calculated, by removing the Cu–Cl unit and performing single point energy calculations on the ligand fragments L, fixed in their *trans* N3 and *trans* N7 geometries. The difference in strain energy between the two was found to be 9 kJ/mol, the *trans* N3 fragment being the most stable. This is in good agreement with the value of 10.6 kJ/mol calculated with ADF, while molecular mechanics calculations with MOMECC^[16,17] give the same relative strain energies (L more stable *trans* N3 than *trans* N7) but smaller absolute values^[18].

The results of the EDA for $[\text{Cu}(\text{L}^{1a})(\text{Cl})]^+$, $[\text{Cu}(\text{L}^{2a})(\text{Cl})]^+$ and $[\text{Cu}(\text{L}^{3a})(\text{Cl})]^+$ are summarised in Table 3.2^[15]. The total attractive interaction is due to ΔE_{elstat} and ΔE_{orb} , and the percentage contribution of these terms to the total attractive interaction is given in parentheses. For $[\text{Cu}(\text{L}^{2a})(\text{Cl})]^+$ the components of ΔE_{int} (see Section 3.2 for definition) reveal that, while the repulsive Pauli interaction and the attractive electrostatic interaction stabilise *trans* N3 relative to *trans* N7 by approximately 34 kJ/mol, this is partly compensated by the attractive orbital interaction, which favours *trans* N7 by circa 23 kJ/mol.

The EDA with Cl^- , Cu^{2+} and L treated as separate fragments (Cl–Cu–L) and that with CuCl^+ and L treated as separate fragments (CuCl–L) stabilise the *trans* N7 isomer by 1 and 6 kJ/mol respectively. Here, the stabilising electrostatic and orbital interactions favour *trans* N7 binding, while Pauli interactions favour *trans* N3. In both cases the attractive interactions

3. The Copper(II) Complexes of tetradentate 3,7-Diazabicyclo[3.3.1]nonane Derivatives

dominate over the repulsive term, resulting in a total stabilisation of *trans* N7 over *trans* N3. A further calculation, performed with CuL^{2+} and Cl^- fragments ($\text{CuL}-\text{Cl}$), results in a stabilisation of the *trans* N3 isomer by around 150 kJ/mol. Here, the total attractive interactions, due to ΔE_{elstat} and ΔE_{orb} , are significantly different for the two isomers.

The EDA of $[\text{Cu}(\text{L}^{3a})(\text{Cl})]^+$ yields qualitatively similar results to that of $[\text{Cu}(\text{L}^{2a})(\text{Cl})]^+$. For $[\text{Cu}(\text{L}^{3a})(\text{Cl})]^+$ a *trans* N7 isomer was not located and the *trans* N3 isomer with a constrained N7–Cu–Cl angle of 165° (as found in *trans* N7 $[\text{Cu}(\text{L}^{2a})(\text{Cl})]^+$) was used in the analysis.

Table 3.2. Energy decomposition analysis of $[\text{Cu}(\text{L}^{2a})(\text{Cl})]^+$ (*trans* N3 and *trans* N7)^[15]; ΔE 's given in kJ/mol

		L	L-Cu-Cl	L-CuCl	LCu-Cl
<i>trans</i> N3 $[\text{Cu}(\text{L}^{1a})(\text{Cl})]^+$	ΔE_{int}	-27444.8	-2619.8	-732.2	-927.9
	ΔE_{Pauli}	107890.7	914.2	783.0	515.1
	ΔE_{elstat}	-22821.6 (16.9 %)	-2307.7 (65.3 %)	-823.5 (54.3 %)	-1034.3 (71.7 %)
	ΔE_{orb}	-112513.8 (83.1 %)	-1226.3 (34.7 %)	-691.7 (45.7 %)	-408.8 (28.3 %)
<i>trans</i> N7 $[\text{Cu}(\text{L}^{1a})(\text{Cl})]^+$	ΔE_{int}	-27441.0	-2561.8	-674.2	-870.0
	ΔE_{Pauli}	108056.0	975.6	879.0	531.5
	ΔE_{elstat}	-22859.9 (16.9 %)	-2312.4 (65.4 %)	-866.8 (55.8 %)	-1003.5 (71.6 %)
	ΔE_{orb}	-112637.1 (83.1 %)	-1225.1 (34.6 %)	-686.4 (44.2 %)	-398.1 (28.4 %)
<i>trans</i> N3 $[\text{Cu}(\text{L}^{2a})(\text{Cl})]^+$	ΔE_{int}	-30618.4	-2586.4	-697.8	-1014.5
	ΔE_{Pauli}	118587.0	842.8	649.9	548.7
	ΔE_{elstat}	-24937.3 (16.7 %)	-2244.9 (65.5 %)	-723.5 (53.7 %)	-1014.9 (64.9 %)
	ΔE_{orb}	-124268.3 (83.3 %)	-1184.3 (34.5 %)	-624.2 (46.3 %)	-548.2 (35.1 %)
<i>trans</i> N7 $[\text{Cu}(\text{L}^{2a})(\text{Cl})]^+$	ΔE_{int}	-30607.8	-2587.2	-703.4	-857.1
	ΔE_{Pauli}	118613.8	888.3	795.8	513.2
	ΔE_{elstat}	-24930.5 (16.7 %)	-2246.4 (64.6 %)	-814.6 (54.3 %)	-1001.3 (73.1 %)
	ΔE_{orb}	-124290.9 (83.3 %)	-1229.2 (35.4 %)	-684.7 (45.7 %)	-369.0 (26.9 %)
<i>trans</i> N3 $[\text{Cu}(\text{L}^{3a})(\text{Cl})]^+$	ΔE_{int}	-27542.3	-2527.9	-637.5	-913.1
	ΔE_{Pauli}	110597.0	814.5	617.5	498.8
	ΔE_{elstat}	-23802.6 (17.2 %)	-2163.8 (64.7 %)	-691.3 (55.1 %)	-1015.2 (71.9 %)
	ΔE_{orb}	-114336.7 (82.8 %)	-1178.6 (35.3 %)	-563.4 (44.9 %)	-396.7 (28.1 %)
<i>trans</i> N7 $[\text{Cu}(\text{L}^{3a})(\text{Cl})]^+$	ΔE_{int}	-27534.0	-2530.2	-644.4	-869.6
	ΔE_{Pauli}	110533.6	861.3	755.9	450.0
	ΔE_{elstat}	-23769.2 (17.2 %)	-2176.3 (64.2 %)	-767.4 (54.8 %)	-970.7 (73.6 %)
	ΔE_{orb}	-114298.3 (82.8 %)	-1215.2 (35.8 %)	-632.8 (45.2 %)	-348.9 (26.4 %)

3. The Copper(II) Complexes of tetradentate 3,7-Diazabicyclo[3.3.1]nonane Derivatives

The stabilisation of the *trans* N3 isomer is therefore due primarily to the preference of the ligand for the *trans* N3 coordination geometry and a large stabilising orbital interaction energy for *trans* N3 coordination. This supports one of the most important observations in copper(II) bispidine coordination chemistry, namely that the orbital interactions strongly favour coordination of substrates *trans* to N3.

In summary, all fragment type calculation show that *trans* N3 binding is more favourable than *trans* N7 binding, in agreement with experiment. The percentage of the attractive interaction remains constant for both isomers in all calculations. For all fragment type calculations ΔE_{int} of the *trans* N3 isomer is approximately 60 kJ/mol lower in energy than that of *trans* N7.

Cu(II) complexes with H₂O as co-ligand

Calculations have been performed for $[\text{Cu}(\text{L}^{2a})(\text{H}_2\text{O})]^{2+}$ and the isomerism is analogous to $[\text{Cu}(\text{L}^{2a})(\text{Cl})]^+$, in that both a *trans* N3 and a *trans* N7 isomer are found^[19]. The calculated (L^{2a}) and experimental (L^{2b}) geometries are summarised in Table 3.3. As for $[\text{Cu}(\text{L}^{2a})(\text{Cl})]^+$, the qualitative agreement between the calculated and experimental structures is reasonable, but here too the Cu–N7/Cu–N3 ratio is incorrectly predicted. The *trans* N3 isomer is also predicted to be more stable than the *trans* N7 isomer (by 5 kJ/mol), although experimentally only the *trans* N7 isomer has been isolated. The same result is obtained with ADF, with an energy difference of 7 kJ/mol. It is interesting to note that the Cu–O_{aqua} bond *trans* to N3 is 0.15 Å shorter than *trans* to N7, as opposed to only 0.05 Å for Cu–Cl in $[\text{Cu}(\text{L}^{2a})(\text{Cl})]^+$. This is probably due to the fact that the Cu–Cl bond is stronger to begin with, because of the negatively charged Cl[–] ion, so that the differences between the *trans* N3 and *trans* N7 sites are less pronounced than for H₂O.

Table 3.3. Calculated and experimental geometric parameters of the $[\text{Cu}(\text{L}^2)(\text{X})]^{2+}$ complexes, for X=H₂O, CH₃CN; experimental values given in italics

Ligands	L^{2a} , X=H ₂ O	L^{2a} , X=H ₂ O	L^{2b} , X=H ₂ O	L^{2a} , X=CH ₃ CN	L^{2a} , X=CH ₃ CN
Parameters	<i>trans</i> N3	<i>trans</i> N7	<i>trans</i> N7	<i>trans</i> N3	<i>trans</i> N3
Bond lengths (Å)					
Cu-N7	2.355	2.239	2.087	2.376	2.376
Cu-N3	2.013	2.144	2.133	2.029	2.004
Cu-Npy1	2.138	2.017	2.029	2.145	2.052
Cu-Npy2	2.138	2.017	2.015	2.145	2.075
Cu-X	2.032	2.190	1.991	2.012	1.951
Cu-N7/Cu-N3	1.170	1.044	0.978	1.171	1.186
N7...N3	3.028	3.080	2.930	3.029	2.934
Npy...Npy	4.149	4.004	4.013	4.130	4.034
Bond angles (°)					
N7-Cu-N3	87.38	89.28	87.94	86.50	83.66
Npy-Cu-Npy	152.05	166.18	165.60	148.65	155.63
N7-Cu-X	92.49	163.54	161.61	92.59	90.94
Bond torsions (°)					
N3-C-C-Npy1	30.56	43.29	43.08	28.30	26.08
N3-C-C-Npy2	-30.56	-43.29	-40.00	-28.30	-29.89

3. The Copper(II) Complexes of tetradentate 3,7-Diazabicyclo[3.3.1]nonane Derivatives

Rigid PES scans have been performed on the two isomers of $[\text{Cu}(\text{L}^{2a})(\text{H}_2\text{O})]^{2+}$, varying the $\text{Cu}-\text{O}_{\text{aqua}}$ distance between 2.0 and 4.0 Å (see Figure 3.5), and these reveal that the energy required to remove the *trans* N7 bound H_2O molecule is approximately 35 kJ/mol less than the energy required *trans* to N3 (without taking the rearrangement of the CuL fragment into account). This is in the same region as the difference in binding energy of 27 kJ/mol calculated for the two isomers of $[\text{Cu}(\text{L}^{2a})(\text{Cl})]^+$.

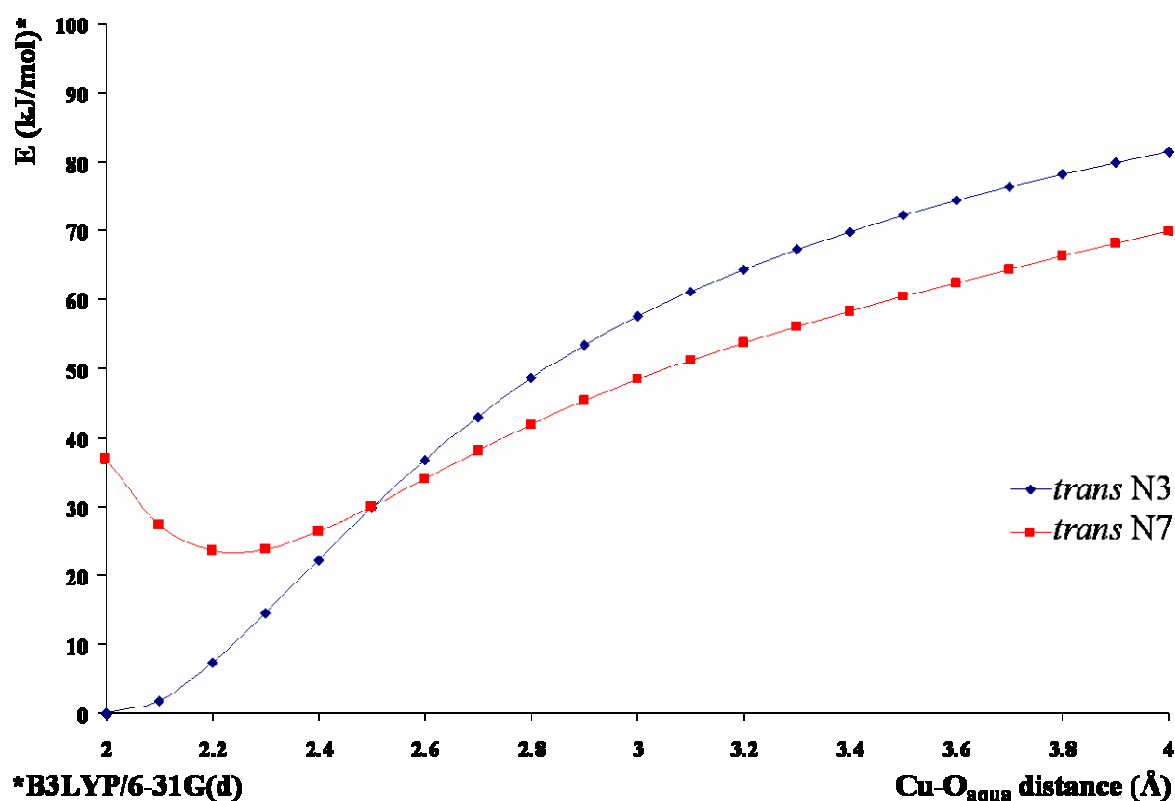


Figure 3.5. Rigid PES scan of the $\text{Cu}-\text{O}_{\text{aqua}}$ distance in $[\text{Cu}(\text{L}^{2a})(\text{H}_2\text{O})]^{2+}$, *trans* N3 and *trans* N7, with the energies normalised to the *trans* N3 global minimum

Cu(II) complexes with CH₃CN as co-ligand

Calculations were also performed on the $[\text{Cu}(\text{L}^{2a})(\text{CH}_3\text{CN})]^{2+}$ complex with the acetonitrile coordinated *trans* to N3 and the experimental and calculated structures are given in Table 3.3. The agreement between experimental and calculated structures is good, the only significant difference being in the orientation of the acetonitrile ligand, which is due to the C_s symmetry in the calculated structure. The isomerism in this complex has been investigated computationally^[20] and a *trans* N7 isomer is located, which is higher in energy than that of the *trans* N3 isomer. In this case therefore, the calculations are in agreement with the experiment, both favouring the *trans* N3 position. This is an indication of the subtle balance between the steric effect of the *ortho* substituent and that of the co-ligand and is further verification for the electronic stabilisation of the *trans* N3 position by the bispidine ligand.

A comparison of the calculated and experimental *trans* N3 structures of $[\text{Cu}(\text{L}^{2a})(\text{CH}_3\text{CN})]^{2+}$ with the calculated *trans* N3 isomers of $[\text{Cu}(\text{L}^{2a})(\text{Cl})]^+$ and $[\text{Cu}(\text{L}^{2a})(\text{H}_2\text{O})]^+$, reveals that their geometries with respect to the copper(II) coordination site are practically identical, which provides validation for the calculated geometries of the *trans* N3 isomers of $[\text{Cu}(\text{L}^{2a})(\text{Cl})]^+$ and $[\text{Cu}(\text{L}^{2a})(\text{H}_2\text{O})]^+$. Figure 3.6(a) shows an overlay of the calculated and experimental structures of $[\text{Cu}(\text{L}^{2a})(\text{CH}_3\text{CN})]^{2+}$ and an overlay of the calculated *trans* N3 structures of $[\text{Cu}(\text{L}^{2a})(\text{CH}_3\text{CN})]^{2+}$, $[\text{Cu}(\text{L}^{2a})(\text{Cl})]^+$ and $[\text{Cu}(\text{L}^{2a})(\text{H}_2\text{O})]^+$ are shown in Figure 3.6(b).

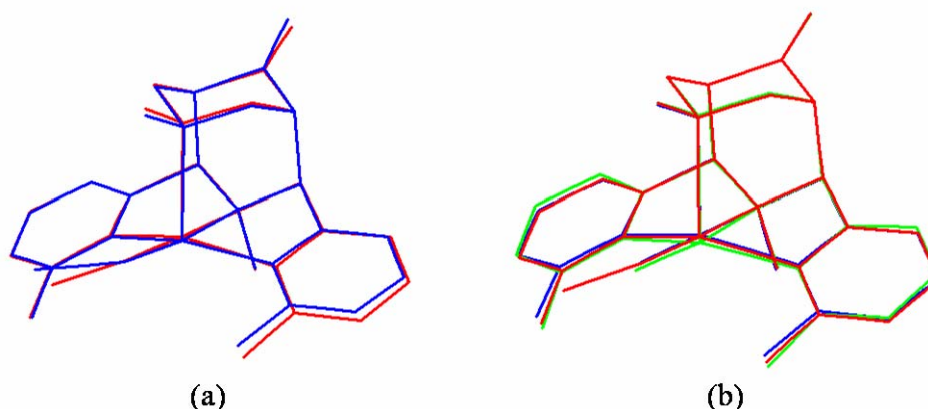


Figure 3.6. Overlay plots of (a) $[\text{Cu}(\text{L}^{2a})(\text{CH}_3\text{CN})]^{2+}$, calculated (red) and experimental (blue), and (b) the calculated structures of $[\text{Cu}(\text{L}^{2a})(\text{CH}_3\text{CN})]^{2+}$ (red), $[\text{Cu}(\text{L}^{2a})(\text{Cl})]^+$ (blue) and $[\text{Cu}(\text{L}^{2a})(\text{H}_2\text{O})]^+$ (green)

Cu(II) complexes with NO₃⁻ as co-ligand

Copper(II) bispidone complexes with NO₃⁻ as co-ligand are known for L^{1b} and L^{2b}. In both structures the nitrate ion coordinates as a bidentate ligand and the resulting complexes therefore have distorted octahedral geometries, which differ however with respect to the Jahn-Teller axis. As observed in the copper(II) complexes with monodentate co-ligands, [Cu(L^{1b})(NO₃)]⁺ has a structure with an elongated Cu–N7 bond. Once again the addition of an *ortho* substituent on the pyridine rings destabilises this minimum, but in this case to a structure with elongated Cu–Npy bonds, as in the crystal structure of [Cu(L^{2b})(NO₃)]⁺. Relevant geometric parameters (calculated and experimental) are summarised in Table 3.3 below and the structures of the global minima are shown in Figure 3.7.

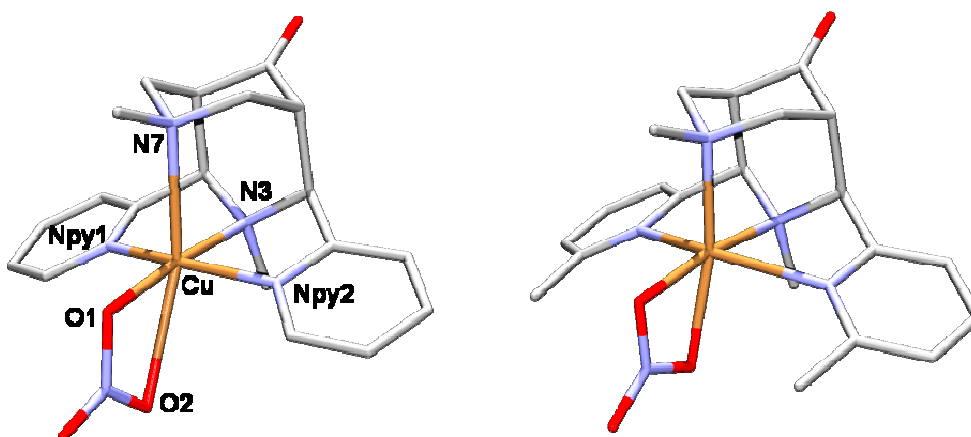


Figure 3.7. The calculated structures of [Cu(L^{1a})(NO₃)]⁺ and [Cu(L^{2a})(NO₃)]⁺

While the bond lengths in the calculated structures of [Cu(L^{1a})(NO₃)]⁺ and [Cu(L^{2a})(NO₃)]⁺ differ quantitatively from those of the crystal structures, this is probably largely due to the different substituent at C9 (see Figure 3.1), and there is nonetheless a correspondence with respect to the Jahn-Teller axis. The calculated structure of [Cu(L^{3a})(NO₃)]⁺ is similar to that of [Cu(L^{2a})(NO₃)]⁺, in that the Cu–Npy bond is elongated. The extent of the elongation differs however, and the Cu–Npy bond lengths are shorter with L^{3a} than with L^{2a}.

The elongation of the Cu–Npy bonds can be explained on the basis of the steric interaction of the *ortho* substituents with the co-ligand, which destabilises the electronically favoured geometry with an elongated Cu–N7 bond. The options of alleviating this steric strain

3. The Copper(II) Complexes of tetradentate 3,7-Diazabicyclo[3.3.1]nonane Derivatives

available in complexes with a monodentate co-ligand X (decreasing the N7–Cu–X angle or coordination of X *trans* to N7), are not available for the $[\text{Cu}(\text{L}^{1\text{b}})(\text{NO}_3)]^+$ complexes, due to the restraints imposed by the chelate ring formed by the nitrate ion, so that the only remaining possibility of alleviating the steric strain is an increase in the Cu–Npy bond lengths.

Table 3.3. Calculated and experimental geometric parameters of the $[\text{Cu}(\text{L})(\text{NO}_3)]^+$ complexes, for $\text{L}^1\text{-L}^3$; experimental values given in italics

Ligand	$\text{L}^{1\text{a}}$	$\text{L}^{1\text{b}}$	$\text{L}^{2\text{a}}$	$\text{L}^{2\text{b}}$	$\text{L}^{3\text{a}}$
Parameters	Cu-N7 long	<i>Cu-N7 long</i>	Cu-Npy long	<i>Cu-Npy long</i>	Cu-Npy long
Bond lengths (Å)					
Cu-N7	2.440	2.291	2.106	2.092, 2.032	2.093
Cu-N3	2.066	2.001	2.054	1.976, 1.987	2.091
Cu-Npy1	2.064	2.010	2.479	2.259, 2.377	2.456
Cu-Npy2	2.064	2.008	2.479	2.347, 2.376	2.456
Cu-O1	1.950	1.970	2.005	1.964, 1.982	2.006
Cu-O2	2.589	2.641	2.118	2.283, 2.139	2.068
Cu-N7/Cu-N3	1.181	1.145	1.025	1.059, 1.023	1.001
N7...N3	3.029	2.903	2.933	2.853, 2.834	2.939
Bond angles (°)					
N7-Cu-N3	84.04	84.84	89.64	89.00, 89.69	89.25
Npy1-Cu-Npy2	160.23	161.56	149.73	155.60, 152.54	148.67
N7-Cu-O1	101.81	103.81	100.11	99.63, 100.56	101.20
N7-Cu-O2	157.28	157.19	162.99	159.50, 163.35	164.89
Bond torsions (°)					
N3-C-C-Npy1	34.50	33.74	44.13	41.88, 41.70	45.11
N3-C-C-Npy2	-34.50	-30.23	-44.13	-42.16, 44.80	-45.11

*Two independent X-ray structures

Numerous attempts to isolate the corresponding local minima for these three compounds have as been unsuccessful and it is doubtful these local minima exist. Optimisations constraining the Cu–Npy (for $\text{L}^{1\text{a}}$) and Cu–N7 (for $\text{L}^{2\text{a}}$ and $\text{L}^{3\text{a}}$) bond lengths to the values found in the calculated structures of the corresponding local minima lead to a destabilisation of the resulting structures by only 10 to 15 kJ/mol, but the structures all converge to their global minima as soon as the constraints are removed.

3.3.2. Electronic structure of the $[\text{Cu}(\text{L})(\text{Cl})]^+$ complexes

Previous DFT calculations have shown that the bispidine ligand L^1 does not induce steric strain on the CuCl^+ fragment, but yields a coordination geometry which is similar to a local minimum on the potential energy surface of the unstrained $[\text{Cu}(\text{NH}_3)_2(\text{imine})_2(\text{Cl})]^+$ complex^[6]. In this local minimum of $[\text{Cu}(\text{NH}_3)_2(\text{imine})_2(\text{Cl})]^+$ the $\text{C}_{\text{ar}}-\text{N}_{\text{ar}}-\text{Cu}-\text{Cl}$ torsion angle (ar = aromatic) has a value of around 15° . The corresponding torsion angles in calculated structures of $[\text{Cu}(\text{L}^{1\text{a}})(\text{Cl})]^+$ and the *trans* N3 isomers of $[\text{Cu}(\text{L}^{3\text{a}})(\text{Cl})]^+$ and $[\text{Cu}(\text{L}^{2\text{a}})(\text{Cl})]^+$ are 9, 16 and 22° respectively. The reason for the stabilisation of this geometry has not yet been unambiguously assigned and for this reason the electronic structure of $[\text{Cu}(\text{L}^{1\text{a}})(\text{Cl})]^+$, in particular the molecular orbitals in the outer valence shell and the location of the unpaired electron, was investigated. Molecular orbitals from restricted open-shell (RO) DFT calculations were used for the analysis, since these give a more intuitive molecular orbital picture than the α and β orbitals of unrestricted DFT calculations.

We define our coordinate system so that the $\text{Cu}-\text{N7}$ bond lies along the z-axis, the $\text{Cu}-\text{Npy}$ bonds along the x-axis and the $\text{Cu}-\text{Cl}$ bond along the y-axis. The HOMO of $[\text{Cu}(\text{L}^{1\text{a}})(\text{Cl})]^+$ is the σ antibonding combination of a $\text{Cu}(\text{d}_{x^2-y^2})$, the p_y orbitals of Cl and N3 and the p_x orbitals of the Npy 's (Figure 3.8(a)), as one would expect for a square-pyramidal d^9 copper(II) complex. The HOMO-1 is the σ/π antibonding combination of the $\text{Cu}(\text{d}_{z^2})$ orbital and the p_z orbitals of N7/Cl respectively. The HOMO-2 is an almost completely localised $\text{Cl}(\text{p}_x)$ orbital with a small percentage of d_{xy} character, while the HOMO-3 is the π bonding combination of the HOMO-1. The HOMO-4 has no $\text{Cu}(\text{d})$ character and only slight $\text{Cl}(\text{p})$ character. The HOMO-5 is interesting in terms of the stabilisation of the bispidine geometry, since it shows some bonding interaction between the $\text{Cl}(\text{p}_y)$ and the upper lobe of the pyridine π system. Since it only involves the upper lobe of the pyridine π system, it requires that the pyridine rings are situated slightly below the $\text{Cu}-\text{Cl}$ bond, which may explain the deviation from the planarity of the equatorial donors one would expect for a square-planar complex.

3. The Copper(II) Complexes of tetradentate 3,7-Diazabicyclo[3.3.1]nonane Derivatives

This can be tested by comparing the orbitals of $[\text{Cu}(\text{L}^{1a})(\text{Cl})]^+$ to the corresponding orbitals in the *trans* N3 and *trans* N7 isomers of $[\text{Cu}(\text{L}^{2a})(\text{Cl})]^+$. The HOMO of the *trans* N3 isomer of $[\text{Cu}(\text{L}^{2a})(\text{Cl})]^+$ is similar to that of $[\text{Cu}(\text{L}^{1a})(\text{Cl})]^+$, with the exception of some additional N7(p_z) character, in keeping with the observed trigonal-bipyramidal distortion (Figure 3.8(b)). The HOMO-1 and HOMO-2 also correspond to those of $[\text{Cu}(\text{L}^{1a})(\text{Cl})]^+$, while the HOMO-3 and HOMO-4 are exchanged relative to $[\text{Cu}(\text{L}^{1a})(\text{Cl})]^+$, but the orbital character remains the same. In terms of the pyridine π system, the HOMO-5 of $[\text{Cu}(\text{L}^{2a})(\text{Cl})]^+$ is identical to that of $[\text{Cu}(\text{L}^{1a})(\text{Cl})]^+$, but the Cl(p_y) component is missing, which supports the interpretation that it is this interaction between the π orbitals of the pyridine rings and the p_y orbitals of the co-ligand which stabilises this geometry.

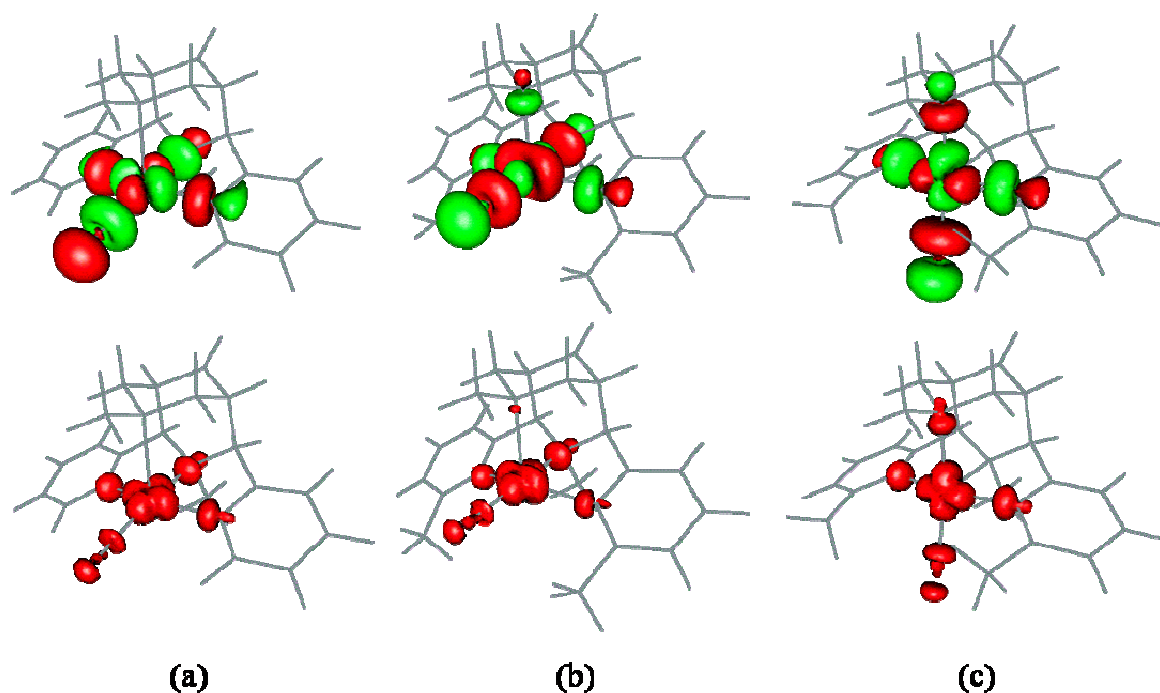


Figure 3.8. The HOMO from ROB3LYP calculations and spin density from UB3LYP calculations for (a) $[\text{Cu}(\text{L}^{1a})(\text{Cl})]^+$ and $[\text{Cu}(\text{L}^{2a})(\text{Cl})]^+$, (b) *trans* N3 and (c) *trans* N7

In the *trans* N7 isomer of $[\text{Cu}(\text{L}^{2a})(\text{Cl})]^+$, the coordinate system is perpendicular to that of $[\text{Cu}(\text{L}^{1a})(\text{Cl})]^+$, with the Cu–N3 bond along the z-axis, and the other two axes unchanged. The HOMO is again the σ antibonding combination of a Cu($d_{x^2-y^2}$) and the p orbitals of the donor atoms in the xy-plane (Figure 3.8(c)). Unlike the *trans* N3 isomer but like $[\text{Cu}(\text{L}^{1a})(\text{Cl})]^+$,

there is no component in the z-direction. The HOMO-1 to HOMO-4 correspond to those of the *trans* N3 isomer. The HOMO-5 has the same pyridine(π) character as the corresponding orbitals of the other two species, as well as some Cl(p) character, but there is no overlap between these two components because they are approximately perpendicular to each other. Another orbital which has significant pyridine(π) and Cl(p) character and which may play a role in determining the orientation of the pyridine rings, is the HOMO-9. The main interaction here however, is between the pyridine(π) system and the N7(p_z) orbital. The HOMO-5 and HOMO-9 of $[\text{Cu}(\text{L}^{1a})(\text{Cl})]^+$ and the two isomers of $[\text{Cu}(\text{L}^{2a})(\text{Cl})]^+$ are shown in Figure 3.9.

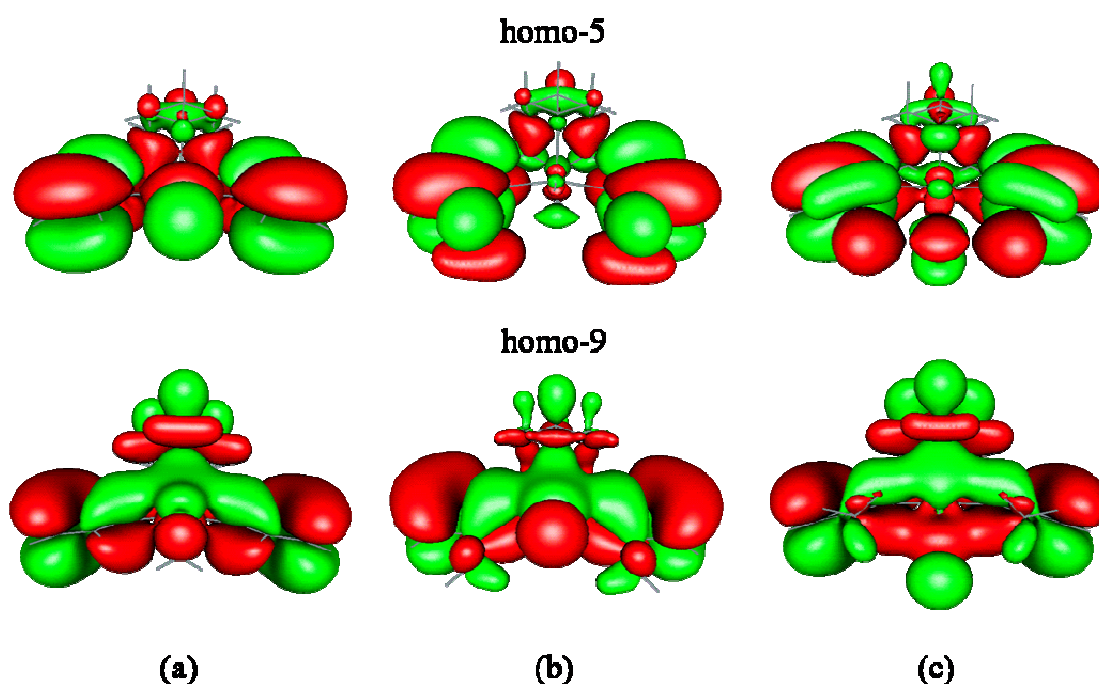


Figure 3.9. Orbital interactions between the CuCl^+ unit and the pyridine donors of the bispidine, for (a) $[\text{Cu}(\text{L}^{1a})(\text{Cl})]^+$ and $[\text{Cu}(\text{L}^{2a})(\text{Cl})]^+$, (b) *trans* N3 and (c) *trans* N7^[21]

Since a d^9 copper(II) system has only one unpaired electron, the total molecular spin density determined from the unrestricted DFT calculations indicates the position of this single electron. Indeed, the molecular spin density distribution from the unrestricted calculations has the same shape as the HOMO of the RO calculations, as shown in Figure 3.8. Both the RO and the unrestricted DFT calculations therefore predict the correct electronic structures for the copper(II) bispidine complexes, despite the fact that Jahn-Teller distortion is underestimated in the *trans* N7 isomer.

3.3.3. Calibration of the DFT Functional

The influence of the functional on the spin density distribution in $[\text{Cu}(\text{L}^1)(\text{Cl})]^+$ and $[\text{Cu}(\text{L}^2)(\text{Cl})]^+$

A known weakness of pure DFT functionals such as BLYP, BP86 and BPW91, is that they generate an overly covalent bonding description due to a lack of electron correlation^[22]. For this reason hybrid DFT functionals such as B3LYP, B3P86 and B3PW91 were developed in which a certain amount of Hartree-Fock exchange (E_{XHF} , 20%) was incorporated into the functional to account for the lack of electron correlation. While these hybrid functionals have proven to be reliable for a wide range of compounds, it has been shown that the bonding description in $[\text{Cu}(\text{Cl})_4]^{2-}$ is still too covalent^[10]. On the other hand, Becke's half and half functional (BHandHLYP), which incorporates 50% E_{XHF} , gives a description which is too ionic. This was determined by comparing the calculated spin density distribution in $[\text{Cu}(\text{Cl})_4]^{2-}$ with various functionals to the spin density distribution determined from EPR spectroscopy. A functional containing 38% E_{XHF} was found to give the best correlation with the experimental spin densities in $[\text{Cu}(\text{Cl})_4]^{2-}$.

The EPR spectrum of $[\text{Cu}(\text{L}^{\text{b}})(\text{Cl})]^+$ is well resolved and the super hyperfine transitions due to the donor atoms are observed in the perpendicular region^[23]. Using a model based on ligand field theory, the spin densities of the copper centre and the donor atoms can be determined from the hyperfine and super hyperfine values, respectively. The best spectral simulation was based on a model where coupling of the electron spin with the nuclear spins of Cu ($I=3/2$), N3, Npy1, Npy2 ($I=1$) and Cl ($I=3/2$) was considered and coupling with N7 was assumed to have a negligible contribution to the super hyperfine splitting pattern. This yielded spin densities of 0.868 for Cu and values of 0.044, 0.046 and 0.082 for N3, the Npy's and Cl respectively, which can be used to empirically calibrate the functional.

In analogy to the calculations performed for $[\text{Cu}(\text{Cl})_4]^{2-}$ ^[10], a range of DFT calculations with varying amounts of E_{XHF} were performed for $[\text{Cu}(\text{L}^{\text{a}})(\text{Cl})]^+$, $[\text{Cu}(\text{L}^{\text{b}})(\text{Cl})]^+$ and $[\text{Cu}(\text{L}^{\text{2a}})(\text{Cl})]^+$, using the 6-31G(d) basis set and a range of functionals implemented in Gaussian03. For L^{a} and L^{b} five pure DFT functionals (0% E_{XHF}), three B3-type functionals

3. The Copper(II) Complexes of tetradentate 3,7-Diazabicyclo[3.3.1]nonane Derivatives

(Becke's 3-parameter hybrid exchange functional with different correlation functionals, 20% E_XHF), the PBE (25% E_XHF) and BHandHLYP functionals (50% E_XHF) were used. For L^{2a} a subset of five of the above functionals was tested, as it was shown for L^{1a} and L^{1b} that the spin density is relatively unaffected by different correlation functionals. For comparative purposes, spin densities at the *ab initio* HF level were also calculated for both complexes. Results for selected functionals are summarised in Table 3.4 for $[Cu(L^{1a})(Cl)]^+$ and $[Cu(L^{1b})(Cl)]^+$ and Table 3.5 for $[Cu(L^{2a})(Cl)]^+$.

The calculations indicate that the main delocalisation of the single unpaired electron in $[Cu(L^{1a})(Cl)]^+$ and $[Cu(L^{1b})(Cl)]^+$ is to the Cl and the tertiary amine donor N3; slightly less spin density is donated to the two pyridine donors and the spin density on N7 is negligible. This is in agreement with the model used to calculate the hyperfine and super hyperfine splitting in the EPR spectrum. An interesting result is that hydrolysis of the C=O group at C9 has a negligible effect on the spin density of the copper centre. The spin densities calculated for $[Cu(L^{1b})(Cl)]^+$ are almost identical to those of $[Cu(L^{1a})(Cl)]^+$, although there is a slight decrease in the amount of donation to N3 and Cl and an even smaller increase in the donation to the Npy's.

A linear dependence of the spin density on the copper centre with the amount of HF exchange in the hybrid functional is observed, which seems to be relatively independent of the nature of the correlation functional. This is shown graphically for $[Cu(L^{1a})(Cl)]^+$ in Figure 3.10. For $[Cu(L^{1a})(Cl)]^+$ the spin on Cu varies between ~ 0.57 for the pure DFT functionals (0% E_XHF); ~ 0.67 for the Becke three-parameter hybrid functionals (20% E_XHF), 0.70 for the PBE/PBE (25% E_XHF) and 0.81 for the BHandHLYP (50% E_XHF) functionals respectively. The spin density on Cu calculated at HF level is 0.93. The spin on the donor atoms decreases as the spin on the copper increases and this relationship is also linear, as is shown in Figure 3.11.

The calculated spin densities are also relatively insensitive to small changes in the geometry of the coordination centre. If one compares, for example, the BVWN and BLYP functionals, both of which are pure DFT functionals, one notes that, although the copper–donor bond lengths differ by up to 0.1 Å, the calculated spin densities on the Cu are practically identical and those on the ligands very close.

Table 3.4. The influence of the functional on the spin density distribution in $[\text{Cu}(\text{L}^{1a})(\text{Cl})]^+$ and $[\text{Cu}(\text{L}^{1b})(\text{Cl})]^+$

Functional Parameters	BLYP	BP86	B3LYP	B3P86	PBE	B(38HF) LYP	B(38HF) P86	BH&HLYP	B(61HF) LYP	B(61HF) P86	exp
$[\text{Cu}(\text{L}^{1a})(\text{Cl})]^+$											
Cu	0.575	0.569	0.672	0.665	0.700	0.771	0.758	0.812	0.864	0.840	-
N7	0.001	0.002	0.000	0.000	0.000	-0.001	-0.001	0.001	-0.001	-0.001	-
N3	0.104	0.107	0.082	0.084	0.076	0.059	0.063	0.050	0.037	0.044	-
Npy	0.072	0.072	0.063	0.064	0.060	0.049	0.052	0.044	0.035	0.040	-
Cl	0.154	0.152	0.114	0.115	0.101	0.077	0.080	0.061	0.044	0.051	-
$[\text{Cu}(\text{L}^{1b})(\text{Cl})]^+$											
Cu	0.575	0.569	0.673	0.665	0.701	0.772	0.758	0.813	0.865	0.840	0.868
N7	0.002	0.003	0.000	0.000	0.000	-0.001	-0.001	0.001	-0.001	-0.001	0.000
N3	0.110	0.114	0.085	0.088	0.080	0.061	0.066	0.052	0.038	0.045	0.044
Npy	0.071	0.071	0.063	0.064	0.060	0.049	0.052	0.044	0.035	0.040	0.046
Cl	0.150	0.149	0.111	0.112	0.099	0.075	0.078	0.060	0.042	0.050	0.082

Table 3.5. The influence of the functional on the spin density distribution in $[\text{Cu}(\text{L}^{2a})(\text{Cl})]^+$

Functional Parameters	BP86	B3P86	B3LYP	PBE	B(38HF) P86	BH&HLYP	B(61HF) P86	HF
Cu	0.566, 0.563	0.671, 0.660	0.679, 0.669	0.709, 0.698	0.771, 0.759	0.828, 0.820	0.855, 0.846	0.945, 0.941
N7	0.034, 0.073	0.021, 0.057	0.020, 0.054	0.018, 0.051	0.014, 0.042	0.010, 0.030	0.009, 0.028	0.004, 0.008
N3	0.107, 0.004	0.087, 0.003	0.083, 0.004	0.079, 0.003	0.065, 0.003	0.050, 0.004	0.044, 0.003	0.021, 0.005
Npy	0.058, 0.078	0.050, 0.068	0.051, 0.066	0.046, 0.063	0.038, 0.053	0.032, 0.043	0.028, 0.038	-0.006, -0.005
Cl	0.137, 0.163	0.104, 0.126	0.102, 0.125	0.090, 0.110	0.069, 0.086	0.051, 0.063	0.041, 0.053	0.012, 0.019

3. The Copper(II) Complexes of tetradentate 3,7-Diazabicyclo[3.3.1]nonane Derivatives

The B3PW91 and B3LYP functionals, both of which contain 20% E_XHF , also give identical spin densities on the Cu, despite the differences of up to 0.05 Å in the predicted bond lengths. On the grounds of these observations, the influence of the slightly different geometries calculated by the different functionals and used for the calculation of the spin densities can be considered negligible in comparison to the much larger effect of the amount of HF exchange.

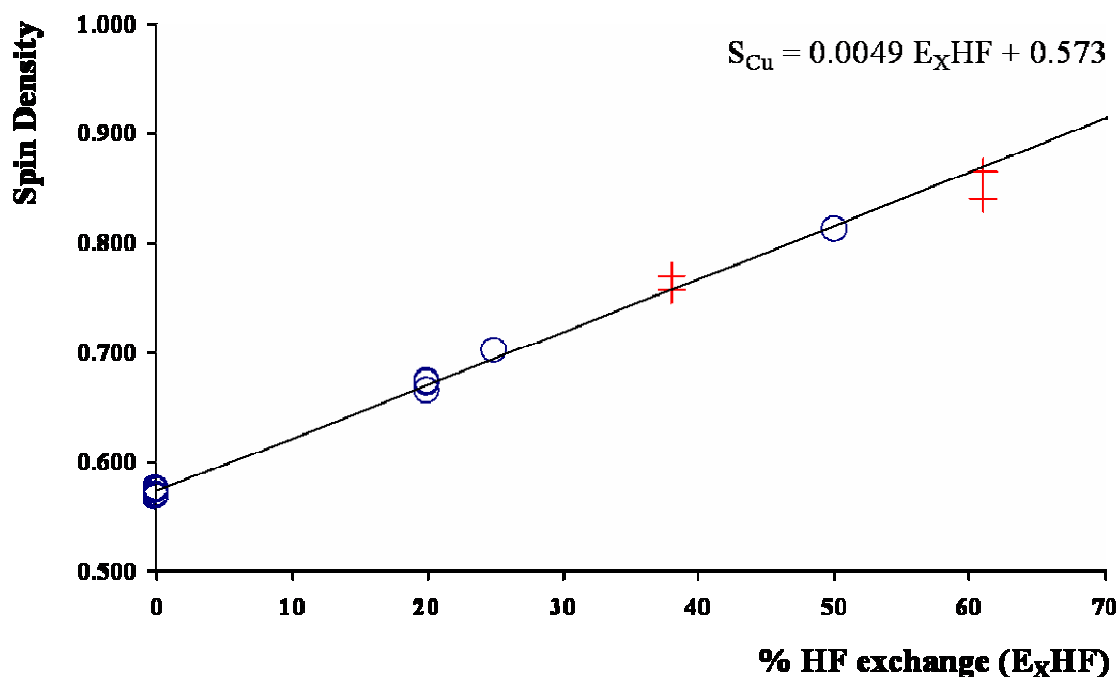
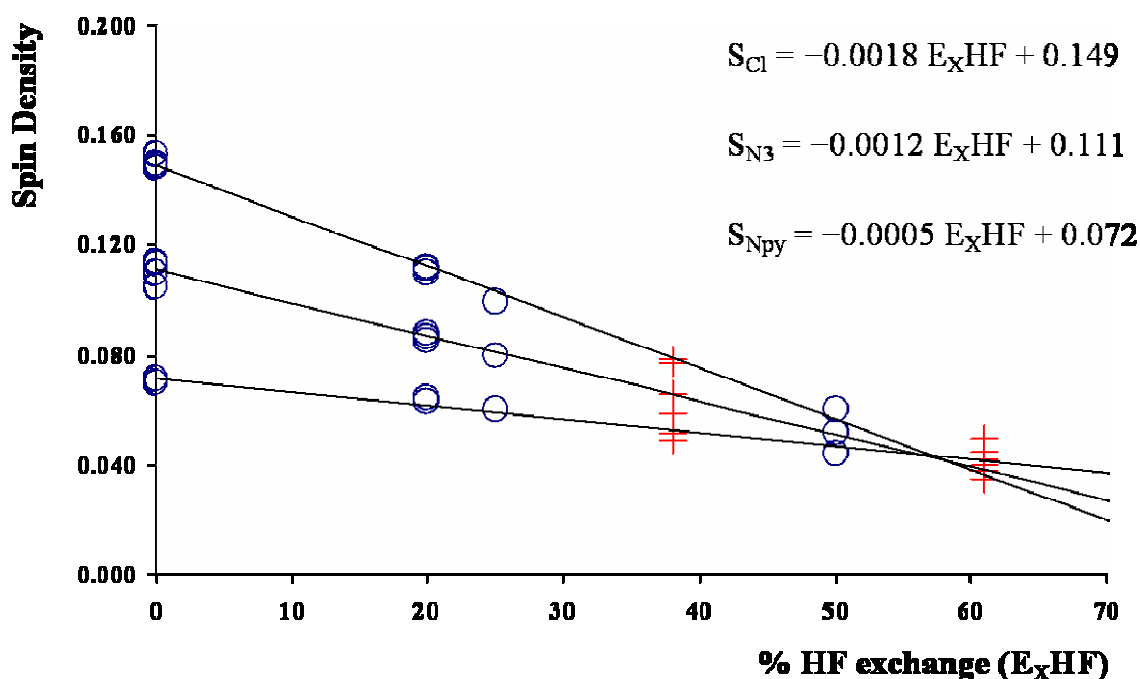


Figure 3.10. Plot of Spin Density vs E_XHF for the Cu in $[Cu(L^{1a})(Cl)]^+$, ○: Gaussian 03 implemented functionals (used for linear fitting), +: modified functionals

From the linear dependence of the spin density on the amount of E_XHF and the known experimental value of 0.87 for the spin on the copper centre in $[Cu(L^{1b})(Cl)]^+$, the amount of E_XHF required to predict the correct spin density on the copper is calculated to be 61%, considerably higher than the 38% found to be optimal for $[Cu(Cl)_4]^{2+}$. This is not unexpected, since the BHandHLYP functional, with 50% E_XHF , predicts a spin of 0.81 on the copper, which is still below the experimental value.

Calculations with an adjusted BLYP functional, incorporating 61% E_XHF (denoted B(61HF)LYP), were therefore performed and the result of 0.87 for the Cu spin density is in agreement with the “experimental” value. With an adjusted B(61HF)P86 functional, the calculated spin density is slightly lower (0.84), but still in good agreement with the

experimental value. For comparison, the B(38HF)LYP and B(38HF)P86 functionals yield Cu spin densities of 0.77 and 0.76 respectively, significantly lower than the experimental value.



**Figure 3.11. Plot of Spin Density vs E_XHF for, Cl, N3 and Npy in $[Cu(L^{1a})(Cl)]^+$,
○: Gaussian03 implemented functionals, +: modified functionals**

Not only the spin density on the copper, but also the spin densities on the donor atoms, can be determined by EPR spectroscopy (see Table 3.4), and here the first problem is encountered. While the B(61HF)LYP functional improves the calculated spin on the copper, a spin of around half of the experimental value for Cl and slightly lower than experiment for N3 and the Npy's are predicted.

The spin densities on the ligands also have a linear dependence on amount of E_XHF and from these equations the optimal amount of E_XHF necessary to reproduce the experimentally determined spin densities can be determined for each of the ligands, analogous to the method used for copper. For $[Cu(L^{1b})(Cl)]^+$, optimal values of 34%, 67% and 26% E_XHF are determined for Cl, N3 and Npy respectively. Yet another complication arises from the fact that, while the spin density on the copper is not dependent on the group at C9, the spin densities on the ligands are, to some extent. For $[Cu(L^{1a})(Cl)]^+$, the values are 35%, 61% and 27% for Cl, N3 and Npy respectively.

3. The Copper(II) Complexes of tetradentate 3,7-Diazabicyclo[3.3.1]nonane Derivatives

Interestingly, the required amount of HF exchange for Cl, based on the experimental value, is close to the 38% E_{XHF} determined to be optimal for $[\text{CuCl}_4]^{2-}$ [10]. Indeed, of all the tested functional, the B(38HF)LYP functional gives the best agreement with the experimental value for Cl (see Table 3.4). The spin on the Npy's should be best predicted by a functional such as PBE, with 25% E_{XHF} , as is indeed found to be the case, while N3 is best represented by the 61% E_{XHF} functional.

These inconsistencies reinforce the view that there is no general optimal functional for all complexes of a given metal. That being said however, it must be added that the contribution to the total spin density from the ligands is much smaller than the contribution of the metal centre. An improvement of the electronic description of the metal at the expense of some of the ligands should still give a better description of the electronic structure of the complex as a whole. Also, the contribution of N3 and Npy to the total spin density is small, so that large changes in E_{XHF} lead to smaller changes in spin density (and a corresponding smaller error) than for Cu or Cl. The main problem is therefore the incorrectly predicted spin density on Cl. For $[\text{Cu}(\text{L}^{2\text{a}})(\text{Cl})]^+$ the relationship between the amount of E_{XHF} and the spin density on the copper centre is also linear, for both the *trans* N3 and *trans* N7 isomers. The spin density distributions and the relationships to the amount of E_{XHF} are similar to that of $[\text{Cu}(\text{L}^{1\text{a}})(\text{Cl})]^+$. The spin densities predicted by the B(61HF)LYP functional correspond well with the experimentally determined spin densities for 6-31G(d) basis set. It has been shown for $[\text{CuCl}_4]^{2-}$ however, that an increase in size of the basis set tends to decrease the spin density on the copper centre for all-electron basis sets and increase the spin density for ECP basis sets [10]. This suggests that a larger all electron basis set would require a functional with more than 61% E_{XHF} and a larger ECP basis set one with less than 61% E_{XHF} . This further complicates the problem and makes it near to impossible to find a functional which is optimal for copper(II) complexes and all basis sets.

Table 3.6. The influence of the functional on the geometry of $[\text{Cu}(\text{L}^{\text{lb}})(\text{Cl})]^+$

Functional Parameter	BLYP	BP86	B3LYP	B3P86	PBE	B(38HF) LYP	B(38HF) P86	BH&H LYP	B(61HF) LYP	B(61HF) P86
	Cu-N7	2.338	2.262	2.334	2.274	2.277	2.358	2.262	2.305	2.370
Cu-N3	2.069	2.044	2.058	2.035	2.037	2.077	2.040	2.068	2.106	2.047
Cu-Npy	2.020	1.997	2.028	2.005	2.011	2.056	2.017	2.043	2.090	2.022
Cu-Cl	2.271	2.249	2.239	2.219	2.218	2.240	2.213	2.228	2.249	2.208
N7-Cu-N3	86.82	87.89	85.80	86.48	86.14	84.82	86.04	85.15	84.02	85.60
N7-Cu-Cl	106.59	106.10	107.87	107.49	107.91	109.27	108.46	109.35	110.77	109.35
Npy-Cu-Npy	154.30	153.30	155.49	155.21	155.35	155.44	155.31	155.19	154.36	155.10
Cu-N7/Cu-N3	1.130	1.106	1.134	1.117	1.118	1.135	1.109	1.115	1.125	1.094

Table 3.7. The influence of the functional on the relative energies and geometries of the two isomers of $[\text{Cu}(\text{L}^{2\text{th}})(\text{Cl})]^+$

Functional Parameter	BP86	B3P86	B3LYP	PBE	B(38HF)P86	BH&HLYP	B(61HF)P86	HF
	Cu-N7	2.344, 2.173	2.311, 2.157	2.374, 2.210	2.307, 2.164	2.282, 2.162	2.316, 2.219	2.251, 2.163
Cu-N3	2.013, 2.143	2.003, 2.141	2.023, 2.164	2.005, 2.140	2.006, 2.134	2.030, 2.147	2.011, 2.120	2.079, 2.150
Cu-Npy	2.080, 2.015	2.104, 2.028	2.132, 2.055	2.114, 2.036	2.129, 2.044	2.170, 2.079	2.143, 2.056	2.276, 2.171
Cu-Cl	2.231, 2.272	2.201, 2.237	2.220, 2.258	2.201, 2.234	2.195, 2.227	2.208, 2.240	2.191, 2.218	2.239, 2.263
N7-Cu-N3	87.29, 87.87	86.85, 87.12	86.20, 86.65	86.64, 86.75	86.61, 86.52	85.93, 85.61	86.22, 85.90	85.27, 83.58
N7-Cu-Cl	91.53, 162.94	93.49, 162.59	93.38, 162.20	93.96, 162.40	95.02, 161.45	95.99, 159.79	96.36, 16.13	99.35, 153.42
Npy-Cu-Npy	144.58, 166.72	144.76, 165.33	145.20, 165.09	144.66, 164.92	144.62, 164.44	144.67, 163.56	144.54, 163.46	143.54, 160.65
Cu-N7/Cu-N3	1.164, 1.014	1.154, 1.007	1.174, 1.021	1.151, 1.011	1.138, 1.013	1.141, 1.034	2.229, 2.020	1.117, 1.085
ΔE (kJ/mol)	7.12	6.17	9.15	5.59	6.50	9.87	6.59	12.45

The influence of the functional on the geometries and relative energies of $[\text{Cu}(\text{L}^1)(\text{Cl})]^+$ and $[\text{Cu}(\text{L}^2)(\text{Cl})]^+$

Selected geometric parameters of $[\text{Cu}(\text{L}^{2b})(\text{Cl})]^+$ calculated with the functionals described above are given in Table 3.6. On the whole the hybrid functionals perform better for angles, but overestimate the bond lengths, and this overestimation increases as more E_{XHF} is added. The non-hybrid functionals generally give a better description of the bond lengths but worsen the bond angles. So, while the spin densities are improved by increasing the amount of E_{XHF} , this is done so at the expense of the geometries.

The geometries and relative energies of the two isomers of $[\text{Cu}(\text{L}^{2a})(\text{Cl})]^+$ were also compared for the range of functionals described above, in an attempt to find an explanation for the computed destabilisation of the experimentally observed *trans* N7 isomer, relative to the *trans* N3 isomer. The results are summarised in Table 3.7. While the energy difference between the two isomers is decreased by two of the functionals, PBE and B3P86, relative to the B3LYP value, none of the functionals predict the *trans* N7 isomer to be more stable.

Since a 10 kJ/mol difference in energy between isomers leads to an experimental ratio of 99:1 and only the *trans* N7 isomer of $[\text{Cu}(\text{L}^{2b})(\text{Cl})]^+$ is observed, this implies that this isomer should be at least 10 kJ/mol lower in energy than the *trans* N3 isomer. However, the calculated energy difference is up to 10 kJ/mol in the opposite direction, implying that the density functional methods make an error of more than 20 kJ/mol in the calculation of the relative energies of the isomers (see also to Section 3.3.1).

While the calculated geometries of the *trans* N7 isomer of $[\text{Cu}(\text{L}^2)(\text{Cl})]^+$ show an overall good agreement with experiment across the range of functionals, the Cu–N3 bonds are consistently shorter than the Cu–N7 bonds in the calculated structures ($\text{Cu–N7}/\text{Cu–N3} > 1$). This is in contrast to the crystal structure, where the Cu–N3 bond is slightly longer than the Cu–N7 bond ($\text{Cu–N7}/\text{Cu–N3} = 0.99$). It is interesting to note that the two functionals which give the smallest error in relative energy (PBE and B3P86) also have the smallest Cu–N7/Cu–N3 ratio (1.01) and therefore also better agreement with experiment. For B3LYP and BHandHLYP the ratios are larger (1.02 and 1.03, respectively) and the relative energies increase to 9.2 and 9.9 kJ/mol, respectively. The *ab initio* calculations at HF level give a Cu–N7/Cu–N3 ratio of

3. The Copper(II) Complexes of tetradentate 3,7-Diazabicyclo[3.3.1]nonane Derivatives

1.08 and an energy difference of 12.5, performing worse than any of the DFT functionals. The incorrect prediction of the Cu–N7/Cu–N3 ratio may lead to a loss of electronic stabilisation (due to the pseudo Jahn-Teller effect) in the calculated *trans* N7 structures and may be the reason for the computed destabilisation of the *trans* N7 isomer of $[\text{Cu}(\text{L}^2)(\text{Cl})]^+$.

It should be noted that the optimal functional for $[\text{Cu}(\text{L}^1)(\text{Cl})]^+$ from the point of view of the spin density on the copper centre is not the functional which gives the smallest error in relative energy for $[\text{Cu}(\text{L}^2)(\text{Cl})]^+$. In fact, there is no direct correlation between the covalence of the bonding (% E_{XHF}), the relative energy of the two isomers and the Cu–N7/Cu–N3 ratio. The overall tendency is that an increase in the % E_{XHF} improves the description of the spin densities, but worsens the Cu–N7/Cu–N3 ratio and the therefore also the relative energy between the *trans* N3 and *trans* N7 isomers. The question of the correct functional for the calculation of copper-bispidine complexes is therefore not as simple as for $[\text{Cu}(\text{Cl})_4]^{2-}$, where the bond covalence is the only significant factor determining the bond lengths and energies.

This problem can be partially remedied by the choice of correlation functional. While the correlation functional does not significantly influence the spin density distribution, it does influence the bond lengths and therefore also the relative energies. The P86 correlation functional predicts shorter bond lengths than LYP, in better agreement with experiment. A change from B3LYP to B3P86 reduces both the Cu–N7 and Cu–N3 bond lengths, but has a larger effect on Cu–N7 than on Cu–N3. Consequently, ΔE between the isomers is reduced by 3kJ/mol. Furthermore, the change in ΔE between B3P86 and B(61HF)P86 (a threefold increase in % HF exchange) is negligible, unlike for the LYP correlation functional, which is much more sensitive to the amount of E_{XHF} .

A further possibility is that the *trans* N3 isomer is indeed more stable in the gas phase and that the *trans* N7 isomer is found in crystalline form because it is stabilised by solvent effects or by the crystal lattice. This possibility was tested by solution phase geometry optimisations of the two isomers of $[\text{Cu}(\text{L}^{2a})(\text{Cl})]$, using the 6-31G(d) basis set and the PCM with acetonitrile as the solvent. Indeed, this has the effect of decreasing ΔE to 4 kJ/mol (from 9 kJ/mol in the gas phase) for the B3LYP functional, although the *trans* N3 isomer remains more stable. For the B3P86 functional, which already shows an improvement over B3LYP in the gas phase,

3. The Copper(II) Complexes of tetradentate 3,7-Diazabicyclo[3.3.1]nonane Derivatives

solvent effects lead to near degeneracy of the isomers (ΔE less than 1 kJ/mol). One expects therefore that the addition of solvent effects to the B(61HF)LYP functional will also give close to degenerate isomers.

The B3LYP/6-31G(d) optimised *trans* N3 and *trans* N7 geometries of $[\text{Cu}(\text{L}^{2a})(\text{Cl})]^+$ have also been used to calculate the energy with the SORCI method^[24]. For these calculations, the Ahlrichs triple- ζ basis set for the metal center and a double- ζ basis set for the non-metal atoms have been employed. Without solvation, the SORCI calculation predicts the *trans* N3 isomer to be more stable than the *trans* N7 isomer by 13.6 kJ/mol (consistent with the Gaussian03 and ADF predictions). However, using the COSMO solvation model implemented in ORCA and acetonitrile as the solvent, the reverse order is obtained, i.e. the *trans* N7 isomer is more stable by 7.9 kJ/mol. This seems to suggest that, while the incorrect prediction of the Cu-N7/Cu-N3 ratio does play a role in determining the energy difference between the two isomers, the *trans* N3 isomer may, in fact, be the most stable isomer in the gas phase, while the *trans* N7 isomer is stabilised in solution and is therefore also the only isomer observed in the crystalline form.

3.4. Conclusion

We have shown that substrate binding in the copper(II) complexes of the ligand L^1 takes place preferentially *trans* to the tertiary amine donor N3, regardless of the nature and denticity of the substrate, leading to square-pyramidal or distorted octahedral geometries with an elongated Cu–N7 bond. This is in agreement with experiment and the results of an earlier DFT study. Substitution *ortho* to the coordinating nitrogen of the pyridine rings leads to a distortion of the favoured square-pyramidal geometry and the appearance of further minima on the potential energy surface, with elongated Cu–N3 or Cu–Npy axes. The relative energies of these isomers are determined by the size of the *ortho* substituent and through variation of the co-ligand in complexes with *ortho* substituted bispidines, all three “Jahn-Teller isomers” can be obtained.

The reasons for the preferential binding of substrates *trans* to N3 and the specific orientation of the Cu–X unit (slightly above the plane of the two pyridine rings) have been explored. The calculations indicate some bonding interaction between the π bonding orbitals of the pyridine rings and the p orbitals of the co-ligand, which may play a role in determining the orientation of the Cu–X unit relative to the pyridine rings.

The overall correlation of the experimental and calculated geometries is good, but for the $[\text{Cu}(\text{L})(\text{Cl})]^+$ complexes, the Cu–N7/Cu–N3 ratio in the *trans* N7 isomers is incorrectly predicted by DFT (with Gaussian03 and ADF) and HF calculations. Both the DFT and HF calculations also predict the incorrect energetic order of the *trans* N3 and *trans* N7 isomers of $[\text{Cu}(\text{L})(\text{Cl})]^+$. The energy difference between the two isomers decreases as the ratio of Cu–N7/Cu–N3 decreases, but the relationship is not linear.

A range of functionals was therefore tested and the spin density on the copper centre and the donor atoms shown to be directly proportional to the amount of HF exchange incorporated into the hybrid DFT functionals. By varying the % $E_{\text{X}}\text{HF}$, the functional can be tuned to predict the correct spin density on the copper centre in $[\text{Cu}(\text{L}^{\text{b}})(\text{Cl})]^+$, but the spin densities on the ligands, in particular Cl, are not correctly predicted with the tuned functional. In addition, the optimal functional in terms of spin density on the copper and donor atoms does

3. The Copper(II) Complexes of tetradentate 3,7-Diazabicyclo[3.3.1]nonane Derivatives

not solve the problem of the incorrect prediction of the Cu–N7/Cu–N3 ratios in the *trans* N7 structures or the resulting incorrect prediction of the energies.

The correlation functional has a larger effect on the relative energies than the exchange functional, with the P86 correlation functional performing better LYP. The addition of solvent effects in the calculations also stabilises the *trans* N7 isomer with respect to the *trans* N3 isomer, leading to better agreement with experiment. This suggests that the *trans* N3 isomer may be the most stable isomer in the gas phase, while the *trans* N7 isomer is stabilised in solution and is therefore also the only isomer observed in the crystalline form.

3.5. References

-
- ¹ H. Börzel, P. Comba, C. Katsichtis, W. Kiefer, A. Lienke, V. Nagel and H. Pritzkow, *Chem. Eur. J.*, **1999**, 5, 1716
- ² H. Börzel, P. Comba, K.S. Hagen, C. Katsichtis and H. Pritzkow, *Chem. Eur. J.*, **2000**, 6, 914
- ³ H. Börzel, P. Comba and H. Pritzkow, *Chem. Commun.*, **2001**, 97
- ⁴ P. Comba, B. Martin, A. Prikhod'ko, H. Pritzkow and Heidi Rohwer, *C.R. Chimie*, **2005**, 8, 1506
- ⁵ R. Gleiter, M. Kobayashi and J. Kuthan, *Tetrahedron*, **1976**, 32, 2775
- ⁶ P. Comba, A. Lienke, *Inorg. Chem.*, **2001**, 40, 5206
- ⁷ *Gaussian 03, Revision B.03*, M. J. Frisch, G. W. Trucks, H. B. Schlegel, G. E. Scuseria, M. A. Robb, J. R. Cheeseman, J. A. Montgomery, Jr., T. Vreven, K. N. Kudin, J. C. Burant, J. M. Millam, S. S. Iyengar, J. Tomasi, V. Barone, B. Mennucci, M. Cossi, G. Scalmani, N. Rega, G. A. Petersson, H. Nakatsuji, M. Hada, M. Ehara, K. Toyota, R. Fukuda, J. Hasegawa, M. Ishida, T. Nakajima, Y. Honda, O. Kitao, H. Nakai, M. Klene, X. Li, J. E. Knox, H. P. Hratchian, J. B. Cross, C. Adamo, J. Jaramillo, R. Gomperts, R. E. Stratmann, O. Yazyev, A. J. Austin, R. Cammi, C. Pomelli, J. W. Ochterski, P. Y. Ayala, K. Morokuma, G. A. Voth, P. Salvador, J. J. Dannenberg, V. G. Zakrzewski, S. Dapprich, A. D. Daniels, M. C. Strain, O. Farkas, D. K. Malick, A. D. Rabuck, K. Raghavachari, J. B. Foresman, J. V. Ortiz, Q. Cui, A. G. Baboul, S. Clifford, J. Cioslowski, B. B. Stefanov, G. Liu, A. Liashenko, P. Piskorz, I. Komaromi, R. L. Martin, D. J. Fox, T. Keith, M. A. Al-Laham, C. Y. Peng, A. Nanayakkara, M. Challacombe, P. M. W. Gill, B. Johnson, W. Chen, M. W. Wong, C. Gonzalez, and J. A. Pople, *Gaussian, Inc., Pittsburgh PA*, **2003**
- ⁸ C. Lee, W. Yang, R. Parr, *Phys. Rev. B*, **1988**, 37, 785; A.D. Becke, *J. Chem. Phys.*, **1993**, 98, 5648
- ⁹ R.K. Szilagy, M. Metz and E.I. Solomon, *J. Phys. Chem. A*, **2002**, 106, 2994
- ¹⁰ R.S. Mulliken, *J. Chem. Phys.*, **1955**, 23, 1833
- ¹¹ G. te Velde, F.M. Bickelhaupt, S.J.A. van Gisbergen, C. Fonseca Guerra, E.J. Baerends, J.G. Snijders, T. Ziegler, *J. Comput. Chem.*, **2001**, 22, 931; C Fonseca Guerra, J G Snijders, G te Velde, and E J Baerends, *Theor. Chem. Acc.*, **1998**, 99, 391; *ADF version 2004.01e*, E.J. Baerends, J. Autschbach, A. Bérces, C. Bo, P.M. Boerrigter, L. Cavallo, D.P. Chong, L. Deng, R.M. Dickson, D.E. Ellis, L. Fan, T.H. Fischer, C. Fonseca Guerra, S.J.A. van Gisbergen, J.A. Groeneveld, O.V. Gritsenko, M. Grüning, F.E. Harris, P. van den Hoek, H. Jacobsen, G. van Kessel, F. Kootstra, E. van Lenthe, D.A. McCormack, V.P. Osinga, S.

Patchkovskii, P.H.T. Philipsen, D. Post, C.C. Pye, W. Ravenek, P. Ros, P.R.T. Schipper, G. Schreckenbach, J.G. Snijders, M. Sola, M. Swart, D. Swerhone, G. te Velde, P. Vernooijs, L. Versluis, O. Visser, E. van Wezenbeek, G. Wiesenekker, S.K. Wolff, T.K. Woo, and T. Ziegler, *SCM, Theoretical Chemistry, Vrije Universiteit, Amsterdam, The Netherlands*, <http://www.scm.com>

¹² T. Ziegler and A. Rauk, *Inorg. Chem.*, **1979**, 18, 1558; T. Ziegler and A. Rauk, *Inorg. Chem.*, **1979**, 18, 1755; F.M. Bickelhaupt and E.J. Baerends, in *Rev. Comput. Chem.*, K B Lipkowitz and D B Boyd, Eds., *Wiley, New York*, **2000**, 15, 1

¹³ *gOpenmol, Version 2.20 for Linux*, L. Laaksonen, **1997**

¹⁴ *GaussView, Version 3.09*, R. Dennington II, T. Keith, J. Millam, K. Eppinnett, W.L. Hovell, and R. Gilliland, Semichem, Inc., Shawnee Mission, KS, **2003**

¹⁵ S. Wunderlich, *Forschungsbericht im Rahmen des Anorganisch-Chemischen Fortgeschrittenenpraktikums*, Ruprecht-Karls Universität Heidelberg, **2005**

¹⁶ P.Comba, T.W. Hambley, G. Lauer, M. Melter, N. Okon, *MOME97, a Molecular Package for Inorganic Compounds*, CVS, **1997**

¹⁷ J.E. Bol, C. Buning, P. Comba, J. Reedijk, M. Ströhle, *J. Comp.Chem.*, **1998**, 19, 512

¹⁸ P.Comba, B. Martin, A. Prikhod'ko, H. Prtitzkow, H. Rohwer, *C.R. Chimie*, **2005**, 8, 1506

¹⁹ Calculations performed by Dr. Bodo Martin, **2005**

²⁰ C. Lopez de Laorden, *PhD Thesis*, Ruprecht-Karls Universität Heidelberg, **2006**

²¹ Molecular orbitals plotted at a contour level of 0.009

²² W. Koch und M.C. Holthausen, *A Chemist's Guide to Density Functional Theory, 2nd Ed.*, Wiley VCH, Weinheim, **2001**

²³ M. Atanasov, P. Comba, B. Martin, V. Müller, G. Rajaraman, H. Rohwer, *J. Comput. Chem.*, **2006**, *accepted*

²⁴ Calculations performed by Dr. Gopalan Rajaraman

4. A Mechanistic Study of the Reaction with H₂O₂ of the Iron(II) Complex of a tetradentate 3,7-Diazabicyclo[3.3.1]nonane Derivative

4.1. Introduction

Mononuclear non-heme iron enzymes are known to catalyse a variety of hydrocarbon oxidations via the activation of molecular oxygen^[1,2,3], and much research has been devoted to clarifying the mechanisms of these oxidations. While the exact mechanistic details remain unclear, many are believed to proceed via Fe^{III}-alkylperoxo or -hydroperoxo intermediates. However, for non-heme iron enzymes, few reactive intermediates have been characterised. Key intermediates that have been identified include a high-spin Fe^{III}-alkylperoxo unit in lipoxygenase^[2,3,4], a low-spin Fe^{III}-hydroperoxo intermediate in bleomycin^[5,6] and a high-spin Fe^{IV}=O species in TauD (an α -ketoglutarate dioxygenase enzyme)^[7].

Probably the most well studied example of a mononuclear non-heme iron enzyme is that of the anti-tumor drug bleomycin (BLM). Bleomycin is responsible for DNA cleavage in cells and is believed to coordinate Fe^{II} pentadentately, leaving an open site for the coordination of molecular oxygen. Figure 4.1 shows the bleomycin ligand, with the donor atoms highlighted in red.

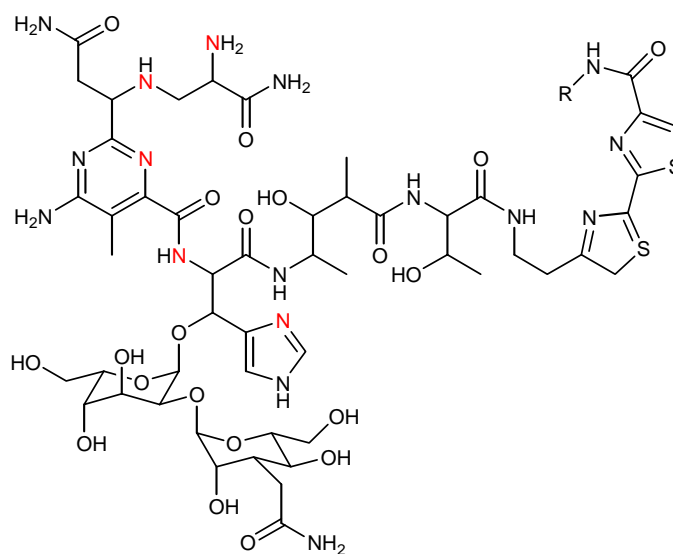


Figure 4.1. The active site of bleomycin (with donor atoms highlighted in red)^[3]

4. The Reaction of the Iron(II) Complex of a tetradentate 3,7-Diazabicyclo[3.3.1]nonane Derivative with H₂O₂

The addition of O₂ leads to the formation of an Fe^{III}(BLM)(•O₂⁻) intermediate, referred to as oxygenated BLM, which is consumed by disproportionation, to form Fe^{III} + O₂ and an Fe^{III}(BLM)(OOH) intermediate known as activated bleomycin (ABLM). ABLM is the last spectroscopically observable intermediate in the reaction cycle before DNA cleavage takes place. While heterolytic cleavage of the O–O bond of the Fe^{III}-hydroperoxo intermediate has been shown by DFT calculations to be highly favourable for porphyrin systems^[8,9,10], due to the formation of an Fe^{IV}=O/porphyrin radical combination, the corresponding O–O bond heterolysis in BLM is calculated to be highly endothermic and therefore highly unlikely to play a role in BLM chemistry. Homolytic cleavage is also ruled out on the basis of the high specificity of the reaction of ABLM with DNA^[6]. The current belief is that the hydroperoxo unit in ABLM is directly responsible for attack of the substrate C–H bond.

In addition to the enzymatic studies, the development of synthetic iron complexes aimed at mimicking the oxygenation reactions observed in non-heme iron oxygenases and aiding in the clarification of their mechanisms, is an active area of research^[11,12,13,14]. In particular, a number of ligands have been synthesised, whose iron(II) complexes have shown activity in the oxidation of alkanes and olefins in the presence of hydrogen peroxide^[15,16,17,18,19]. Some of the ligands used in oxidation catalysis are shown in Figure 4.2. They have in common a mixed amine/pyridine donor set and tetradentate or pentadentate coordination of Fe^{II}.

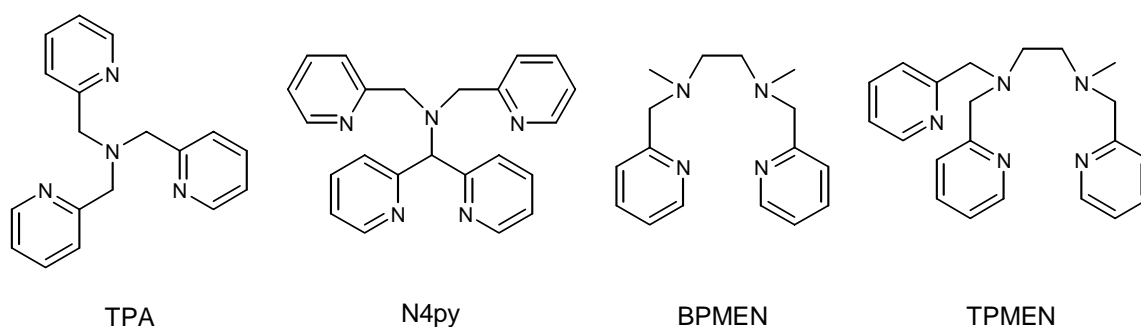


Figure 4.2. Common ligands used in iron oxidation catalysis

The similarity of the bispidine donor set to those of known ligands used in oxidation catalysis is apparent. The iron(II) complexes of selected bispidine ligands have been tested in the catalytic epoxidation and dihydroxylation of olefins with H₂O₂ and have proven to be among

the most active known, comparable in activity to those of TPA and N4py^[20]. Specifically, catalytic studies have been performed with the ligands L¹, L⁶ and L⁷, shown in Figure 4.3 along with a representation of the geometries of their Fe^{II} complexes.

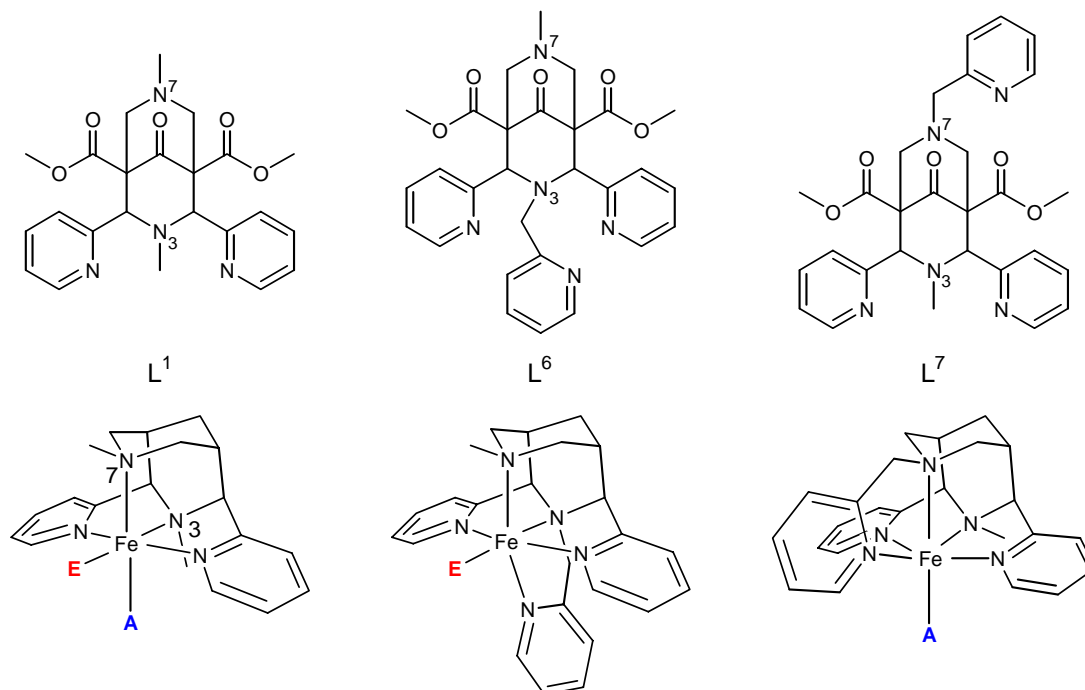


Figure 4.3. The bispidine ligands tested in iron oxidation catalysis and a representation of the geometries of their Fe^{II} complexes

The Fe^{II} complexes of L¹, L⁶ and L⁷ have distorted *cis*-octahedral geometries, with one or two open coordination sites which differ in their ability to bind substrates. Coordination in the equatorial plane *trans* to N3 (E in Figure 4.3) leads to short and strong bonds, while axial coordination *trans* to N7 (A in Figure 4.3) leads to longer and weaker bonds^[21]. While in complexes with L¹, both coordination sites are available, in complexes with L⁶ and L⁷ one of these coordination sites (*trans* to N3 and N7 respectively) is blocked, leading to dramatic differences in reactivity. Nonetheless, on the basis of product distributions, labelling studies and spectroscopically characterised intermediates, a similar chemistry is assumed for L⁶ and L⁷. Specifically, low-spin Fe^{III}- η^1 -hydroperoxo, high-spin Fe^{III}- η^2 -peroxo and low-spin (S=1) Fe^{IV}=O intermediates have been characterised for both ligands^[22,23,24] from the reaction of their Fe^{II} complexes with H₂O₂ under various conditions.

4. The Reaction of the Iron(II) Complex of a tetradentate 3,7-Diazabicyclo[3.3.1]nonane Derivative with H₂O₂

Reactivity and labelling experiments with L⁷ reveal that epoxide is formed exclusively under aerobic conditions and that a large percentage of this epoxide is formed using oxygen atoms originating from O₂, rather than H₂O₂ [20]. Under anaerobic conditions, the catalytic activity is greatly decreased and a mixture of epoxide and diol is formed. On the basis of these and the spectroscopic results, an oxidation mechanism based on the formation of an Fe^{III}-hydroperoxo intermediate, which undergoes homolytic cleavage of the O–O bond to form a low-spin Fe^{IV}=O intermediate, has been proposed [19].

The tetradentate ligand L¹, on the other hand, demonstrates a similar reactivity to L⁷, but a markedly different product distribution [25]. Diol is formed as the main product, with both oxygen atoms originating from H₂O₂, and the reactivity and product distribution under aerobic and anaerobic conditions are identical. This is in contrast to the pentadentate bispidines and the tetradentate TPA ligand, for example, where a percentage of oxygen in the diol is incorporated from H₂O in the reaction mixture [26]. In addition, no Fe^{III}-intermediates have been isolated from the reaction of the Fe^{II} complex of L¹ with H₂O₂, although Fe^{III}-peroxo and Fe^{III}-alkylperoxo [27] species have been formed from the reaction with KO₂ and ^tBuOOH respectively.

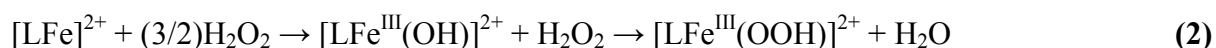
Due to the lack of characterised intermediates for L¹ and the possibility, suggested by spectroscopic, catalytic and labelling studies, of a different mechanism from the pentadentate ligands L⁶ and L⁷, a DFT study of possible mechanisms for the reaction of the Fe^{II} complex of L¹ with H₂O₂ was initiated. Inspiration was taken from mechanistic proposals [28,29] and experimental and computational studies [30,31] on the Fenton reaction (the reaction of Fe^{II} with H₂O₂ in aqueous medium), as well as from mechanistic studies of hydrocarbon oxidation by mononuclear non-heme enzymes and their model systems.

A commonly quoted mechanism for the Fenton reaction, is that of Haber and Weiss [29], which involves oxidation of the Fe^{II} centre to Fe^{III}. The reactive species are proposed to be free hydroxyl radicals produced by the resulting decomposition of hydrogen peroxide:



4. The Reaction of the Iron(II) Complex of a tetradentate 3,7-Diazabicyclo[3.3.1]nonane Derivative with H₂O₂

The classically proposed mechanism for oxidation by mononuclear non-heme iron enzymes also involves oxidation of the Fe^{II} centre to form of a low-spin [LFe^{III}(OOH)]²⁺ intermediate. A similar mechanism has been observed spectroscopically in synthetic model systems such as TPA and N4py, where the [LFe^{III}(OOH)]²⁺ complex is formed via an [LFe^{III}(OH)]²⁺ intermediate upon the reaction of H₂O₂ with the Fe^{II} precursor:



The [LFe(OOH)]²⁺ complex may then undergo homolytic or heterolytic cleavage of the O–O bond to form an Fe^{IV}=O species and an •OH radical or an Fe^V=O species and an [−]OH ion respectively; or it may react directly with the substrate, as is currently believed to be the case for bleomycin.

As far back as 1932 however, an alternative mechanism for the Fenton reaction was proposed, which involves the formation of a high-valent Fe^{IV}=O intermediate^[28]:

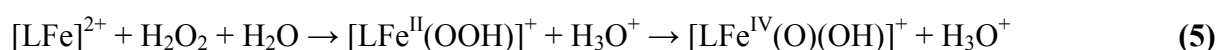


This mechanism has more recently been supported by experimental^[32] and DFT^[30] studies and involves ligand exchange of H₂O₂ with a coordinated H₂O molecule in the hexaaqua iron(II) complex to form [(H₂O)₅Fe^{II}(H₂O₂)]²⁺, two consecutive homolytic bond cleavage reactions to form [(H₂O)₄Fe^{IV}(OH)₂]²⁺ and proton transfer to form [(H₂O)₅Fe^{IV}(O)]²⁺.

An analogous mechanism may be proposed for the reaction of an Fe^{II} complex with H₂O₂:



The [LFe^{II}(H₂O₂)]²⁺ complex is expected to be slightly acidic and a third variation is therefore possible, which involves deprotonation of the complex prior to O–O bond cleavage:



Unlike reactions (2) and (4) however, this mechanism requires the presence of water to bring about deprotonation of the hydrogen peroxide.

Figure 4.4 shows the three main mechanistic pathways that have been investigated for L¹. Pathway **A** is based on reaction (2) above, pathway **B** on reaction (4) and pathway **C** on reaction (5). The results are compared with available experimental information and a mechanism for olefin oxidation is proposed, based on the accumulated experimental and computational results. Possible reasons for the differences in behaviour between L¹ and other tetradentate ligands such as TPA, as well as the pentadentate bispidine ligands L⁶ and L⁷, are also discussed.

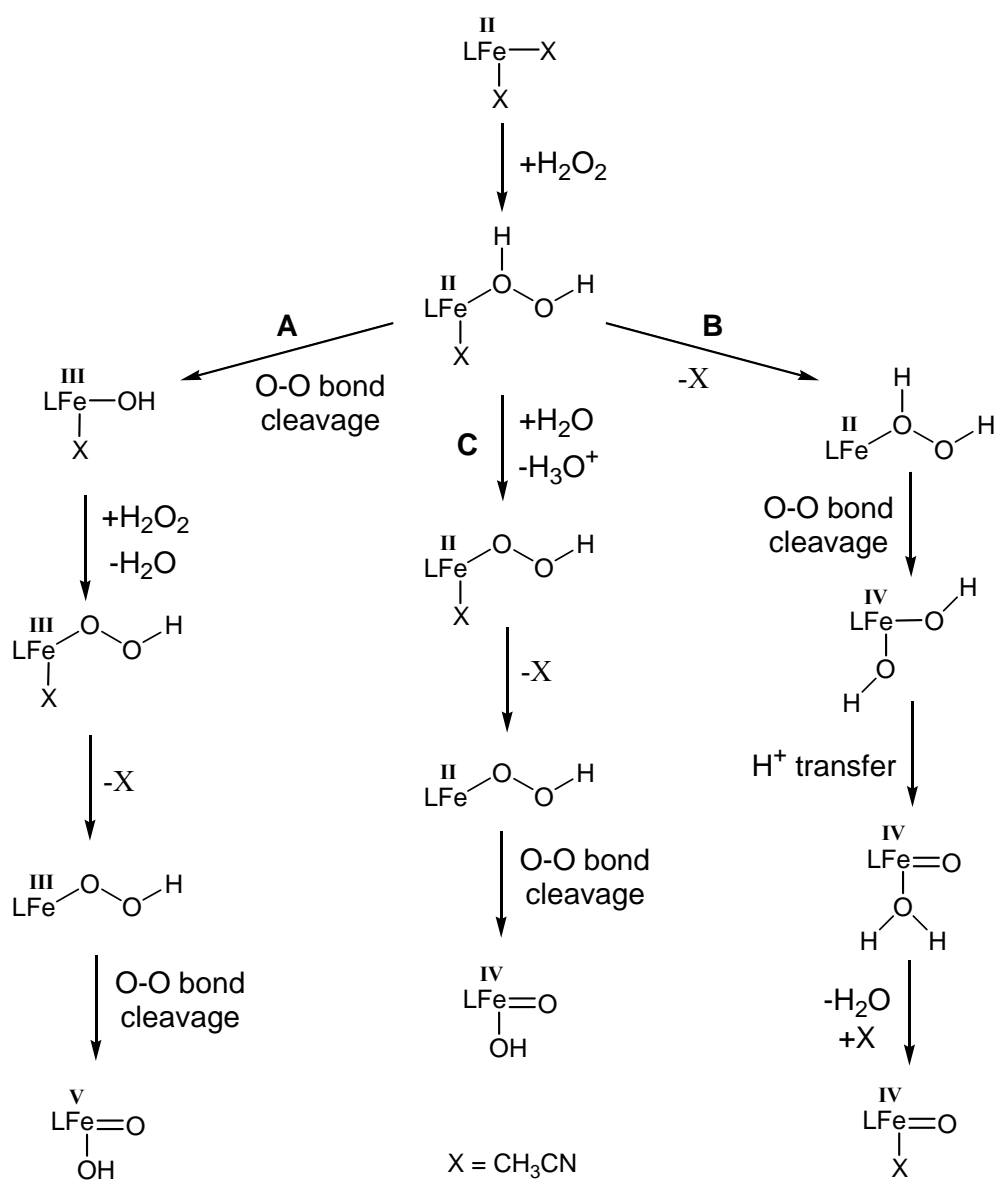


Figure 4.4. The main mechanistic pathways studied for the reaction of the iron(II) complex of the tetradentate bispidine ligand L¹ with H₂O₂

4.2. Computational Methods

Calculations were performed with Gaussian03^[33] using DFT methods. Geometries were optimised in gas phase using the B3LYP functional^[34] and a 6-31G(d) basis set. Frequency calculations were performed on the optimised structures to verify that they are minima on the PES, as well as to obtain force constants and thermodynamic data. Selected structures were re-optimised with the same functional and basis set, but including solvent effects via the PCM^[35] with acetonitrile as solvent. The difference in geometry between the gas phase and the solvated structures was less than 0.02 Å for the bond lengths and less than 4° for the bond angles and solvent effects were therefore neglected for further geometry optimisations. Single point energy calculations were performed on the B3LYP/6-31G(d) optimised structures using Ahlrich's TZVPP basis set^[36] and including solvent effects as described above. Quoted energies are those calculated at B3LYP/TZVPP level. The simplified model system described in Section 2.2 with the ketone form of the ligand was used in all calculations (see Figure 1.1).

The L¹ ligand is tetradentate and therefore has two possible substrate coordination sites. Coordination of the substrate is assumed to take place *trans* to the tertiary amine N3, as this has been shown to be the favoured coordination site in complexes of L¹. This assumption has nonetheless been tested and confirmed for selected complexes reported here, by calculating the relative energies of the two possible isomers (*trans* N3 and *trans* N7). The catalysis is performed in methanol or acetonitrile, using a catalyst: oxidant: substrate ratio of 1:10:1000. Since an aqueous solution of H₂O₂ is used, small amounts of H₂O are found in the catalytic mixture. Only solvation in acetonitrile is considered here, so the possibility of coordination of CH₃CN and H₂O in the open binding site *trans* to N7 are taken into account.

For the location of transition states the QST2 and QST3 methods, as implemented in Gaussian03, were used. The resulting optimised structures were verified as the transition states by frequency calculations and the single negative frequency was investigated using GaussView^[37], to verify that the correct transition state was obtained.

4.3. Results and Discussion

4.3.1. Preliminary calculations on L¹Fe^{II} and H₂O₂

The [L¹Fe^{II}(CH₃CN)₂]²⁺ precursor

Calculations were performed on the [L¹Fe^{II}(CH₃CN)₂]²⁺ precursor and the results compared to available experimental data. The geometry was optimised for the S=0 and S=2 spin states (convergence could not be reached for the S=1 state) and a high-spin (S=2) ground state is calculated, in agreement with experiment^[21]. The singlet state is 28.0 kJ/mol higher in energy than the quintet ground state. A Mulliken spin density of 3.80 is calculated for the iron centre in the ground state, in the region of what one would expect for a high-spin d⁶ Fe^{II} centre (four unpaired electrons), with the remaining spin density shared between the donor atoms.

Since no crystal structure has been obtained for [L¹Fe^{II}(CH₃CN)₂]²⁺, the calculated structure of was compared to the crystal structure of [L¹Fe^{II}(SCN)₂]. The correspondence is good, as can be seen from Table 4.1 and the overlay of the two structures shown in Figure 4.5. The geometric parameters of the L¹Fe fragment in [L¹Fe^{II}(CH₃CN)₂]²⁺ are practically identical to those of [L¹Fe^{II}(SCN)₂]. The bond lengths to the co-ligands are about 0.1 Å longer, but this is to be expected on the basis of the different charges of the co-ligands.

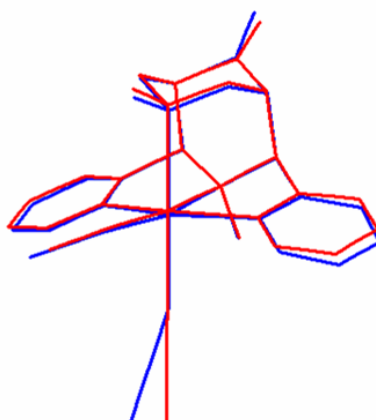


Figure 4.5. Overlay of the structures of [L¹Fe^{II}(CH₃CN)₂]²⁺ (calculated - red) and [L¹Fe^{II}(SCN)₂] (experimental - blue)

Table 4.1. Selected geometric parameters of $[L^1Fe(CH_3CN)_2]^{2+}$ and $[L^1Fe(SCN)_2]$, experimental parameters given in bold italics

Complex	$[L^1Fe(CH_3CN)_2]^{2+}$	$[L^1Fe(CH_3CN)_2]^{2+}$	$[L^1Fe(SCN)_2]$
Parameters	S=0	S=2	S=2
Bond distances (Å)			
Fe-N7	2.210	2.385	2.373
Fe-N3	2.031	2.241	2.242
Fe-Npy1	2.004	2.172	2.170
Fe-Npy2	2.004	2.170	2.176
Fe-Nac (<i>trans</i> N7)	1.935	2.131	2.038
Fe-Nac (<i>trans</i> N3)	1.938	2.234	2.117
N3...N7	2.916	3.028	2.922
Valence Angles (°)			
N7-Fe-N3	86.78	81.70	78.52
Npy1-Fe-Npy2	165.20	152.78	149.67

Homolytic cleavage of the O-O bond in free H₂O₂

With our methodology, the calculated bond length in H₂O₂ is 1.456 Å, which is around 0.2 Å less than the experimentally determined value of 1.475 Å^[38]. The H–O–O–H torsion angle of 118.68° is in better agreement with experiment (116.0°) and the O–O–H angles of 99.7° are reasonably close to the experimental value of 94.8°. The activation barrier for homolytic cleavage of the O–O bond in free H₂O₂ was calculated and compared to the experimental^[39] and a previously published DFT value^[30]. The experimental energy needed for breaking the O–O bond at 25°C is 213 kJ/mol and the energy calculated in a previous DFT study using the PW91 functional and a triple-ξ basis set with one polarisation function, as implemented in ADF, is 234 kJ/mol. We calculate a value of 238 kJ/mol, 25 kJ/mol larger than experiment, but in good agreement with the previously calculated DFT value. This is a good indication that the reaction energies and energy barriers are relatively independent of the DFT method, since we have used a hybrid functional and a double-ξ basis set. In addition, a fairly simple computational setup (rigid PES scans, varying the O...O distance in H₂O₂ and 2·OH) was used to compute this energy and zero-point corrections were not included.

4.3.2. Primary Intermediate $[L^1Fe^{II}(HOOH)(CH_3CN)]^{2+}$

For all three possible reaction pathways, the first step in the mechanistic cycle is assumed to be the nucleophilic addition of hydrogen peroxide to the iron(II) centre by ligand exchange with the *trans* N3 coordinated acetonitrile ligand. This reaction is calculated to be endothermic by 29.8 kJ/mol. The structure of the $[L^1Fe^{II}(HOOH)(CH_3CN)]^{2+}$ complex was optimised in all possible spin states and a quintet (S=2) ground state is calculated, which is shown in Figure 4.6. The singlet and triplet states lie 47.4 and 63.7 kJ/mol higher in energy than the ground state respectively.

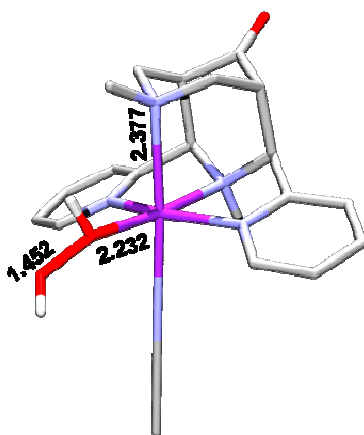


Figure 4.6. Optimised geometry of primary intermediate $[L^1Fe^{II}(HOOH)(CH_3CN)]^{2+}$ in its high-spin (S=2) ground state

Selected bond lengths and stretching frequencies, as well as the relative energies of the different spin states, are given in Table 4.2 (O1 = *trans* N3 bound oxygen atom of H₂O₂, O2 = unbound/*trans* N7 bound oxygen atom). The full geometries are given in Addendum A. In all three spin states the hydrogen peroxide is monodentately coordinated to the iron centre, as can be seen from the Fe...O2 distances. The O–O bond length in the quintet ground state is 1.452 Å, which is only slightly shorter than the value of 1.456 Å calculated for unbound H₂O₂. However, the O–O stretching frequency is lowered from 939 cm⁻¹ in H₂O₂ to 911 cm⁻¹ in $[L^1Fe^{II}(HOOH)(CH_3CN)]^{2+}$, which indicates a weakening of the O–O bond upon coordination to the iron centre. The Mulliken spin density of 3.79 on the iron centre is

relatively unchanged from that in $[L^1Fe^{II}(CH_3CN)]^{2+}$, indicating that there is minimal charge donation to the H_2O_2 ligand.

Since a small amount of water is present in the reaction mixture of the catalytic experiments, ligand exchange of the coordinated acetonitrile with water to form $[L^1Fe^{II}(HOOH)(H_2O)]^{2+}$ is, in principle, possible. The reaction is calculated to be thermoneutral but, since ligand exchange reactions in high-spin Fe^{II} complexes are known to follow dissociative reaction mechanisms^[40], should proceed via a short lived pentacoordinate $[L^1Fe^{II}(HOOH)]^{2+}$ intermediate, the formation of which is endothermic by 22.0 kJ/mol.

Table 4.2. Selected geometric parameters, stretching frequencies and relative energies of the spin states in the Fe^{II} -hydrogen peroxide complexes of L^1

	Interatomic distances (Å)			ν (cm^{-1})	ΔE (kJ/mol)
	Fe-O1	Fe-O2	O1-O2	O1-O2	0°
$[L^1Fe^{II}(HOOH)]^{2+}$					
S=0	2.204	2.147	1.455	930	65.9
S=1	2.005	2.818	1.468	837	45.7
S=2	2.216	2.878	1.454	918	0.0
$[L^1Fe^{II}(CH_3CN)(HOOH)]^{2+}$					
S=0	2.067	3.065	1.462	860	47.4
S=1	2.157	3.156	1.457	889	63.7
S=2	2.232	3.173	1.452	911	0.0
$[L^1Fe^{II}(H_2O)(HOOH)]^{2+}$					
S=0	2.077	3.040	1.473	800	63.6
S=1	2.040	3.063	1.479	759	71.4
S=2	2.349	3.298	1.456	898	0.0

The structures of the $[L^1Fe^{II}(HOOH)(H_2O)]^{2+}$ and $[L^1Fe^{II}(HOOH)]^{2+}$ complexes were also optimised in all possible spin states and both have quintet (S=2) ground states. The S=0 and S=1 states are 63.6 and 71.4 kJ/mol higher in energy in $[L^1Fe^{II}(HOOH)(H_2O)]^{2+}$ and 65.9 and 45.7 kJ/mol higher in $[L^1Fe^{II}(HOOH)]^{2+}$. These results are also summarised in Table 4.2. Coordination of hydrogen peroxide to the iron centre is η^1 in all cases but that of singlet $[L^1Fe^{II}(HOOH)]^{2+}$, and this can be rationalised in terms of ligand field theory. We define the coordinate system such that the Fe–N7 bond lies along the z-axis, the Fe–N_{py} bonds along

4. Oxidation Catalysis with the Iron(II) Complex of a tetradentate 3,7-Diazabicyclo[3.3.1]nonane Derivative

the y-axis and the Fe–N3 bond along the y-axis. Low-spin ($S=0$) Fe^{II} has a $(t_{2g})^6(e_g)^0$ configuration; both the e_g orbitals are unoccupied, which makes occupation of both coordination sites favourable. In $[\text{L}^1\text{Fe}^{\text{II}}(\text{HOOH})(\text{CH}_3\text{CN})]^{2+}$ and $[\text{L}^1\text{Fe}^{\text{II}}(\text{HOOH})(\text{H}_2\text{O})]^{2+}$ however, the second coordination site is already occupied, whereas in $[\text{L}^1\text{Fe}^{\text{II}}(\text{HOOH})]^{2+}$ it is free for the coordination of the second oxygen atom of the hydrogen peroxide. In the intermediate- and high-spin states one ($S=1$) or both ($S=2$) of these orbitals are singly occupied and the H_2O_2 coordinates as a monodentate ligand in the direction of the empty or singly occupied $d_{x^2-y^2}$ orbital (*trans* N3), regardless of whether an additional co-ligand is coordinated or not.

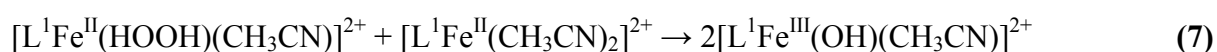
In the $S=2$ ground state of $[\text{L}^1\text{Fe}^{\text{II}}(\text{HOOH})]^{2+}$ the O–O stretching frequency is 918 cm^{-1} , which is lowered to 837 cm^{-1} in the $S=1$ state, indicating a weakening of the O–O bond. This is also reflected in O–O bond lengths, which increase from 1.453 \AA ($S=2$) to 1.468 \AA ($S=1$), while the Fe–O bond lengths decrease correspondingly from 2.216 \AA ($S=2$) to 2.005 \AA ($S=1$). The $S=1$ state is therefore activated for bond cleavage with respect to the $S=2$ ground state.

4.3.3. The Fe^{III}-hydroperoxo – Fe^V-oxo-hydroxo pathway (A)

The first reaction mechanism we have considered is shown in pathway **A** of Figure 4.4 and can be divided into four steps, namely: (i) O–O bond cleavage in the primary intermediate $[\text{L}^1\text{Fe}^{\text{II}}(\text{HOOH})(\text{CH}_3\text{CN})]^{2+}$, to form an Fe^{III}-hydroxo intermediate, $[\text{L}^1\text{Fe}^{\text{III}}(\text{OH})(\text{CH}_3\text{CN})]^{2+}$; (ii) reaction of $[\text{L}^1\text{Fe}^{\text{III}}(\text{OH})(\text{CH}_3\text{CN})]^{2+}$ with a second molecule of H₂O₂ to form $[\text{L}^1\text{Fe}^{\text{III}}(\text{OOH})(\text{CH}_3\text{CN})]^{2+}$ and H₂O; (iii) abstraction of the *trans* N7 bound acetonitrile in $[\text{L}^1\text{Fe}^{\text{III}}(\text{OOH})(\text{CH}_3\text{CN})]^{2+}$ to form $[\text{L}^1\text{Fe}^{\text{III}}(\text{OOH})]^{2+}$ and (iv) heterolytic cleavage of the O–O bond to form an Fe^V-oxo-hydroxo intermediate, $[\text{L}^1\text{Fe}^{\text{V}}(\text{O})(\text{OH})]^{2+}$. Formation of an Fe^{III}-hydroxo intermediate and its decomposition to Fe^{III}-hydroperoxo has been spectroscopically observed for ligands such as N4py^[41]. Note that steps (iii) and (iv) have been regarded independently for the computational purposes (i.e. a dissociative mechanism is assumed), whereas in reality they will not be independent of each other, since ligand exchange reactions in Fe^{III} complexes are generally associative in nature^[40]. Not shown in Figure 4.4, but also discussed here, is the possibility of homolytic cleavage of the O–O bond in $[\text{L}^1\text{Fe}^{\text{III}}(\text{OOH})(\text{CH}_3\text{CN})]^{2+}$ to form $[\text{L}^1\text{Fe}^{\text{IV}}(\text{O})(\text{CH}_3\text{CN})]^{2+}$ and an •OH radical.

Formation of $[\text{L}^1\text{Fe}^{\text{III}}(\text{OH})(\text{CH}_3\text{CN})]^{2+}$

The formation of an Fe^{III}-hydroxo intermediate may proceed directly via homolytic cleavage of the O–O bond in $[\text{L}^1\text{Fe}^{\text{II}}(\text{HOOH})(\text{CH}_3\text{CN})]^{2+}$ to form $[\text{L}^1\text{Fe}^{\text{III}}(\text{OH})(\text{CH}_3\text{CN})]^{2+}$ and an •OH radical ((**6**)), or via the reaction of $[\text{L}^1\text{Fe}^{\text{II}}(\text{HOOH})(\text{CH}_3\text{CN})]^{2+}$ with a second molecule of $[\text{L}^1\text{Fe}^{\text{II}}(\text{CH}_3\text{CN})_2]^{2+}$ to form a dinuclear complex, which subsequently undergoes homolytic cleavage of the O–O bond to form two $[\text{L}^1\text{Fe}^{\text{III}}(\text{OH})(\text{CH}_3\text{CN})]^{2+}$ units ((**7**)):



The total reaction energy of direct homolytic cleavage in $[\text{L}^1\text{Fe}^{\text{II}}(\text{HOOH})(\text{CH}_3\text{CN})]^{2+}$ (reaction (**6**)) is 5.3 kJ/mol and the energy barrier is calculated to be approximately 35 kJ/mol

in the gas phase. The transition state could not be fully optimised however, so the effect of solvation has not been taken into account. The general effect of solvation is to increase the energy barriers by 5–20 kJ/mol (6-31G(d) vs. TZVPP + PCM), so it is likely that the energy barrier for this reaction in solution is in the region of 50 kJ/mol.

The total enthalpy of formation via a dinuclear intermediate (reaction (7)) is -86.0 kJ/mol per unit of reactant. Due to the size of the system, no attempt to optimise the dinuclear intermediate was made, so the height of the energy barrier for this reaction is unknown. However, the extremely low concentration of the Fe^{II} catalyst in the reaction mixture makes it statistically improbable that the $[\text{L}^1\text{Fe}^{\text{II}}(\text{HOOH})(\text{CH}_3\text{CN})]^{2+}$ complex will come into contact with a further $[\text{L}^1\text{Fe}^{\text{II}}(\text{CH}_3\text{CN})_2]^{2+}$ before a number of alternative reactions take place (see pathways **B** and **C** below). In addition, even if the enthalpy of formation of the dinuclear complex is favourable, this will be countered by a large, unfavourable entropy term.

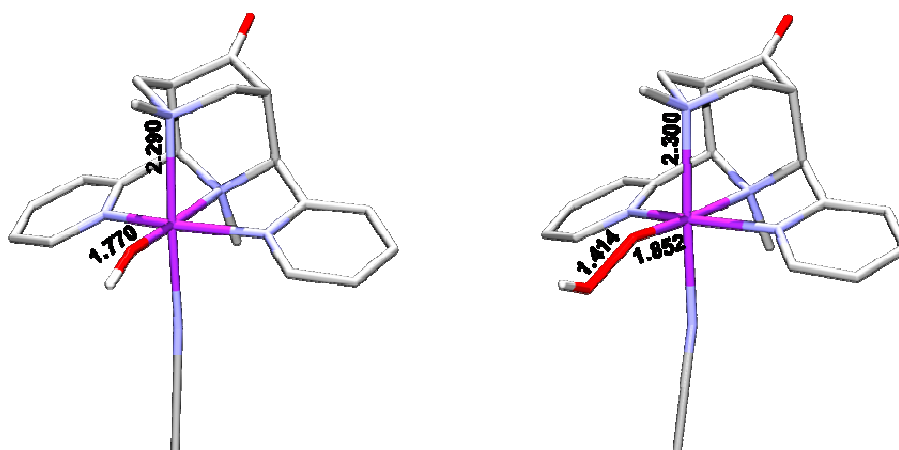


Figure 4.7. The geometries of $[\text{L}^1\text{Fe}^{\text{III}}(\text{OH})(\text{CH}_3\text{CN})]^{2+}$ and $[\text{L}^1\text{Fe}^{\text{III}}(\text{OOH})(\text{CH}_3\text{CN})]^{2+}$ in their high-spin ($S=5/2$) ground states

The geometry of $[\text{L}^1\text{Fe}^{\text{III}}(\text{OH})(\text{CH}_3\text{CN})]^{2+}$ was optimised for all possible spin states and a high-spin ($S=5/2$) ground state with an Fe–O bond length of 1.770 Å is calculated. The $S=3/2$ and $S=1/2$ states are 28.7 and 21.3 kJ/mol higher in energy than the ground state with Fe–O bond lengths of 1.775 Å and 1.783 Å respectively. The Fe–O bond lengths are shortened by approximately 0.2 to 0.3 Å relative to $[\text{L}^1\text{Fe}^{\text{II}}(\text{HOOH})(\text{CH}_3\text{CN})]^{2+}$. Figure 4.7 shows the calculated geometries of $[\text{L}^1\text{Fe}^{\text{III}}(\text{OH})(\text{CH}_3\text{CN})]^{2+}$ and $[\text{L}^1\text{Fe}^{\text{III}}(\text{OOH})(\text{CH}_3\text{CN})]^{2+}$.

Formation of $[L^1Fe^{III}(OOH)(CH_3CN)]^{2+}$ and $[L^1Fe^{III}(OOH)]^{2+}$

The formation of $[L^1Fe^{III}(OOH)(CH_3CN)]^{2+}$ from $[L^1Fe^{III}(OH)(CH_3CN)]^{2+}$ via ligand exchange is calculated to be approximately thermoneutral (+0.9 kJ/mol). Removal of the acetonitrile coordinated *trans* to N7 to form the pentacoordinate $[L^1Fe^{III}(OOH)]^{2+}$ complex is endothermic by 26.8 kJ/mol and ligand exchange to form $[L^1Fe^{III}(OOH)(H_2O)]^{2+}$ has a reaction energy of 4.6 kJ/mol.

Table 4.3. Fe–O and O–O bond distances and frequencies in the Fe^{III} -hydroperoxo complexes of L^1

	Bond length (Å)		ν (cm^{-1})	ΔE (kJ/mol)	
	Fe-O1	O1-O2	O1-O2	0°C	25°C
$[L^1Fe^{III}(OOH)]^{2+}$					
S=1/2	1.804	1.462	888	9.5	5.8
S=3/2	1.760	1.450	877	0.0	0.0
S=5/2	1.829	1.416	933	0.9	2.4
$[L^1Fe^{III}(CH_3CN)(OOH)]^{2+}$					
S=1/2	1.775	1.442	890	2.3	0.0
S=3/2	1.777	1.438	918	12.4	14.1
S=5/2	1.852	1.414	940	0.0	2.9
$[L^1Fe^{III}(H_2O)(OOH)]^{2+}$					
S=1/2	1.790	1.460	866	10.9	5.6
S=3/2	1.784	1.450	894	12.6	11.3
S=5/2	1.862	1.428	936	0.0	0.0

The relative energies of spin states of the Fe^{III} -hydroperoxo complexes at 0° and 25°C are given in Table 4.3, along with selected bond lengths and the O–O stretching frequencies. While the $[L^1Fe^{III}(OOH)(CH_3CN)]^{2+}$ complex is also predicted to have a high-spin (S=5/2) ground state, the low-spin (S=1/2) state lies only 2.3 kJ/mol higher in energy and the S=3/2 state 12.4 kJ/mol higher. For the $[L^1Fe^{III}(OOH)]^{2+}$ complex the S=3/2 and S=5/2 states are practically degenerate and the low-spin (S=1/2) state has an energy of 9.5 kJ/mol relative to the ground state. The ground state of $[L^1Fe^{III}(OOH)(H_2O)]^{2+}$ is again high-spin (S=5/2) and the destabilisation of the S=3/2 and S=1/2 states with respect to the ground state is 12.6 and 10.9 kJ/mol, respectively.

The energies discussed above include zero-point (0°C), but not thermal (25°C) corrections. When these are added, the low-spin (S=1/2) state of the $[L^1Fe^{III}(OOH)(CH_3CN)]^{2+}$ complex becomes the ground state and the S=3/2 and S=5/2 states then have energies of 14.1 and 2.9 kJ/mol with respect to the S=1/2 ground state. This is the only intermediate for which the ground spin states change depending on whether only zero-point or also thermal corrections are added to the energy and indicates a spin crossover from S=5/2 to S=1/2 at a temperature somewhere between 0° and 25° C. These results are not unexpected, since the $[L^1Fe^{III}(OO^tBu)]^{2+}$ complex lies close enough to the spin-crossover limit that a spin state crossover can be induced by a change in temperature and/or solvent^[27]. For the $[L^1Fe^{III}(OOH)(H_2O)]^{2+}$ and $[L^1Fe^{III}(OOH)]^{2+}$ complexes, the calculated ground spin state does not change when thermal corrections are added, although the energy difference between the high-spin (S=5/2) and low-spin (S=1/2) states is approximately halved.

O-O bond cleavage in $[LFe^{III}(OOH)(CH_3CN)]^{2+}$ and $[LFe^{III}(OOH)]^{2+}$

Homolytic cleavage of the O–O bond in $[L^1Fe^{III}(OOH)(CH_3CN)]^{2+}$ leads to the formation of $[L^1Fe^{IV}(O)(CH_3CN)]^{2+}$ and an $\cdot OH$ radical. This reaction is calculated to be endothermic by 99.5 kJ/mol, which is highly unfavourable and similar to the reaction energy calculated for the analogous reaction in bleomycin^[6], while the reaction of $[(TPA)Fe^{III}(OOH)(H_2O)]^{2+}$ to $[(TPA)Fe^{IV}(O)(H_2O)]^{2+}$ has a significantly smaller reaction energy of 79 kJ/mol^[42].

The product of heterolytic O–O bond cleavage in $[L^1Fe^{III}(OOH)]^{2+}$, on the other hand, is postulated to be an $[L^1Fe^V(O)(OH)]^{2+}$ complex, in which the formed hydroxide ion is immediately trapped by the iron centre. This reaction is slightly exothermic (–4.10 kJ/mol) and has an energy barrier of 83.8 kJ/mol. It must be kept in mind however, that removing the *trans* N7 coordinated acetonitrile molecule costs 26.8 kJ/mol, making the total formation of $[L^1Fe^V(O)(OH)]^{2+}$ and CH_3CN from $[L^1Fe^{III}(OOH)(CH_3CN)]^{2+}$ endothermic by 22.7 kJ/mol. This is practically identical to the reaction energy of 21 kJ/mol calculated for the formation of $[(TPA)Fe^V(O)(OH)]^{2+}$ from $[(TPA)Fe^{III}(OOH)(H_2O)]^{2+}$ ^[42]. Figure 4.8 shows the calculated

structures of the reactant, transition state and product of this reaction, including relevant bond lengths and relative energies.

The geometry of $[L^1Fe^V(O)(OH)]^{2+}$ was optimised for both the $S=1/2$ and $S=3/2$ spin states. The ground spin state is the same as that of $[L^1Fe^{III}(OOH)]^{2+}$ ($S=3/2$), which implies that the reaction will be facilitated by the removal of the *trans* N7 bound acetonitrile in $[L^1Fe^{III}(OOH)(CH_3CN)]^{2+}$, which does not have a quartet ground state. In addition, the near degeneracy of the $S=1/2$ and $S=5/2$ spin states of $[L^1Fe^{III}(OOH)(CH_3CN)]^{2+}$ and the $S=5/2$ and $S=3/2$ spin states of $[L^1Fe^{III}(OOH)]^{2+}$ should facilitate the spin state crossover required prior to cleavage of the O–O bond.

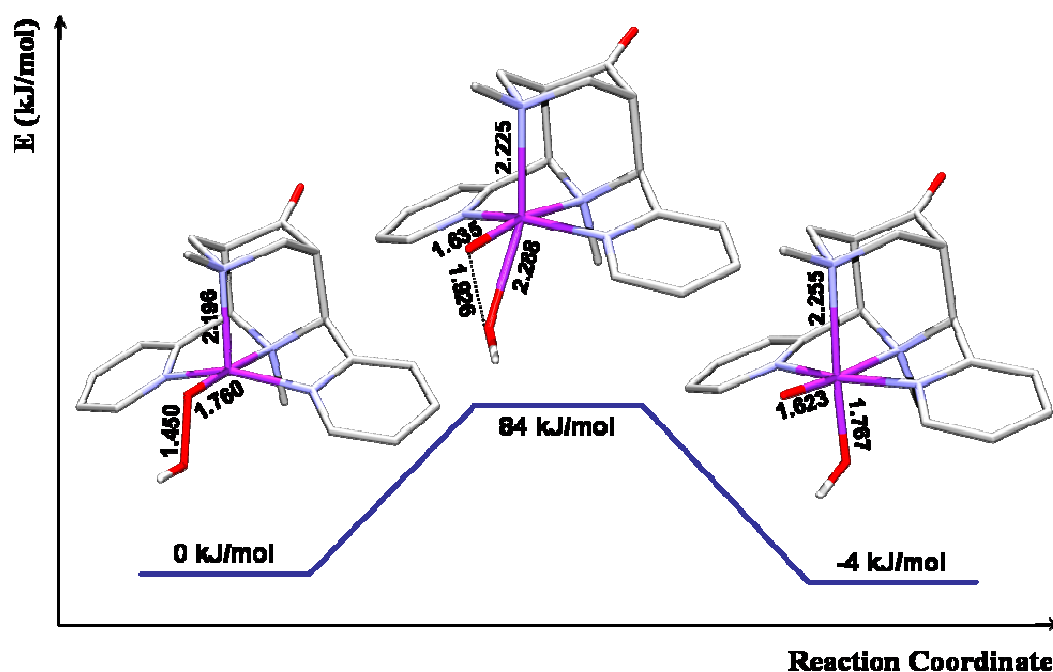


Figure 4.8. The reactant, transition state and product of heterolytic cleavage in $[L^1Fe^{III}(OOH)]^{2+}$, on the $S=3/2$ surface

The Fe–O bond distance in the ground state of $[L^1Fe^V(O)(OH)]^{2+}$ is 1.623 Å, which is around 0.04 Å shorter than the corresponding bond length calculated for the $[(TPA)Fe^V(O)(OH)]^{2+}$ complex (1.665 Å)^[42]. While this difference may be partially due to the use of different methodologies, it is likely that L^1 does induce shorter bond lengths than TPA, due to the strong in-plane binding *trans* to the tertiary amine donor N3.

4. Oxidation Catalysis with the Iron(II) Complex of a tetradentate 3,7-Diazabicyclo[3.3.1]nonane Derivative

Although high-spin Fe^{V} formally has three unpaired electrons, one expects a spin density on iron of around 2, due to the delocalisation of two of the unpaired electrons in the two $\text{Fe}=\text{O}$ π^* orbitals^[43]. Indeed, a spin density of 2.07 is calculated on the iron centre, with the bulk of the remaining spin density on the oxo ligand (0.87) and a small amount on the oxygen of the hydroxy ligand (0.16).

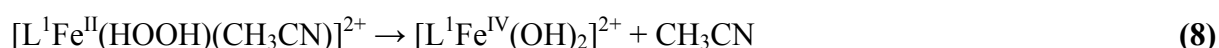
In summary therefore, O–O bond cleavage in $[\text{L}^{\text{I}}\text{Fe}^{\text{II}}(\text{HOOH})(\text{CH}_3\text{CN})]^{2+}$ to form $[\text{L}^{\text{I}}\text{Fe}^{\text{III}}(\text{OH})(\text{CH}_3\text{CN})]^{2+}$ and an $\cdot\text{OH}$ radical has a relatively low energy barrier, but an unfavourable enthalpy. Formation of $[\text{L}^{\text{I}}\text{Fe}^{\text{III}}(\text{OH})(\text{CH}_3\text{CN})]^{2+}$ via a dinuclear intermediate is exothermic, but is expected to have a highly unfavourable entropy term. In the event that the $[\text{L}^{\text{I}}\text{Fe}^{\text{III}}(\text{OOH})(\text{CH}_3\text{CN})]^{2+}$ intermediate is formed, the formation of an $[\text{L}^{\text{I}}\text{Fe}^{\text{V}}(\text{O})(\text{OH})]^{2+}$ complex, proposed to be the reactive intermediate in the oxidation of olefin with TPA^[42,44], is unlikely to take place due to an unfavourable reaction enthalpy and a high energy barrier.

4.3.4. The Fe^{IV}-dihydroxo – Fe^{IV}-oxo-aqua pathway (B)

The second possible reaction mechanism is shown in pathway **B** of Figure 4.4 and can also be divided into four steps, namely: (i) abstraction of the *trans* N7 bound acetonitrile in the primary intermediate [L¹Fe^{II}(HOOH)(CH₃CN)]²⁺; (ii) heterolytic cleavage of the O–O bond in [L¹Fe^{II}(HOOH)]²⁺ to form an Fe^{IV}-dihydroxo intermediate, [L¹Fe^{IV}(OH)₂]²⁺; (iii) proton transfer from the *trans* N3 to the *trans* N7 bound hydroxide of [L¹Fe^{IV}(OH)₂]²⁺ to form [L¹Fe^{IV}(O)(H₂O)]²⁺ and (iv) ligand exchange of to form [L¹Fe^{IV}(O)(CH₃CN)]²⁺. Note that, as for the reaction of [L¹Fe^{III}(OOH)(CH₃CN)]²⁺ to [L¹Fe^V(O)(OH)]²⁺, a dissociative mechanism is assumed and steps (i) and (ii) are considered separately. However, since ligand exchange reactions in high-spin Fe^{II} complexes are generally dissociative in nature^[40], the computational simplification is justified in this case. Not shown in Figure 4.4, but also discussed here, is the possibility of ligand exchange of acetonitrile with water in [L¹Fe^{II}(HOOH)(CH₃CN)]²⁺, followed by homolytic cleavage of the O–O bond in the [L¹Fe^{II}(HOOH)(H₂O)]²⁺ complex to form [L¹Fe^{IV}(OH)₂]²⁺ and water.

Reaction pathway from [LFe^{II}(HOOH)(CH₃CN)]²⁺ to [LFe^{IV}(OH)₂]²⁺

As discussed above, the formation of [L¹Fe^{IV}(OH)₂]²⁺ from [L¹Fe^{II}(HOOH)(CH₃CN)]²⁺ can be divided into two parts, namely, abstraction of the *trans* N7 bound acetonitrile to form a pentadentate [L¹Fe^{II}(HOOH)]²⁺ species with an open coordination site, followed by O–O bond heterolysis in [L¹Fe^{II}(HOOH)]²⁺. Removal of acetonitrile is endothermic by 22.0 kJ/mol (see Section 4.3.4), but the formation of [L¹Fe^{IV}(OH)₂]²⁺ from [L¹Fe^{II}(HOOH)]²⁺ is exothermic by 93.4 kJ/mol, bringing the total energy of reaction **(8)** to –71.4 kJ/mol:



The ground state of [L¹Fe^{IV}(OH)₂]²⁺ is calculated to have an S=1 configuration, by a margin of 11.2 kJ/mol with respect to the high-spin (S=2) state. The S=0 state lies 98.1 kJ/mol higher in energy than the ground state. Because the reactant and product of O–O bond heterolysis

have different spin states, a spin-forbidden transition from the quintet to the triplet state must take place somewhere along the reaction path, and both spin states are considered. The geometries of the reactants, transition states and products of the reaction of $[L^1Fe^{II}(HOOH)]^{2+}$ to $[L^1Fe^{IV}(OH)_2]^{2+}$ for both $S=1$ and $S=2$, including relevant bond lengths and relative energies, are shown in Figure 4.9.

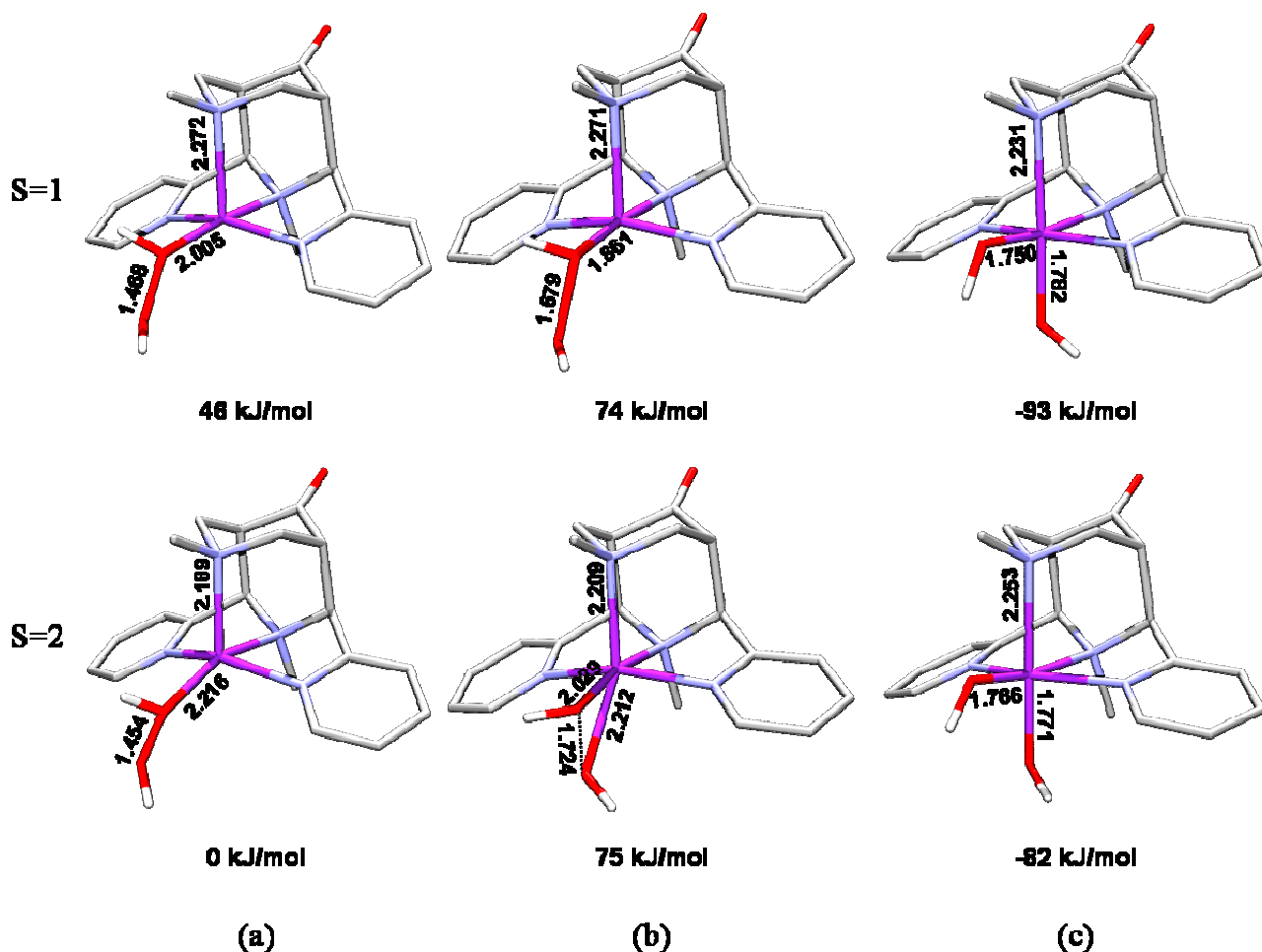


Figure 4.9. The reactant (a), transition state (b) and product (c) of heterolytic O–O bond cleavage in $[L^1Fe^{II}(HOOH)]^{2+}$ for $S=1$ and $S=2$

Investigation of the potential energy surfaces for the $S=1$ and $S=2$ states reveals that the transition states are practically degenerate, despite having very different geometries. Aside from the obvious shortening of the Fe–O1 (O1 and O2 defined as in Section 4.3.2) and lengthening of the O–O bond, the geometry of the triplet transition state is very similar to that of the reactant (see Figure 4.7(b)). The Fe–N7 bond lengths are identical, the Fe–O1–O2

angle is hardly changed (from 107.5° in the reactant to 105.2° in the transition state) and formation of the Fe–O2 bond has not yet begun. This is in agreement with the low energy barrier of 27.8 kJ/mol. However, since the triplet state of the reactant is destabilised by 45.7 kJ/mol relative to the quintet ground state (see Table 4.2 and Figure 4.9(a)), the transition state on the triplet surface lies 73.5 kJ/mol higher in energy than the quintet ground state of $[L^1Fe^{II}(HOOH)]^{2+}$. The transition state on the quintet surface is 74.6 kJ/mol higher in energy than the reactant, but practically degenerate with the triplet transition state (Figure 4.9(b)). In keeping with the higher energy barrier, the geometry of the transition state on the quintet surface is a great deal closer to that of the product than in the triplet state. The Fe–O1–O2 angle has decreased from 101.3° in the reactant to 71.7° in the transition state, the Fe–N7 bond is slightly lengthened, the Fe–O2 bond is already formed and the O–O bond is elongated. From the large energy difference between the S=1 and S=2 states of the reactant, an early spin-state crossover can be excluded, while the near degeneracy of transition states on the triplet and quintet surfaces strongly suggests that the spin-crossing takes place shortly before to the transition state is formed.

Coordination of hydrogen peroxide to the FeL^1 fragment therefore greatly reduces the energy required to cleave the O–O bond, from ~ 240 kJ/mol in free H_2O_2 to 73.5 kJ/mol in $[L^1Fe^{II}(HOOH)]^{2+}$. This is in agreement with the observed weakening of the O–O bond in coordinated H_2O_2 , as discussed above (see Section 4.3.2).

Formation of $[LFe^{IV}(OH)_2]^{2+}$ from $[LFe^{II}(HOOH)(H_2O)]^{2+}$

A further possibility for formation of $[L^1Fe^{IV}(OH)_2]^{2+}$ is a “water-assisted” mechanism such as that postulated for $[(H_2O)_5Fe^{II}(HOOH)]^{2+}$ ^[30]. For our system, this involves ligand exchange of CH_3CN with H_2O to form $[L^1Fe^{II}(HOOH)(H_2O)]^{2+}$, followed by the formation of a short-lived $[L^1Fe^{III}(H_2O)(OH)]^{2+}$ species and an $\cdot OH$ radical, which immediately abstracts a hydrogen atom from the *trans* N7 bound H_2O molecule, forming as final product the $[L^1Fe^{IV}(OH)_2]^{2+}$ complex and a water molecule hydrogen bonded to the *trans* N7 bound hydroxyl ligand. This is shown schematically in Figure 4.10.

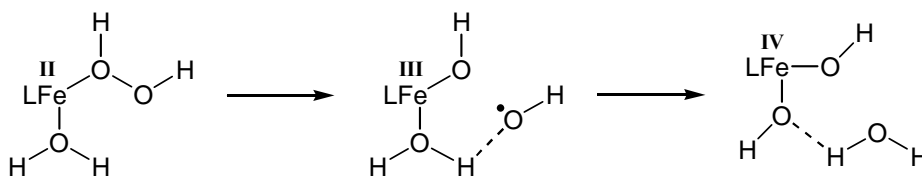


Figure 4.10. Schematic representation of the formation of $[L^1Fe^{IV}(OH)_2]^{2+}$ from $[L^1Fe^{II}(HOOH)(H_2O)]^{2+}$

As discussed previously, the thermoneutral ligand exchange proceeds via a pseudo pentacoordinate intermediate and has an energy barrier of 22.0 kJ/mol. Since the ground state of the $[L^1Fe^{II}(HOOH)(H_2O)]^{2+}$ complex also has an S=2 electronic configuration, this reaction again involves a forbidden spin state crossover. The transition state for O–O bond cleavage on the high-spin (S=2) surface has an energy of 68.8 kJ/mol relative to the S=2 ground state of the reactant, which is lower than the energy of the S=1 reactant (71.4 kJ/mol). The energy barrier on the S=1 surface is only 15.2 kJ/mol, but the transition state has an energy of 86.5 kJ/mol, with respect to the S=2 ground state. This indicates that the O–O bond cleavage will take place on the quintet surface and that the spin-crossover occurs after the transition state has been formed.

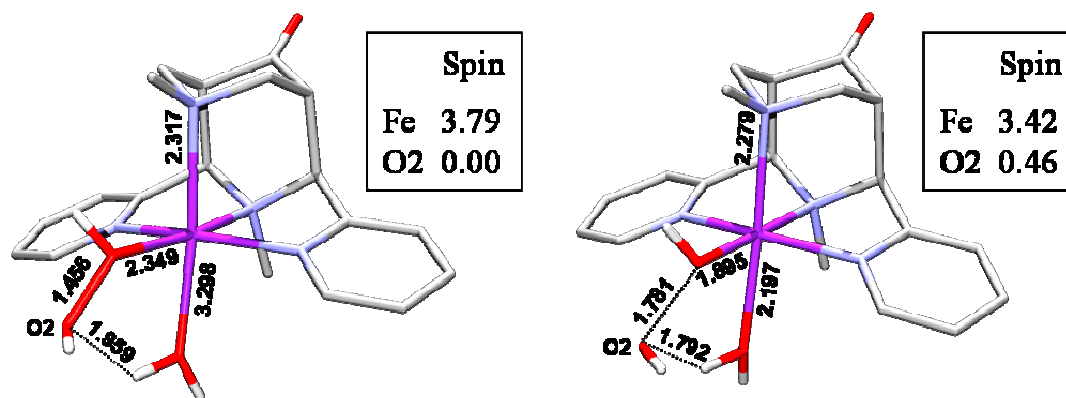


Figure 4.11. The reactant and transition state for homolytic cleavage in S=2 $[L^1Fe^{II}(HOOH)(H_2O)]^{2+}$, showing the Mulliken spin densities on Fe and O2

The geometries of the quintet reactant and transition state are shown in Figure 4.11. The Fe–O1 bond length has decreased from 2.349 Å in the reactant to 1.895 Å in the transition state and the O1–O2 distance increased from 1.456 Å to 1.781 Å. The Fe^{III} intermediate and

the second transition state were not optimised, since the reaction is analogous to the formation of $[L^1Fe^{IV}(O)(OH)]^+$ from $[L^1Fe^{II}(OOH)(H_2O)]^+$ (see Section 4.3.5 below), for which the energy barrier of the proton transfer step is shown to be negligible in comparison to that of O–O bond cleavage. Also shown in Figure 4.11 are the spin densities on Fe and O2 in the quintet reactant and transition states. In the reactant, the spin density on the Fe is 3.79, as one would expect for high-spin Fe^{II} (d^6 , four unpaired electrons), and there is no net spin density on O2. In the transition state, the spin density on the iron has decreased to 3.42 and there is a net spin density of 0.46 on O2, indicating a transition to an Fe^{III} intermediate (d^5 , three unpaired electrons) and an $\cdot OH$ radical.

The energy barrier of 68.8 kJ/mol is comparable to the energy barrier of 73.5 kJ/mol for O–O bond cleavage in $[L^1Fe^{II}(HOOH)]^{2+}$. Since the energy barrier for the ligand exchange of CH_3CN with H_2O is also low, the main factor determining which pathway is followed will be the relative concentrations of acetonitrile and water. Under the catalytic conditions, direct O–O bond cleavage in $[L^1Fe^{II}(HOOH)]^{2+}$ should take place almost exclusively.

Formation of $[LFe^{IV}(O)(H_2O)]^{2+}$ from $[LFe^{IV}(OH)_2]^{2+}$

Proton transfer from the *trans* N3 to the *trans* N7 bound hydroxide of $[L^1Fe^{IV}(OH)_2]^{2+}$ leads to the formation of an $[L^1Fe^{IV}(O)(H_2O)]^{2+}$ complex. The geometry of this species was optimised for the S=1 and S=2 states and the quintet state is calculated to be 14.2 kJ/mol more stable than the triplet state. The total reaction energy of reaction (9) is –12.7 kJ/mol:



Since the reactant, $[L^1Fe^{IV}(OH)_2]^{2+}$, has a triplet ground state, this reaction again involves a forbidden spin-state crossover and both the S=1 and S=2 pathways were considered. The activation barrier on the S=2 surface is 85.3 kJ/mol, bringing the total energy of the quintet transition state to 96.5 kJ/mol with respect to the triplet ground state of $[L^1Fe^{IV}(OH)_2]^{2+}$. The S=1 transition state, on the other hand, lies 74.7 kJ/mol higher in energy than the reactant and

is therefore the more likely pathway of the two. The spin-crossover is therefore expected to take place close to or in the product state.

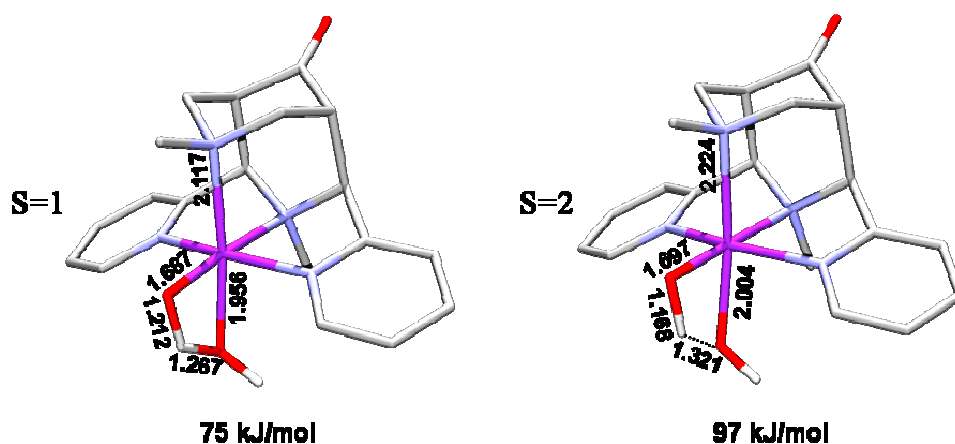


Figure 4.12. Transition states for the reaction of $[L^1Fe^{IV}(OH)_2]^{2+}$ to $[L^1Fe^{IV}(O)(H_2O)]^{2+}$ for S=1 and S=2, including energies relative to the S=1 $[L^1Fe^{IV}(OH)_2]^{2+}$ intermediate

Figure 4.12 shows the geometries of the transition states and energies relative to the ground state of the reactant, $[L^1Fe^{IV}(OH)_2]^{2+}$, for both the S=1 and S=2 states. Unlike the transition states for the O–O homolysis, the geometries of the transition states for the proton transfer are similar for the S=1 and S=2 pathways.

Water-assisted pathway for the reaction of $[LFe^{IV}(OH)_2]^{2+}$ to $[LFe^{IV}(O)(H_2O)]^{2+}$

An alternative to the direct proton transfer in $[L^1Fe^{IV}(OH)_2]^{2+}$ is a water-assisted mechanism, where an H_2O molecule in the second coordination sphere acts as a proton shuffle, abstracting a proton from the *trans* N3 bound hydroxide and transferring one of its own to the second, *trans* N7 bound hydroxide. This is shown schematically in Figure 4.13.

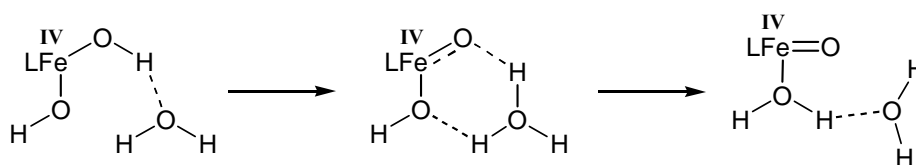


Figure 4.13: Schematic representation of the water-assisted formation of $[L^1Fe^{IV}(O)(H_2O)]^{2+}$ from $[L^1Fe^{IV}(OH)_2]^{2+}$

4. Oxidation Catalysis with the Iron(II) Complex of a tetradentate 3,7-Diazabicyclo[3.3.1]nonane Derivative

One expects this reaction to be more favourable than direct proton transfer, due to the fact that a 5-membered ring is formed in the transition state, instead of the strained 4-membered ring formed in the transition state of the direct proton transfer reaction. Indeed, the energy barrier on the S=1 surface is lowered from 74.7 kJ/mol in the direct reaction, to only 28.1 kJ/mol in the water-assisted mechanism. The S=2 transition state was not optimised, since we have shown that the spin state crossover is likely to take place in the $\text{Fe}^{\text{IV}}=\text{O}$ product and because the spin state of the metal is unlikely to affect the energy barrier of a proton transfer reaction. Figure 4.14 shows the geometry of the transition state on the triplet surface. The Fe–O1 bond length in the water-assisted transition state is 1.661 Å, slightly shorter to the 1.687 Å found in the direct proton transfer transition state in the triplet state.

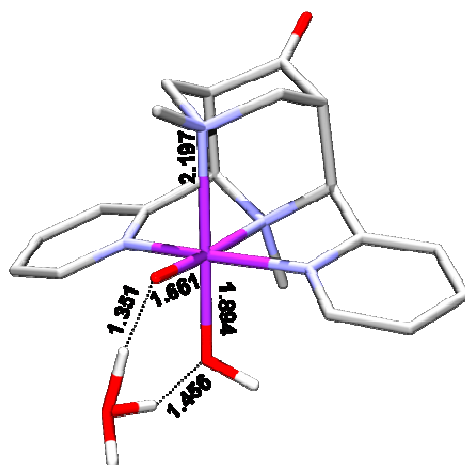


Figure 4.14. The transition state on the S=1 surface for the water-assisted proton transfer reaction of $[\text{L}^1\text{Fe}^{\text{IV}}(\text{OH})_2]^{2+}$ to $[\text{L}^1\text{Fe}^{\text{IV}}(\text{O})(\text{H}_2\text{O})]^{2+}$

4.3.5. The Fe^{II}-hydroperoxo – Fe^{IV}-oxo-hydroxo pathway (C)

The third reaction mechanism that has been studied is shown in pathway C of Figure 4.4 and can be divided into three steps, namely: (i) deprotonation of the primary intermediate $[L^1Fe^{II}(HOOH)(CH_3CN)]^{2+}$ to form $[L^1Fe^{II}(OOH)(CH_3CN)]^+$; (ii) abstraction of the *trans* N7 bound acetonitrile to form $[L^1Fe^{II}(OOH)]^+$ and (iii) heterolytic cleavage of the O–O bond in $[L^1Fe^{II}(OOH)]^+$ to form an Fe^{IV}-oxo-hydroxo intermediate, $[L^1Fe^{IV}(O)(OH)]^+$. As for the previous two pathways, a dissociative mechanism is assumed and steps (ii) and (iii) are considered individually. Not shown in Figure 4.4, but also discussed here, is the possibility of ligand exchange of acetonitrile with water to form $[L^1Fe^{II}(OOH)(H_2O)]^+$, followed by homolytic cleavage of the O–O bond to form $[L^1Fe^{IV}(O)(OH)]^+$ and H₂O, analogous to the formation of $[L^1Fe^{IV}(OH)_2]^{2+}$ from $[L^1Fe^{II}(HOOH)(H_2O)]^{2+}$.

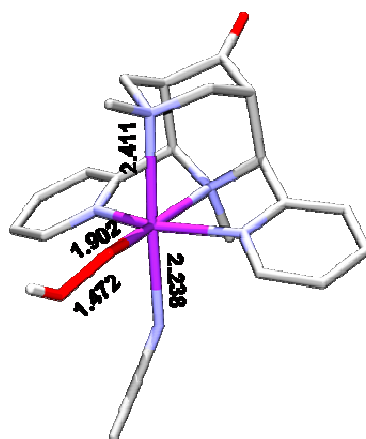
Formation of $[LFe^{II}(OOH)(CH_3CN)]^+$

Deprotonation of primary intermediate $[L^1Fe^{II}(HOOH)(CH_3CN)]^{2+}$ leads to the formation of an Fe^{II}-hydroperoxo intermediate. The geometry of $[L^1Fe^{II}(OOH)(CH_3CN)]^+$ was optimised in all possible spin states and an S=2 ground state is calculated, with relative energies of 48.7 and 65.9 kJ/mol for the S=1 and S=0 states respectively. The calculated geometry of the quintet ground state, including relevant bond lengths, is shown in Figure 4.15. Deprotonation of the bound hydrogen peroxide weakens the O–O bond slightly, which is reflected in the increase in bond length from 1.452 Å in $[L^1Fe^{II}(HOOH)(CH_3CN)]^{2+}$ to 1.472 Å in $[L^1Fe^{II}(OOH)(CH_3CN)]^+$, but has a drastic effect on the Fe–O bond, decreasing the bond length from 2.232 to 1.902 Å. The same tendency is observed in the Fe–O and O–O stretching frequencies. The O–O stretching frequency decreases from 911 cm⁻¹ to 895 cm⁻¹, while the Fe–O stretching frequency more than doubles, from 236 cm⁻¹ in primary intermediate $[L^1Fe^{II}(HOOH)(CH_3CN)]^{2+}$ to 505 cm⁻¹ in $[L^1Fe^{II}(OOH)(CH_3CN)]^+$. These results are summarised in Table 4.4, together with the geometries of $[L^1Fe^{II}(OOH)(H_2O)]^+$ and $[L^1Fe^{II}(OOH)]^+$.

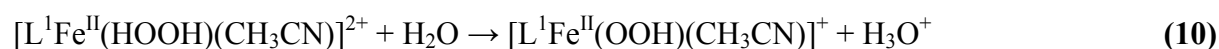
Table 4.4. Selected geometric parameters, O–O stretching frequencies and relative energies of the spin states in the Fe^{II}-hydroperoxo complexes of L¹

	Bond distances (Å)			ν (cm ⁻¹) O1-O2	ΔE (kJ/mol) 0°
	Fe-O1	Fe-O2	O1-O2		
[LFe^{II}(OOH)]⁺					
S=0	1.903	2.021	1.482	850	68.4
S=1	1.795	2.796	1.475	848	34.6
S=2	1.897	2.417	1.472	871	0.0
[LFe^{II}(CH₃CN)(OOH)]⁺					
S=0	1.896	2.849	1.483	860	65.9
S=1	1.815	2.853	1.478	826	48.7
S=2	1.902	2.777	1.472	894	0.0
[LFe^{II}(H₂O)(OOH)]⁺					
S=0	1.914	2.830	1.500	800	74.7
S=1*	1.636	2.303	2.130	-	46.3
S=2	1.916	2.815	1.479	855	0.0

*[LFe^{II}(H₂O)(OOH)]⁺ in the S=1 state converges to a structure best described as a [LFe^{III}(O)(OH₂)]⁺...OH species

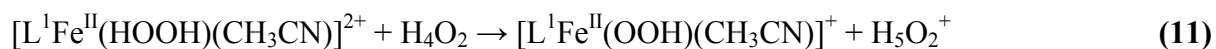
**Figure 4.15. Optimised geometry of [LFe^{II}(OOH)(CH₃CN)]²⁺ in its S=2 ground state**

Deprotonation of [L¹Fe^{II}(HOOH)(CH₃CN)]²⁺ by H₂O, to form [L¹Fe^{II}(OOH)(CH₃CN)]⁺ and H₃O⁺ (reaction **(10)**) has a highly unfavourable reaction energy of +123.2 kJ/mol:



However, this does not account for stabilisation of H₂O and H₃O⁺ by hydrogen bonding. If an additional water molecule is used to stabilise these species through hydrogen bonding

(reaction **(11)**), the energy of deprotonation of $[\text{L}^{\text{I}}\text{Fe}^{\text{II}}(\text{HOOH})(\text{CH}_3\text{CN})]^{2+}$ is lowered by almost 90 kJ/mol to +34.8 kJ/mol:



If a third water molecule is included to stabilise the released proton, the reaction even becomes slightly exothermic and further hydrogen bonding is likely to further decrease the energy. While these hydrogen bonding energies are only approximate (DFT methods are known not to give a good description of hydrogen bonding), they show that this reaction is feasible in the presence of water. The pKa values of the bispidine Fe^{II} -hydrogen peroxide complexes are not known, but a pKa of 7.6 has been experimentally determined for the $[\text{L}^{\text{I}}\text{Fe}^{\text{II}}(\text{H}_2\text{O})]^{2+}$. From this value and the known pKa values of H_2O (15.7) and H_2O_2 (11.7)^[45], the pKa value of $[\text{L}^{\text{I}}\text{Fe}^{\text{II}}(\text{HOOH})]^{2+}$ is estimated to be approximately 3.6. One expects the pKa of $[\text{L}^{\text{I}}\text{Fe}^{\text{II}}(\text{HOOH})(\text{CH}_3\text{CN})]^{2+}$ to lie in the same range, which implies easy deprotonation of the species even at pH values well below 7. This agrees with the exothermic reaction energy predicted in the presence of three or more water molecules and indicates that this would probably be the favoured reaction pathway in aqueous medium. However, given the low concentration of water present in the reaction mixture, this reaction is unlikely to take place under the catalytic reaction conditions.

Solvent abstraction and O-O bond cleavage

A significant result is that abstraction of the *trans* N7 coordinated acetonitrile molecule in $[\text{L}^{\text{I}}\text{Fe}^{\text{II}}(\text{OOH})(\text{CH}_3\text{CN})]^+$ is essentially thermoneutral, in contrast to the corresponding reactions in $[\text{L}^{\text{I}}\text{Fe}^{\text{II}}(\text{HOOH})(\text{CH}_3\text{CN})]^{2+}$ and $[\text{L}^{\text{I}}\text{Fe}^{\text{III}}(\text{OOH})(\text{CH}_3\text{CN})]^{2+}$. A quintet ground state is calculated for $[\text{L}^{\text{I}}\text{Fe}^{\text{II}}(\text{OOH})]^+$ and the triplet and singlet states have energies of 34.6 and 68.4 kJ/mol with respect to the ground state. Solvent abstraction to form $[\text{L}^{\text{I}}\text{Fe}^{\text{II}}(\text{OOH})]^+$ causes a further increase of the O–O bond length from 1.472 Å in $[\text{L}^{\text{I}}\text{Fe}^{\text{II}}(\text{OOH})(\text{CH}_3\text{CN})]^+$ to 1.484 Å in $[\text{L}^{\text{I}}\text{Fe}^{\text{II}}(\text{OOH})]^+$ and a decrease of the Fe–O bond length from 1.902 to 1.897 Å. Again this is reflected in the Fe–O and O–O stretching frequencies (see Table 4.4).

Homolytic cleavage of the O–O bond in $[L^I\text{Fe}^{II}(\text{OOH})]^+$ is both thermodynamically and kinetically the most favourable of all the direct O–O bond cleavage reactions studied, with a total reaction energy of -96.2 kJ/mol and an energy barrier of only 51.5 kJ/mol. As for $[L^I\text{Fe}^{IV}(\text{O})(\text{OH}_2)]^{2+}$, the product of this reaction, an $[L^I\text{Fe}^{IV}(\text{O})(\text{OH})]^+$ complex, has an $S=2$ ground state, with the $S=1$ spin state lying 21.0 kJ/mol higher in energy. The energies of this reaction and the structures and relative energies of the reactant, transition state and product, are shown in Figure 4.16. The geometry of the transition state is quite remarkable, with an Fe–O–O bond angle of 116.1° , around 25° larger than the corresponding angle in both the reactant and the product (90.5° and 91.6° respectively).

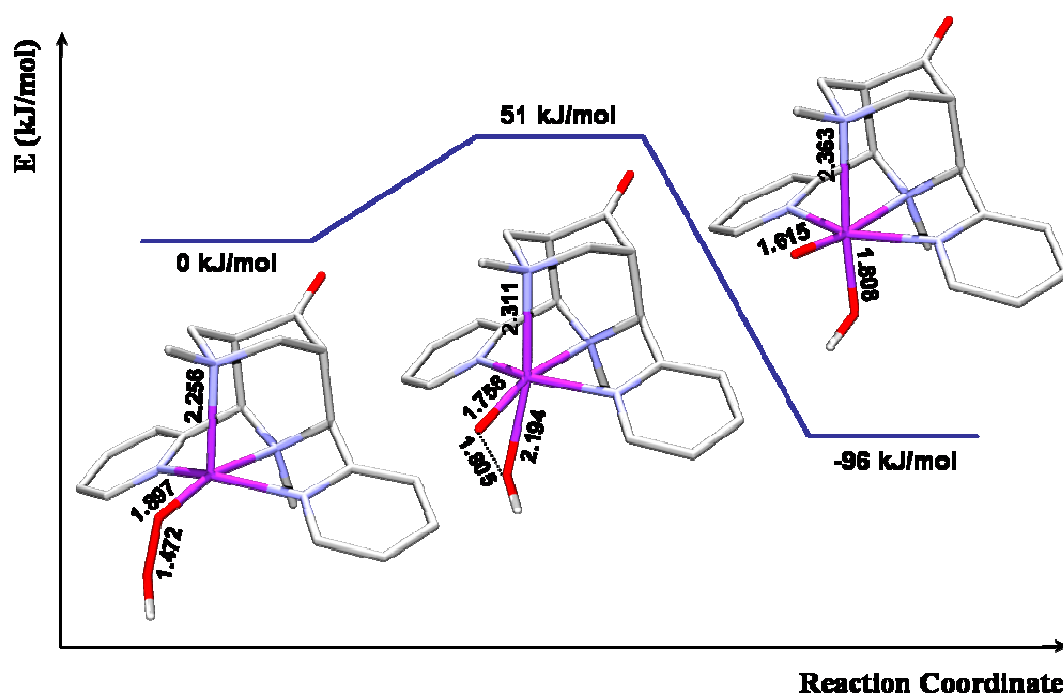


Figure 4.16. The $S=2$ reaction profile for heterolytic cleavage of the O–O bond in $[L^I\text{Fe}^{II}(\text{OOH})]^+$, showing the reactant, transition state and product

An important difference between this and the previous two mechanisms is that all intermediates along this pathway have an $S=2$ ground state and no forbidden spin-crossovers therefore have to occur. This fact, in addition to the thermoneutral solvent abstraction, the exothermic reaction energy and low energy barrier for O–O bond cleavage and the relatively few steps required, makes this pathway extremely favourable. The only real problem is the

deprotonation of $[L^1Fe^{II}(HOOH)(CH_3CN)]^{2+}$, which requires at least three water molecules to stabilise the released proton through hydrogen bonding and make the reaction feasible.

Formation of $[LFe^{IV}(O)(OH)]^+$ from $[LFe^{II}(OOH)(H_2O)]^+$

Analogous to the formation of $[L^1Fe^{IV}(OH)_2]^{2+}$ from $[L^1Fe^{II}(HOOH)(H_2O)]^{2+}$, the $[L^1Fe^{IV}(O)(OH)]^+$ complex can also be formed from $[L^1Fe^{II}(OOH)(H_2O)]^+$, as shown schematically in Figure 4.17.

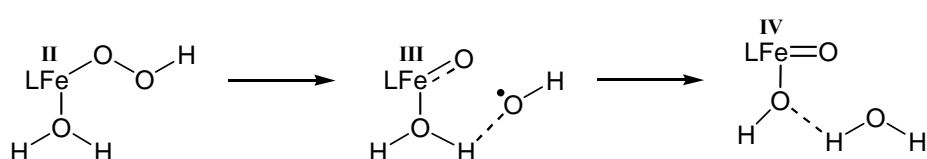


Figure 4.17. Schematic representation of the formation of $[L^1Fe^{IV}(O)(OH)]^+$ from $[L^1Fe^{II}(OOH)(H_2O)]^+$

As discussed previously, the abstraction of acetonitrile is thermoneutral and 12.1 kJ/mol are released upon coordination of a water molecule *trans* to N7. The formed $[L^1Fe^{II}(OOH)(H_2O)]^+$ complex also has an S=2 ground state, with relative energies of 46.3 and 74.7 kJ/mol for the S=1 and S=0 spin states respectively. The reaction pathway for the reaction of $[L^1Fe^{II}(OOH)(H_2O)]^+$ to $[L^1Fe^{IV}(O)(OH)]^+ \cdots OH_2$ on the quintet surface is shown in Figure 4.18 and relevant bond lengths and Mulliken spin densities are given in Table 4.5.

Table 4.5. Summary of the bond distances and Mulliken spin densities for the reaction of $[L^1Fe^{II}(OOH)(H_2O)]^+$ to $[L^1Fe^{IV}(O)(OH)]^+ \cdots OH_2$

Complex	Bond distance (Å)				Mulliken Spin Density		
	Fe-O1	O1-O2	Fe-O3	Fe	O1	O2	O3
$[LFe^{II}(OOH)(H_2O)]^{2+}$	1.916	1.479	2.269	3.77	0.11	0.01	0.02
TS1	1.743	1.837	2.191	3.93	0.26	-0.42	0.04
$[LFe^{III}(O)(H_2O)]^{2+}$	1.714	2.058	2.140	4.03	0.26	-0.57	0.06
TS2	1.721	2.076	2.080	4.06	0.15	-0.52	0.07
$[LFe^{IV}(O)(OH)]^{2+}$	1.614	3.001	1.845	3.20	0.50	0.01	0.14

4. Oxidation Catalysis with the Iron(II) Complex of a tetradentate 3,7-Diazabicyclo[3.3.1]nonane Derivative

The first step, O–O bond cleavage in $[\text{L}^1\text{Fe}^{\text{II}}(\text{H}_2\text{O})(\text{OOH})]^+$, has a relatively low energy barrier of 43.4 kJ/mol and is endothermic by 34.6 kJ/mol, compared to an energy barrier of 51.5 kJ/mol and a total reaction energy of –91.2 kJ/mol for O–O bond cleavage in $[\text{L}^1\text{Fe}^{\text{II}}(\text{OOH})]^+$. The reason for the relatively low energies, despite radical formation, is that the radical is immediately trapped and stabilised by hydrogen bonding with the *trans* N7 bound water molecule. The Fe^{III} oxidation state of the $[\text{L}^1\text{Fe}^{\text{III}}(\text{O})(\text{OH}_2)]^+\cdots\text{OH}$ intermediate is confirmed by the Mulliken spin density on the iron centre, which increases from 3.77 in $[\text{L}^1\text{Fe}^{\text{II}}(\text{H}_2\text{O})(\text{OOH})]^+$, to 4.03 in $[\text{L}^1\text{Fe}^{\text{III}}(\text{O})(\text{H}_2\text{O})]^+\cdots\text{OH}$, closer to the spin densities of 4.21 and 4.19 found on the Fe in $[\text{L}^1\text{Fe}^{\text{III}}(\text{OH})(\text{CH}_3\text{CN})]^{2+}$ and $[\text{L}^1\text{Fe}^{\text{III}}(\text{OOH})(\text{CH}_3\text{CN})]^{2+}$, than to that of the Fe^{II} reactant. The formation of the $\cdot\text{OH}$ radical can also be seen from the change in spin density on O2.

It is interesting to compare the spin densities on Fe and O2 in this transition state (TS1 in Table 4.5 and Figure 4.18) to the corresponding transition state in the reaction of $[\text{L}^1\text{Fe}^{\text{II}}(\text{H}_2\text{O})(\text{HOOH})]^{2+}$ to $[\text{L}^1\text{Fe}^{\text{III}}(\text{OH})(\text{H}_2\text{O})]^+\cdots\text{OH}$ (see Figure 4.11). In the transition state of O–O bond cleavage in $[\text{L}^1\text{Fe}^{\text{II}}(\text{H}_2\text{O})(\text{HOOH})]^{2+}$, the spin density on the Fe is decreased relative to the reactant and an α -electron is being removed from the O–O bond to form the $\cdot\text{OH}$ radical (the spin density on O2 is positive), which is indicative of a spin-crossover from an S=2 to an S=1 state. In contrast, the transition state for O–O bond cleavage in $[\text{L}^1\text{Fe}^{\text{II}}(\text{H}_2\text{O})(\text{OOH})]^+$ shows an increase in spin density on Fe relative to the reactant and a β -electron is being removed from the O–O bond to form the $\cdot\text{OH}$ radical (the spin density on O2 is negative), indicating that no spin-crossover takes place.

The $[\text{L}^1\text{Fe}^{\text{III}}(\text{O})(\text{H}_2\text{O})]^+\cdots\text{OH}$ intermediate is unstable and reacts further to form $[\text{L}^1\text{Fe}^{\text{IV}}(\text{O})(\text{OH})]^+\cdots\text{OH}_2$, a reaction which releases 83.4 kJ/mol. However, the transition state for this reaction (TS2) is calculated to have an energy of 30.6 kJ/mol relative to the reactant, which is lower than the energy of the $[\text{L}^1\text{Fe}^{\text{III}}(\text{O})(\text{OH}_2)]^+\cdots\text{OH}$ intermediate. A comparison of the geometries reveals that TS2 is out of place in the general trend in the bond lengths along the reaction coordinate. For example, the Fe–O1 bond lengths decrease steadily from $[\text{L}^1\text{Fe}^{\text{II}}(\text{H}_2\text{O})(\text{OOH})]^+$ to $[\text{L}^1\text{Fe}^{\text{IV}}(\text{O})(\text{OH})]^+\cdots\text{OH}_2$, with the exception of TS2, in which the

Fe–O bond is slightly longer than in the Fe^{III} intermediate. This is merely an indication of the shallowness of the PES in this region however, rather than a significant error.

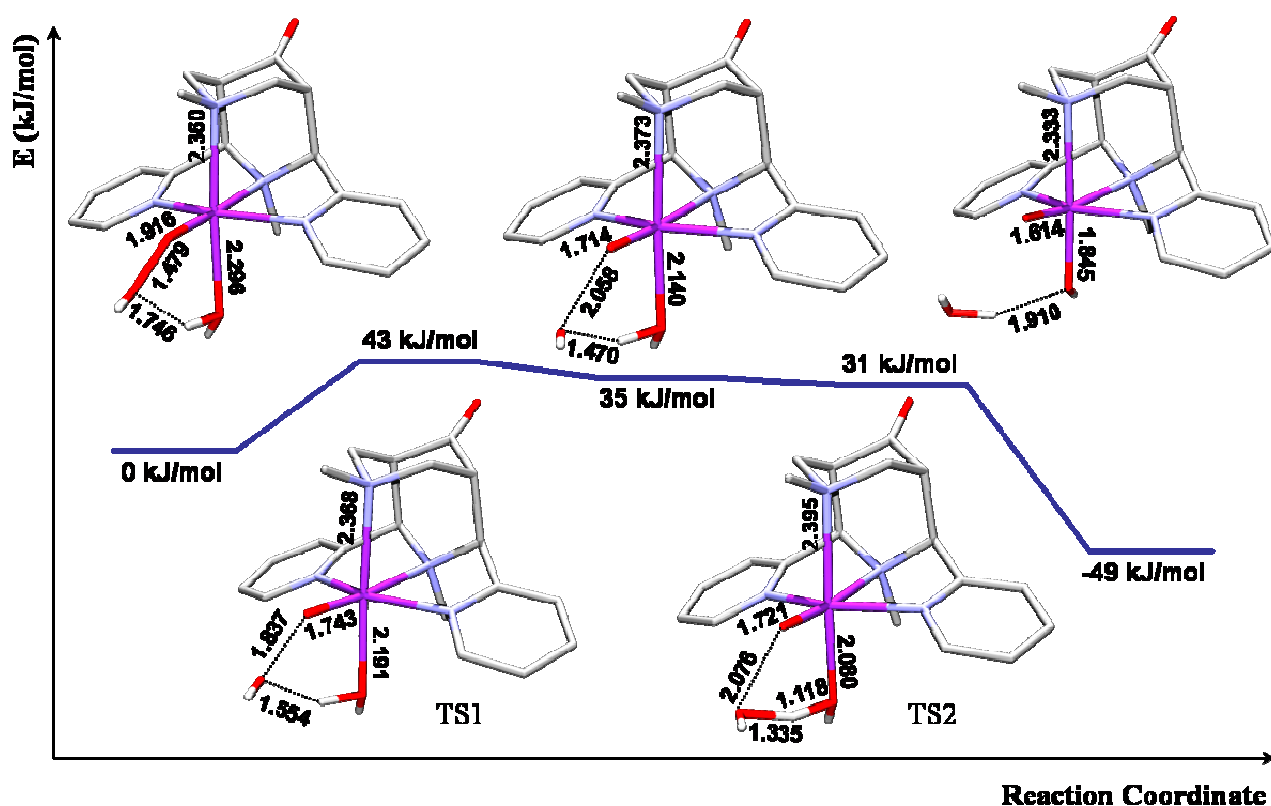


Figure 4.18. The S=2 reaction profile for homolytic cleavage of the O–O bond in $[L^1Fe^{II}(OOH)(H_2O)]^+$, showing the reactant, transition states, intermediate and product

The total energy of this reaction is -49 kJ/mol, which is much lower than the reaction energy of the direct O–O bond cleavage in $[L^1Fe^{II}(OOH)]^+$ (-91.2 kJ/mol). This is partially due to the energy released upon formation of $[L^1Fe^{II}(H_2O)(OOH)]^+$ from $[L^1Fe^{II}(OOH)]^+$ and H_2O , but also due to the fact that the $[L^1Fe^{IV}(O)(OH)]^+\cdots OH_2$ product is 35.4 kJ/mol higher in energy than $[L^1Fe^{IV}(O)(OH)]^+$ and H_2O . A comparison of the geometries of $[L^1Fe^{IV}(O)(OH)]^+$ and $[L^1Fe^{IV}(O)(OH)]^+\cdots OH_2$ (see Figures 4.16 and 4.18), reveals that the Fe–O3 bond length (where O3 is oxygen atom from the *trans* N7 bound H_2O) is significantly longer in the hydrogen bonded complex and that the O3 bound proton is rotated by around 180° from the ground state geometry of $[L^1Fe^{IV}(O)(OH)]^+$.

4.4. Conclusion

Three possible mechanisms (pathways **A**, **B** and **C** of Figure 4.4) have been investigated for the reaction of the Fe^{II} complex of the tetradentate bispidine ligand L¹ with H₂O₂, and these are summarised in Figure 4.19. For pathway **A** the reaction energy for the mononuclear formation of [L¹Fe^{III}(OH)]²⁺ is used and for pathway **C** stabilising hydrogen bonding interactions are not taken into account the reaction energy for the deprotonation step (for reasons outlined in Sections 4.3.3 and 4.3.5 respectively).

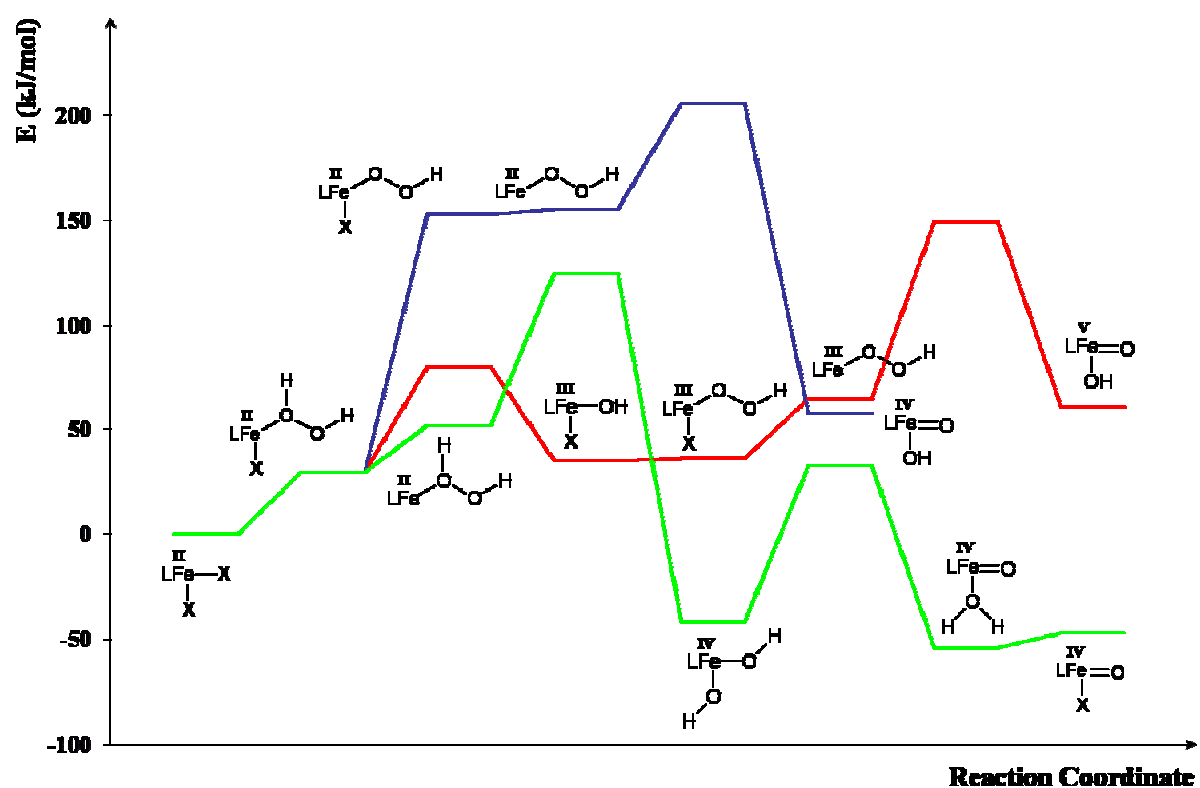


Figure 4.19. Summary of the three studied mechanisms (water-assisted pathways excluded), red – pathway A, green – pathway B, blue – pathway C of Figure 4.4

Under these conditions (low concentration of the catalyst and water) the thermodynamically most favourable pathway is **B**. The first step in the mechanistic cycle is therefore proposed to be the formation of primary intermediate [L¹Fe^{II}(HOOH)(CH₃CN)]²⁺. Due to the dissociative nature of Fe^{II} ligand exchange reactions and the weak binding of the *trans* N7 coordinated solvent molecule, a short-lived pentacoordinate [L¹Fe^{II}(HOOH)]²⁺ intermediate is formed in

the process of ligand exchange *trans* to N7. This intermediate then undergoes homolytic cleavage of the O–O bond to form $[\text{L}^1\text{Fe}^{\text{IV}}(\text{OH})_2]^{2+}$. This species may react directly with the double bond of the substrate, to form the diol, a proposal which is supported by the experimental observation that both oxygen atoms in the diol originate from H_2O_2 .

It is important to note that the $[\text{LFe}^{\text{IV}}(\text{OH})_2]^{2+}$ intermediate essential to our mechanistic proposal cannot be formed when L is a pentadentate ligand, due to the absence of the second coordination site. The analogous reaction for a pentadentate ligand, would lead to the formation of an $[\text{LFe}^{\text{III}}(\text{OH})]^{2+}$ intermediate, the first step in the formation of $[\text{LFe}^{\text{III}}(\text{OOH})]^{2+}$ intermediates indeed observed for L^6 and L^7 . We propose this open coordination site to be the crucial element leading to the differences in product distribution observed between the L^1 and L^7 systems. However, Fe^{III} -hydroxo and Fe^{III} -hydroperoxo intermediates have also been observed for tetradentate ligands such as TPA. The deciding difference between L^1 and other tetradentate systems may be the weak *trans* N7 ligand binding in the L^1 system, induced by the demands of the rigid ligands backbone, since relatively facile removal of the *trans* N7 coordinated solvent molecule is an important requirement in the formation of $[\text{LFe}^{\text{IV}}(\text{OH})_2]^{2+}$.

Proton transfer from the *trans* N3 to the *trans* N7 bound hydroxide in $[\text{L}^1\text{Fe}^{\text{IV}}(\text{OH})_2]^{2+}$ leads to the formation of a high-valent $[\text{L}^1\text{Fe}^{\text{IV}}(\text{O})(\text{H}_2\text{O})]^{2+}$ intermediate, which may undergo ligand exchange to form $[\text{L}^1\text{Fe}^{\text{IV}}(\text{O})(\text{CH}_3\text{CN})]^{2+}$. Either of these species may be responsible for the formation of epoxide, by addition to the double bond of the substrate, analogous to the formation of epoxide in the L^7 system. This may explain the higher diol/epoxide ratio for L^1 , since the formation of the diol is a competing reaction to the formation of the $\text{Fe}^{\text{IV}}=\text{O}$ species which forms the epoxide. This is in contrast to L^7 , where the diol and epoxide are proposed to be formed from a common $\text{Fe}^{\text{IV}}=\text{O}$ intermediate, but there are two possible routes for epoxide formation and only one for diol formation.

4.5. References

- ¹ A.L. Feig, S.J. Lippard, *Chem. Rev.*, **1994**, 94, 759
- ² L. Que, Jr., R.Y.N. Ho, *Chem. Rev.*, **1996**, 96, 2607
- ³ E.I. Solomon, T.C. Brunold, M.I. Davis, J.N. Kemsley, S. Lee, N. Lehnert, F. Neese, A.J. Skulan, Y. Yang, J. Zhou, *Chem. Rev.* **2000**, 100, 235
- ⁴ E. Skrzypczak-Jankun, R.A. Bross, R.T. Carroll, W.R. Dunham, M.O. Funk, Jr., *J. Am. Chem. Soc.*, **2001**, 123, 10814
- ⁵ T.E. Westre, K.E. Loeb, J.M. Zaleski, B. Hedman, K.O. Hodgson and E.I. Solomon, *J. Am. Chem. Soc.*, **1995**, 117, 1309
- ⁶ F. Neese, J.M. Zaleski, K. Loeb Zaleski and E.I. Solomon, *J. Am. Chem. Soc.*, **2000**, 122, 11703
- ⁷ J.C. Price, E.W. Barr, B. Tirupati, M. Bollinger Jr., C. Krebs, *Biochemistry*, **2003**, 42, 7497
- ⁸ D.L. Harris, G.H. Loew, *J. Am. Chem. Soc.*, **1998**, 120, 8941
- ⁹ E.I. Solomon, T.C. Brunold, M.I. Davis, J.N. Kemsley, S. Lee, N. Lehnert, F. Neese, A.J. Skulan, Y. Yang, J. Zhou, *Chem. Rev.* **2000**, 100, 235
- ¹⁰ B. Meunier, S.P. de Visser and S. Shaik, *Chem. Rev.*, **2004**, 104, 3947
- ¹¹ L. Que Jr., *J. Chem. Soc. Dalton Trans.*, **1997**, 21, 3933
- ¹² Y. Dong, Y. Zang, K. Kauffmann, L. Shu, E.C. Wilkinson, E. Muenck, L. Que Jr., *J. Am. Chem. Soc.*, **1997**, 119, 12683
- ¹³ H-F. Hsu, Y. Dong, L. Shu, V.G. Young, L. Que Jr., *J. Am. Chem. Soc.*, **1999**, 121, 5230
- ¹⁴ V.L. MacMurdo, H. Zheng, L. Que Jr., *Inorg. Chem.*, **2000**, 39, 2254
- ¹⁵ K. Chen, L. Que Jr., *Angew. Chem., Int. Ed.*, **1999**, 38, 2227
- ¹⁶ M. Costas, A.K. Tipton, K. Chen, D-H. Jo and L. Que Jr., *J. Am. Chem. Soc.*, **2001**, 123, 6722
- ¹⁷ K. Chen, M. Costas, J. Kim, A. Tipton and L. Que Jr., *J. Am. Chem. Soc.*, **2002**, 124, 3026
- ¹⁸ K. Chen, M. Costas, L. Que Jr., *J. Chem. Soc., Dalton Trans.*, **2002**, 672
- ¹⁹ J.Y. Ryu, J. Kim, M. Costas, K. Chen, W. Nam, L. Que Jr., *Chem. Comm.*, **2002**, 12 1288
- ²⁰ M.R. Bukowski, P. Comba, A. Lienke, C. Limberg, C. Lopez de Laorden, R. Mas-Balleste, M. Merz, L. Que Jr., *Angew. Chem.*, *accepted*
- ²¹ H. Börzel, P. Comba, K.S. Hagen, Y.D. Lampeka, A. Lienke, G. Linti, M. Merz, H. Pritzkow, L.V. Tsymbal, *Inorg. Chim. Acta*, **2002**, 337, 407
- ²² M.R. Bukowski, P. Comba, C. Limberg, M. Merz, L. Que Jr., *Angew. Chem. Int. Ed.*, **2004**, 43, 1283

- ²³ J. Bautz, M.R. Bukowski, A. Stubna, M. Kerscher, A. Lienke, P. Comba, E. Münck and L. Que Jr., *Angew. Chem.*, *submitted*
- ²⁴ Jochen Bautz, *PhD Thesis*, Ruprecht-Karls Universität Heidelberg, **2006**
- ²⁵ Carlos Lopez de Laorden, *PhD Thesis*, Ruprecht-Karls Universität Heidelberg, **2006**
- ²⁶ K. Chen, L. Que, Jr., *J. Am. Chem. Soc.*, **2001**, 123, 6327
- ²⁷ J. Bautz, P. Comba, L. Que Jr., *Inorg. Chem.*, *submitted*
- ²⁸ W.C. Bray, M.H. Gorin, *J. Am. Chem. Soc.*, **1932**, 54, 2124
- ²⁹ F. Haber, J. Weiss, *Proc. R. Soc. London*, **1934**, A147, 332; W.G. Barb, J.H. Baxendale, P. George, K.R. Hargrave, *Trans. Faraday Soc.*, **1951**, 47, 462
- ³⁰ F. Buda, B. Ensing, M.C.M. Gribnau, E.J. Baerends, *Chem. Eur. J.*, **2001**, 7, 2775
- ³¹ F. Buda, B. Ensing, E.J. Baerends, *J. Phys. Chem. A*, **2003**, 107, 5722; F. Buda, B. Ensing, M.C.M. Gribnau, E.J. Baerends, *Chem. Eur. J.*, **2003**, 9, 3436
- ³² M.L. Kremer, *Phys. Chem. Chem. Phys.*, **1999**, 1, 3595
- ³³ *Gaussian 03, Revision B.03*, M. J. Frisch, G. W. Trucks, H. B. Schlegel, G. E. Scuseria, M. A. Robb, J. R. Cheeseman, J. A. Montgomery, Jr., T. Vreven, K. N. Kudin, J. C. Burant, J. M. Millam, S. S. Iyengar, J. Tomasi, V. Barone, B. Mennucci, M. Cossi, G. Scalmani, N. Rega, G. A. Petersson, H. Nakatsuji, M. Hada, M. Ehara, K. Toyota, R. Fukuda, J. Hasegawa, M. Ishida, T. Nakajima, Y. Honda, O. Kitao, H. Nakai, M. Klene, X. Li, J. E. Knox, H. P. Hratchian, J. B. Cross, C. Adamo, J. Jaramillo, R. Gomperts, R. E. Stratmann, O. Yazyev, A. J. Austin, R. Cammi, C. Pomelli, J. W. Ochterski, P. Y. Ayala, K. Morokuma, G. A. Voth, P. Salvador, J. J. Dannenberg, V. G. Zakrzewski, S. Dapprich, A. D. Daniels, M. C. Strain, O. Farkas, D. K. Malick, A. D. Rabuck, K. Raghavachari, J. B. Foresman, J. V. Ortiz, Q. Cui, A. G. Baboul, S. Clifford, J. Cioslowski, B. B. Stefanov, G. Liu, A. Liashenko, P. Piskorz, I. Komaromi, R. L. Martin, D. J. Fox, T. Keith, M. A. Al-Laham, C. Y. Peng, A. Nanayakkara, M. Challacombe, P. M. W. Gill, B. Johnson, W. Chen, M. W. Wong, C. Gonzalez, and J. A. Pople, *Gaussian, Inc., Pittsburgh PA, 2003*
- ³⁴ A.D.J. Becke, *J. Chem. Phys. B*, **1993**, 98, 5648; C. Lee, W. Yang, R.G. Parr, *Phys. Rev. B*, **1988**, 37, 785
- ³⁵ M.T. Cancès, B. Mennucci and J. Tomasi, *J. Chem. Phys.*, **1997**, 107, 3032; M. Cossi, V. Barone, B. Mennucci and J. Tomasi, *Chem. Phys. Lett.*, **1998**, 286, 253; B. Mennucci and J. Tomasi, *J. Chem. Phys.*, **1997**, 106, 5151; M. Cossi, G. Scalmani, N. Rega and V. Barone, *J. Chem. Phys.*, **2002**, 117, 43
- ³⁶ A. Schäfer, C. Huber and R. Ahlrichs, *J. Chem. Phys.*, **1994**, 100, 5829

- ³⁷ *GaussView, Version 3.09*, R. Dennington II, T. Keith, J. Millam, K. Eppinnett, W.L. Hovell, and R. Gilliland, Semichem, Inc., Shawnee Mission, KS, **2003**
- ³⁸ W.C. Oelfke, W. Gordy, *J. Chem. Phys.*, **1969**, 51, 5336
- ³⁹ W.G. Solomons, *Organic Chemistry*, Wiley, New York, **1992**
- ⁴⁰ Y. Ducommun, K.E. Newman and A.E. Mehrbach, *Inorg. Chem.*, **1980**, 19, 3696; R. van Eldik, *Studies in Inorganic Chemistry 7: Inorganic High Pressure Chemistry*, Elsevier, **1986**
- ⁴¹ G. Roelfes, M. Lubben, K. Chen, R.Y.N. Ho, A. Meetsma, S. Genseberger, R.M. Hermant, R. Hage, S.K. Mandal, V.G. Young, Jr., Y. Zang, H. Kooijman, A.L. Spek, L. Que, Jr. and B. Feringa, *Inorg. Chem.*, **1999**, 38, 1929
- ⁴² A. Bassan, M.R.A. Blomberg, P.E.M. Siegbahn, L. Que, Jr., *J. Am. Chem. Soc.*, **2002**, 124, 11056
- ⁴³ S. Shaik, M. Filatov, D. Schröder, H. Schwarz, *Chem. Eur. J.*, **1998**, 4, 193
- ⁴⁴ A. Bassan, M.R.A. Blomberg, P.E.M. Siegbahn, L. Que, Jr., *Chem. Eur. J.*, **2005**, 11, 692
- ⁴⁵ D.A. Vander Griend, J.S. Golden, C.A. Arrington, Jr., *Inorg. Chem.*, **2002**, 41, 7042

5. The Electronic Structure of the Oxoiron(IV) Complexes of tetra- and pentadentate 3,7-Diazabicyclo[3.3.1]nonane Derivatives

5.1. Introduction

Oxoiron(IV) intermediates are invoked as the key active species in a number of oxygenation reactions^[1], both enzymatic and synthetic^[2], and the number of reported $\text{Fe}^{\text{IV}}=\text{O}$ complexes in the literature has increased immensely in recent years^[3,4]. Commonly cited examples of $\text{Fe}^{\text{IV}}=\text{O}$ species in enzymes are the mononuclear heme cytochrome P450 enzymes^[5,6], intermediate Q in methane monooxygenase (MMO)^[7,8] and the mononuclear nonheme taurine/ α -ketoglutarate dioxygenase (TauD) enzyme^[9]. The cytochrome P450 enzymes effect the hydroxylation of alkanes and arenes by means of an $\text{Fe}^{\text{IV}}=\text{O}$ moiety in conjunction with a porphyrin radical. Intermediate Q of MMO, which oxidises methane to methanol, features an $[\text{Fe}^{\text{IV}}_2\text{O}_2]$ diamond core with antiferromagnetically coupled local high-spin iron(IV) centres. Hydroxylation of inactivated carbon atoms in a variety of substrates by TauD is also effected by an $\text{Fe}^{\text{IV}}=\text{O}$ species in a mechanism believed to be similar to that of cytochrome P450. TauD was the first example of the trapping of a mononuclear, nonheme oxoiron(IV) intermediate and was characterised by Mössbauer and EPR studies to be high-spin^[10,11,12]. An $\text{Fe}^{\text{IV}}=\text{O}$ intermediate has also been postulated to play an important role in the activity of the antimalarial drug artemisinin^[13].

A number of iron complexes have been synthesised as model systems, in order to study the reaction mechanisms of these enzymes^[14]. In the specific field of mononuclear non-heme iron chemistry, iron complexes of selected tetra- and pentadentate 3,7-diazabicyclo[3.3.1]nonane bispidine ligands have been synthesised and characterised^[15]. However, given that high oxidation states favour strong basic ligands and that these in turn favour low spin states of the coordinated metal centre, the $\text{Fe}^{\text{IV}}=\text{O}$ complexes of synthetic ligands usually have low-spin ($S=1$) ground states.

Recently, the first crystal structure of an $\text{Fe}^{\text{IV}}=\text{O}$ complex was reported, with the macrocyclic ligand TMC (1,4,8,11-tetramethyl-1,4,8,11-tetraazacyclotetradecane)^[16,17]. This species is characterised by an absorption maximum wavelength at 820 nm, and has an $S=1$ ground state (characterised by Mössbauer spectral simulations). Subsequent to this, a second crystal structure of an $\text{Fe}^{\text{IV}}=\text{O}$ complex could be isolated with the pentadentate ligand N4py^[18] (see Figure 4.2) and was also shown to have an $S=1$ ground state. The Fe–O distances in these two structures are 1.646(3) and 1.639(5) Å respectively, similar to each other and comparable to the Fe–O distances deduced from EXAFS studies of oxoiron(IV) units in synthetic porphyrin (1.65/1.66 Å)^[19] and heme peroxidase compounds (1.60-1.69 Å)^[20,21]. For comparison, the terminal Fe–O distance in the only characterised $\text{Fe}^{\text{III}}=\text{O}$ complex is 1.813(3) Å^[22].

In the same study a further $\text{Fe}^{\text{IV}}=\text{O}$ complex with the ligand Bn-TPEN (see Figure 4.2) was spectroscopically characterised and an Fe–O bond length of 1.67 Å deduced by EXAFS. The relative stabilities of the three possible isomers of $[\text{Fe}^{\text{IV}}(\text{O})(\text{Bn-TPEN})]^{2+}$ were investigated by means of NMR and DFT calculations and a correlation was found between the stability of the complex and the number of pyridine rings aligned parallel to the Fe–O axis. This was rationalised by the observation that the pyridine rings aligned parallel to the Fe–O axis have shorter Fe–Npy bond lengths than those which lie perpendicular to the Fe–O axis, allowing for greater stabilisation of the high-valent iron centre via electron donation.

Despite the growing number of reported low spin $\text{Fe}^{\text{IV}}=\text{O}$ complexes, the only structurally characterised synthetic high-spin Fe^{IV} complex remains the Collins complex, a distorted square pyramidal complex with a macrocyclic κ^4 -nitrogen ligand and a chloride ligand in the axial site, which has been assigned as a high-spin Fe^{IV} species on the basis of Mössbauer and EPR spectroscopy^[23,24]. A more recent study on the electronic structure of high-spin Fe^{IV} complexes^[25] attempts to quantify the relative energies of the $S=1$ and $S=2$ spin states in such complexes, using the Collins complex for “calibration”. The triplet-quintet splitting obtained with CCSD(T) and B3LYP were found to be essentially the same, indicating the suitability of DFT (and B3LYP in particular) for calculating the relative energies of the triplet and quintet states in Fe^{IV} complexes.

The iron(II) complexes of selected tetra- and pentadentate bispidine ligands are among the most active catalysts known in the epoxidation and dihydroxylation of alkenes in the presence of H_2O_2 , comparable in activity to the N4py and TPA complexes^[26]. Recently the $\text{Fe}^{\text{IV}}=\text{O}$ complex of the pentadentate ligand L^6 was formed in aqueous solution and spectroscopically characterised to have an $\text{S}=1$ ground state^[27]. However, as of yet, no $\text{Fe}^{\text{IV}}=\text{O}$ species have been observed for the tetradentate bispidines and no crystal structures have been obtained for those of the pentadentate ligands. For this reason a DFT study of the $\text{Fe}^{\text{IV}}=\text{O}$ complexes of the pentadentate bispidine ligands L^6 and L^7 and the tetradentate ligands L^1 and L^2 was initiated.

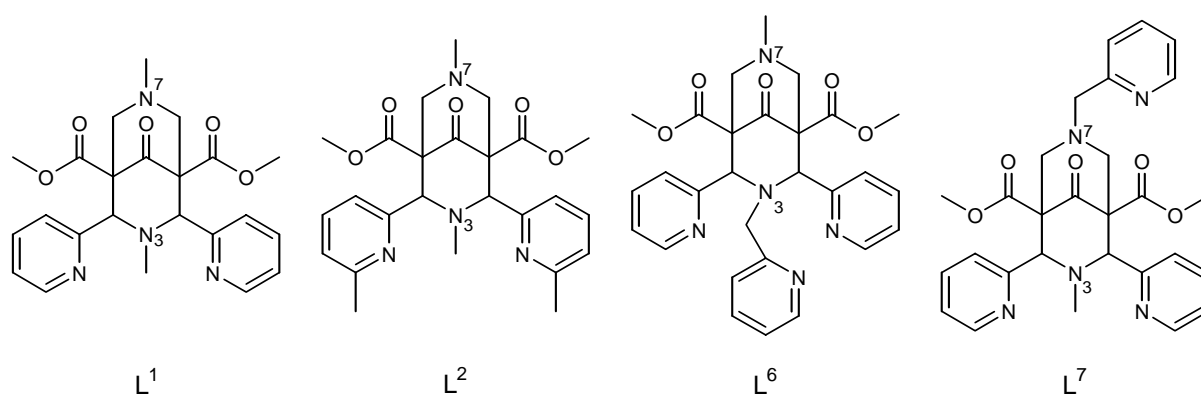


Figure 5.1. The four bispidine-type ligands investigated

The results of the calculations indicate that the $\text{Fe}^{\text{IV}}=\text{O}$ species of the tetradentate bispidine ligands L^1 and L^2 are likely to have $\text{S}=2$ ground states, in contrast to the $\text{S}=1$ states found for the pentadentate bispidines and other model systems, making them interesting potential candidates for enzyme mimics.

5.2. Computational Methods

Calculations were performed with Gaussian03^[28] using spin-unrestricted DFT methods. For the Fe^{IV}=O complexes of L¹, all structures were fully optimised in the gas phase with both the BPW91 and B3LYP^[29] functionals using a 6-31G(d) basis set. Calculations on the complexes of ligands L², L⁶ and L⁷ were performed only with the B3LYP functional, after this was shown for L¹ to give the most reliable results (see Section 5.3). Frequency calculations and SP energy calculations were performed on the B3LYP optimised geometries. For the SP energy calculations, Ahlrichs TZVPP^[30] basis set was used and solvation effects were added, using the PCM^[31] with acetonitrile as solvent. The zero-point energy corrections obtained from the frequency calculations were added to the TZVPP energies to obtain the final energies.

Table 5.1. Bond lengths, stretching frequencies, Mulliken spin densities and relative energies of the Fe^{IV}=O complexes of L¹, L², L⁶, L⁷

Compound	S	Bond distances (Å)					v(Fe-O) (cm ⁻¹)	Mulliken spin densities					E _{rel} (kJ/mol)	
		Fe-O	Fe-N7	Fe-N3	Fe-Npy	Fe-X		O	N7	N3	Npy	X		
[L ¹ Fe(O)] ²⁺	0	1.560	2.035	2.123	1.978	-	1004	0.00	0.00	0.00	0.00	0.00	-	110.7
[L ¹ Fe(O)] ²⁺	1	1.579	2.040	2.030	2.000	-	989	1.62	0.47	-0.02	-0.02	-	-	25.0
[L ¹ Fe(O)] ²⁺	2	1.614	2.184	2.056	2.002	-	943	3.11	0.70	0.12	-0.03	0.00	-	0.0
[L ¹ Fe(O)(CH ₃ CN)] ²⁺	1	1.621	2.148	2.105	1.987	1.980	913	1.22	0.86	-0.02	-0.02	-0.01	0.00	0.5
[L ¹ Fe(O)(CH ₃ CN)] ²⁺	2	1.613	2.321	2.097	2.036	2.302	943	3.13	0.68	0.09	-0.04	0.02	0.04	0.0
[L ¹ Fe(O)(OH ₂)] ²⁺	1	1.617	2.099	2.100	1.987	2.069	934	1.28	0.80	-0.04	-0.02	-0.01	-0.01	14.2
[L ¹ Fe(O)(OH ₂)] ²⁺	2	1.615	2.281	2.082	2.030	2.335	943	3.15	0.67	0.11	-0.04	0.01	0.02	0.0
[L ¹ Fe(O)(OH)] ⁺	1	1.615	2.295	2.133	1.983	1.849	950	1.44	0.66	0.00	-0.01	-0.01	-0.08	21.0
[L ¹ Fe(O)(OH)] ⁺	2	1.615	2.363	2.200	2.202	1.808	953	3.22	0.50	0.01	-0.01	0.06	0.13	0.0
[L ² Fe(O)] ²⁺ , <i>trans</i> N3	0	1.560	2.048	2.110	2.017	-	992	0.00	0.00	0.00	0.00	0.00	-	110.4
[L ² Fe(O)] ²⁺ , <i>trans</i> N3	2	1.613	2.179	2.047	2.054	-	942	3.11	0.72	0.10	-0.04	0.01	-	0.0
[L ² Fe(O)] ²⁺ , <i>trans</i> N7	0	1.565	2.284	1.941	1.976	-	983	0.00	0.00	0.00	0.00	0.00	-	127.6
[L ² Fe(O)] ²⁺ , <i>trans</i> N7	1	1.579	2.146	1.952	2.022	-	981	1.59	0.50	-0.01	-0.05	-0.02	-	26.5
[L ² Fe(O)] ²⁺ , <i>trans</i> N7	2	1.616	2.168	2.129	2.042	-	918	3.15	0.70	-0.02	0.15	-0.01	-	37.3
[L ² Fe(O)(CH ₃ CN)] ²⁺	1	1.618	2.156	2.097	2.049	1.978	919	1.18	0.88	-0.02	-0.02	-0.01	0.00	9.7
[L ² Fe(O)(CH ₃ CN)] ²⁺	2	1.611	2.291	2.089	2.114	2.282	944	3.13	0.68	0.08	-0.04	0.03	0.04	0.0
[L ⁶ Fe(O)] ²⁺	1	1.618	2.152	2.078	1.991	1.981	937	1.28	0.79	-0.01	-0.02	-0.01	-0.02	0.0
[L ⁶ Fe(O)] ²⁺	2	1.610	2.256	2.101	2.121	2.093	960	3.16	0.60	0.05	-0.03	0.05	0.05	19.8
[L ⁷ Fe(O)] ²⁺	1	1.616	2.239	2.009	2.006	1.990	936	1.27	0.81	-0.02	-0.02	-0.01	-0.01	12.8
[L ⁷ Fe(O)] ²⁺	2	1.609	2.223	2.200	2.155	2.064	951	3.17	0.60	-0.03	0.07	0.06	0.03	28.6

5.3. Results and Discussion

$Fe^{IV}=O$ complexes of L^1

For the tetradentate ligand L^1 , the geometries of the $Fe^{IV}=O$ complexes were calculated with the oxo ligand coordinated *trans* to N3 (see Figure 5.2). Geometries and energies have been calculated for complexes where the second potential coordination site *trans* to N7 is either vacant or occupied by ^-OH , H_2O or CH_3CN . The analogous structures where the oxo ligand is coordinated *trans* to N7 have not been optimised as the coordination site *trans* to N3 has been shown, both experimentally and computationally^[32], to be the favoured site for coordination in complexes of L^1 .

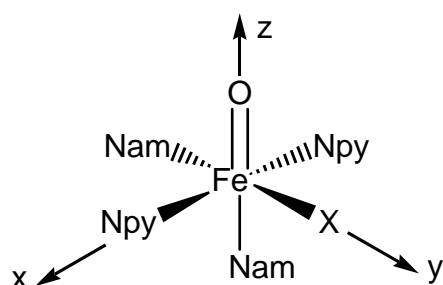


Figure 5.2. Coordination geometry of the bispidine $Fe^{IV}=O$ complexes; Nam=N3/N7, X= CH_3CN , H_2O , ^-OH , a vacant site (L^1 complexes) or pyridine (L^6 and L^7 complexes)

For all four complexes of L^1 described above, the ground state is calculated by B3LYP to be high-spin ($S=2$), although in the case of acetonitrile, the energy difference between the $S=1$ and $S=2$ states is so small that no definite conclusion can be made as to the ground spin state. In contrast, the BPW91 optimisations predict the $S=1$ state to be more stable than $S=2$ by 9, 44, 15 and 11 kJ/mol for $[L^1Fe^{IV}(O)]^{2+}$ and $[L^1Fe^{IV}(O)(X)]^{n+}$, with X= CH_3CN , H_2O ($n=2$) and ^-OH ($n=1$), respectively (note that frequency calculations were not performed on the BPW91 optimised geometries and zero-point energy corrections are therefore not included in these energies). However, the BPW91 functional is a pure DFT functional, and these are known to favour low-spin states. We believe the ground spin states predicted by B3LYP to be correct and not merely an artefact of the functional for a number of reasons: (i) the B3LYP functional

predicts $S=1$ ground states for the $\text{Fe}^{\text{IV}}=\text{O}$ species of the pentadentate ligands L^6 and L^7 , a results which is experimentally verified by their electronic absorption and Mössbauer spectra; (ii) for $[\text{L}^1\text{Fe}^{\text{II}}(\text{CH}_3\text{CN})_2]^{2+}$ the BPW91 functional predicts a low-spin state (by almost 100 kJ/mol), in contrast to experiment, while the B3LYP functional correctly predicts a high-spin state (see Section 4.3.1); (iii) it has been shown that the B3LYP functional is able to predict the correct spin states in Fe^{III} systems^[33]; and (iv) the energetics calculated with B3LYP for other $\text{Fe}^{\text{IV}}=\text{O}$ systems have been shown to be in good agreement with those calculated by CCSD(T) and, if anything, slightly biased towards low-spin states^[25].

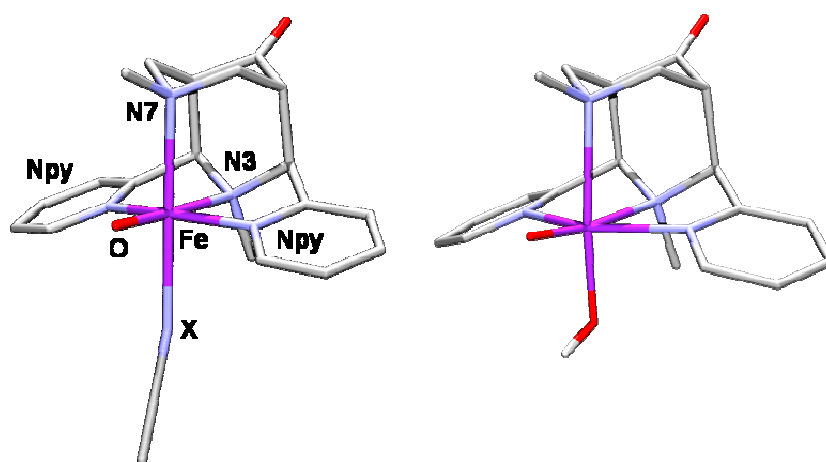


Figure 5.3. Optimised geometries of the $S=2$ ground states of $[\text{L}^1\text{Fe}^{\text{IV}}(\text{O})(\text{CH}_3\text{CN})]^{2+}$ and $[\text{L}^1\text{Fe}^{\text{IV}}(\text{O})(\text{OH})]^+$

Selected bond distances, Mulliken spin populations and relative energies of all the optimised complexes are given in Table 5.1 and the optimised geometries of $[\text{L}^1\text{Fe}^{\text{IV}}(\text{O})(\text{CH}_3\text{CN})]^{2+}$ and $[\text{L}^1\text{Fe}^{\text{IV}}(\text{O})(\text{OH})]^+$ are shown in Figure 5.3. At between 1.58 and 1.62 Å (for the $S=1$ and $S=2$ spin states), the Fe–O bond lengths are significantly shorter than known Fe–O bond lengths in terminal $\text{Fe}^{\text{IV}}=\text{O}$ complexes, but we believe this to be largely due to the choice of functional. The Fe–O bond lengths calculated by the BPW91 functional are, on average, around 0.02 Å longer (between 1.60 and 1.64 Å) than the B3LYP calculated bond lengths, placing them within the range of other calculated and experimental bond lengths, although still slightly on the short side. It is likely that the Fe–O bond lengths in the bispidine $\text{Fe}^{\text{IV}}=\text{O}$ complexes are slightly shorter than in other known species, but not as much as the B3LYP results predict.

For the pentacoordinate $[L^1Fe^{IV}(O)]^{2+}$ complex, the Fe–O bond distances increase steadily from S=0 to S=2 and the difference in bond length between the spin states is quite large. For the hexacoordinate L^1 complexes however, there is relatively little difference between the Fe–O bond distances in the S=1 and S=2 spin state and what difference there is decreases with increasing the basicity of the co-ligand ($CH_3CN > OH_2 > ^-OH$).

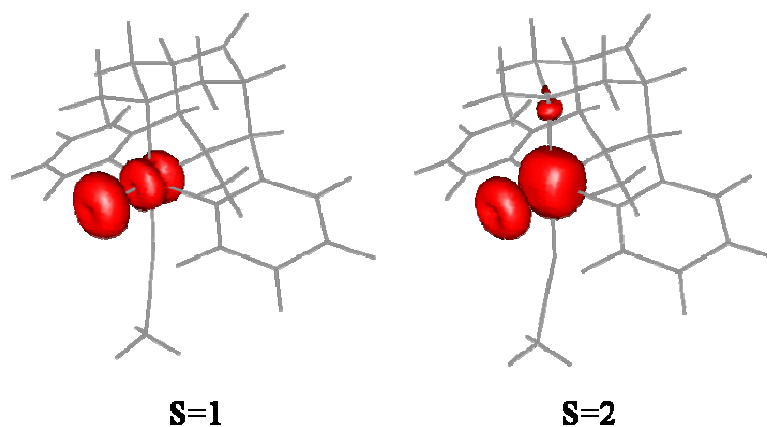


Figure 5.4. Mulliken spin densities of $[L^1Fe^{IV}(O)(CH_3CN)]^{2+}$ for S=1 and S=2

The spin density in the high spin L^1 complexes is mainly localised on the Fe=O unit, with a small percentage on N7, with the exception of $[L^1Fe^{IV}(O)(OH)]^+$, where there is practically no spin density on N7 and the “extra” spin is found on the ^-OH ligand. Figure 5.4 shows the spin density of $[L^1Fe^{IV}(O)(CH_3CN)]^{2+}$ in the S=1 and S=2 states. In the S=1 state, the Fe(d_{xz}) and Fe(d_{yz}) orbitals in which the two unpaired electrons are located are involved in π -bonding with the O(p_x) and O(p_y) orbitals respectively, which distributes the spin density across the Fe=O unit. This is reflected in the spin density profile, which has the shape of an average of these two molecular orbitals (compare to Figure 5.7). In the S=2 state, two further unpaired electrons, located in Fe(d_{xy}) and Fe($d_{x^2-y^2}$) type orbitals, contribute to the spin density profile. The d-shell is one electron away from being half-filled, which accounts for the near spherical symmetry of the spin density on the iron. The spin density on the oxo unit is due to the same two orbitals as for the S=1 state and the spin density profile is therefore similar. The Fe($d_{x^2-y^2}$) orbital is strongly mixed with the N7(p) orbital containing the lone pair (see Figure 5.7), which accounts for the observed spin density on N7. It is interesting to note that the spin

density profile in the high-spin state is practically identical to that observed in a pentacoordinate, trigonal-bipyramidal model complex of the TauD iron site, despite the difference in coordination geometries^[25]. This is the result of the strong π -bonding between the iron(IV) centre and the oxo ligand, which localises the spin density on the Fe=O unit, regardless of the coordination environment, and shows that, while high-spin Fe^{IV} does not correspond to a unique type of electron spin density profile, a high-spin Fe^{IV}=O unit does.

Fe^{IV}=O complexes of L²

In addition to the calculations on the tetradentate ligand L¹, the Fe^{IV}=O complexes of a second tetradentate ligand, L², were also investigated. This ligand was not chosen arbitrarily, but because it has been shown for the TPA family of ligands that substitution of methyl groups ortho to the coordinating nitrogen of the pyridine donors stabilises high-spin states relative to the unsubstituted TPA^[34]. It is therefore reasonable to assume that the same will be true for the bispidine ligands, which have a similar donor set to the TPA ligands, albeit with very different coordination geometries, due to the rigidity of the bispidine backbone.

For the [L²Fe^{IV}(O)]²⁺ complex, both coordination *trans* to N3 and *trans* to N7 was considered, as both forms have been observed in copper(II) complexes with this ligand^[35,36,37]. While here too the *trans* N3 site is preferred, due probably in part to the size of the oxo ligand, both possible isomers are located, with the oxo group coordinated *trans* N3 and *trans* N7 respectively. An interesting twist however, is that both isomers are not found for all spin states. The ground state is high-spin (S=2), with the oxo unit coordinated *trans* N3. The S=2, *trans* N7 isomer has an energy of 37.3 kJ/mol with respect to the ground state. For the S=1 state, no *trans* N3 isomer could be located and the *trans* N7 isomer is 26.5 kJ/mol higher in energy than the ground state (more stable than the S=2, *trans* N7 isomer). If a geometry optimisation is performed for the S=1 state, beginning with a geometry with a *trans* N3 bound oxo unit, it spontaneously moves to a *trans* N7 position. A PES scan, varying the N7–Fe–O angle from 90° to 180° in steps of 5°, indicates that not even a shallow *trans* N3 minimum exists. For the S=0 state, both the *trans* N3 and *trans* N7 isomers are found, but at extremely

high energies of 108.7 and 127.4 kJ/mol respectively, with respect to the ground state. The geometries and relative energies of the S=1 (*trans* N7) and S=2 (*trans* N3 and *trans* N7) structures are shown in Figure 5.5.

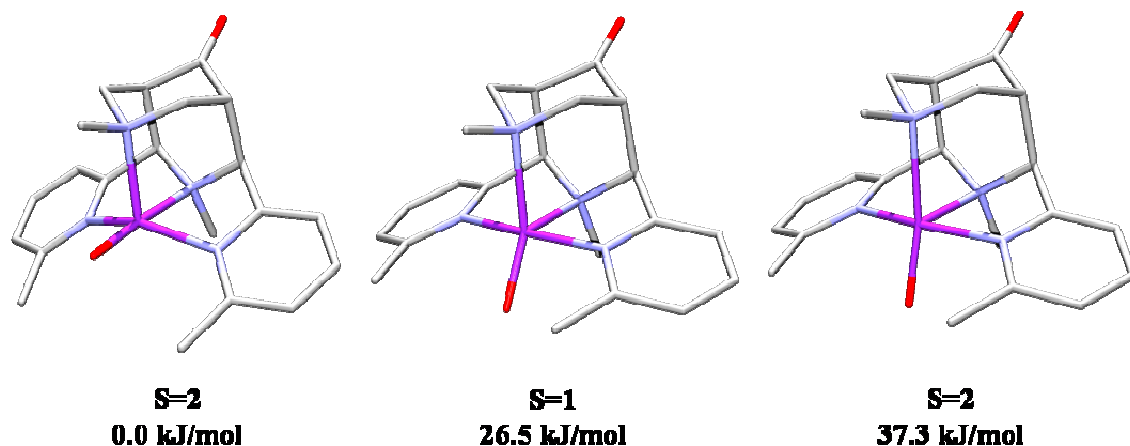


Figure 5.5. Optimised geometries of the S=1 and S=2 isomers of $[L^2Fe^{IV}(O)]^{2+}$

The lack of a *trans* N3 isomer for S=1 is remarkable, as is a comparison of the geometries of the three *trans* N7 structures (for S=0, 1 and 2). Whereas the optimised geometries of the S=0 and S=2 spin states have near to identical N7–Fe–O bond angles of 163.8 and 163.9° respectively, the S=1 state has an N7–Fe–O bond angle of 150.2°, so that the structure is perhaps better described as distorted trigonal-bipyramidal, than distorted square-pyramidal. A further notable point is that, for *trans* N7 coordination, the S=1 state is favoured by around 11 kJ/mol, as for L^7 (where *trans* N7 coordination is enforced by the ligand).

The spin density profile in the high-spin, *trans* N3 isomer of the L^2 complex is practically identical to that of $[L^1Fe^{IV}(O)]^{2+}$, while in the *trans* N7 isomer, the spin densities on N3 and N7 are inverted relative to $[L^1Fe^{IV}(O)]^{2+}$ (as is to be expected on the basis of their relative orientations to the oxo unit). It is interesting to note that in the low-spin (S=1) *trans* N7 isomer, substantially more spin density is localised on the iron centre (and correspondingly less on the oxo) than in the low-spin L^1 complexes and the low-spin complexes of the pentadentate ligands. This may be linked to the N7–Fe–O angle, which deviates significantly from the angle of 180° required for optimum overlap of the O(p_x) and O(p_y) orbitals with the Fe(d_{xz}) and Fe(d_{yz}) orbitals, so that less spin density can be delocalised on the oxo unit.

Restricted potential energy surface scans were performed on the $[\text{L}^2\text{Fe}^{\text{IV}}(\text{O})]^{2+}$ complex to determine the height of the energy barrier between the two isomers. For the high spin *trans* N3 and *trans* N7 structures, as well as the low spin *trans* N7 structure, the N7–Fe–O angle was incremented from 90° to 170° in steps of 5° . The height of this barrier is significant since, while the oxo ligand is small enough to overcome the steric strain induced by the methyl substituents in the *trans* N3 position, the substrates in the possible precursors, $[\text{L}^2\text{Fe}^{\text{II}}(\text{HOOH})]^{2+}$ and $[\text{L}^2\text{Fe}^{\text{III}}(\text{OOH})]^{2+}$, may be too bulky for *trans* N3 coordination. If this is indeed the case, the $\text{Fe}^{\text{IV}}=\text{O}$ species would initially be formed with the oxo ligand *trans* to N7 and this species would then rearrange to form the *trans* N3 ground state. The S=1, *trans* N7 and S=2, *trans* N3 curves cross each other at an N7–Fe–O angle of around 124° and an energy of 52.0 kJ/mol with respect to the S=2, *trans* N3 ground state (21.2 kJ/mol with respect to the S=1 *trans* N7 isomer). This can be seen as the point at which the spin state crossover between the S=1 *trans* N7 ground state and the S=2 *trans* N3 ground state takes place and the energy at this point approximates the energy of the transition state. At 52.0 kJ/mol, the energy barrier is fairly low, indicating that the mechanism of $\text{Fe}^{\text{IV}}=\text{O}$ formation *trans* to N7 followed by a transition to a *trans* N3 structure is plausible.

Due to the lack of a *trans* N3 isomer for the S=1 state of $[\text{L}^2\text{Fe}^{\text{IV}}(\text{O})]^{2+}$, the stabilisation of the S=2 state relative to the L^1 complexes is difficult to quantify. For this reason, calculations were performed on $[\text{L}^2\text{Fe}^{\text{IV}}(\text{O})(\text{CH}_3\text{CN})]^{2+}$ in the S=1 and S=2 states. Through the additional acetonitrile ligand, the oxo ligand is forced to coordinate *trans* to N3, as for $[\text{L}^1\text{Fe}^{\text{IV}}(\text{O})(\text{CH}_3\text{CN})]^{2+}$. The energy difference between the S=2 and S=1 states in this complex is 9.7 kJ/mol, compared to an energy difference of 0.5 kJ/mol in $[\text{L}^1\text{Fe}^{\text{IV}}(\text{O})(\text{CH}_3\text{CN})]^{2+}$. The geometries in both spin states are similar to those of the corresponding L^1 complex, with the exception of the Fe–N_{py} bond distances, which are slightly longer due to the steric strain of the *ortho* substituted methyl groups. The spin density distribution is also almost identical to that of $[\text{L}^1\text{Fe}^{\text{IV}}(\text{O})(\text{CH}_3\text{CN})]^{2+}$. Methylation of the pyridine rings therefore leads to an added stabilisation of the high-spin state by approximately 10 kJ/mol, without significantly changing the electronic properties of the Fe=O unit.

Fe^{IV}=O complexes of L⁶ and L⁷

In the complexes of the two pentadentate bispidine isomers L⁶ and L⁷, one of the two coordination sites available in the L¹ complexes is blocked by an additional pyridine donor (see Figure 6.1), leading to substrate coordination exclusively *trans* N3 (L⁶) or *trans* N7 (L⁷). The same effect that is observed for L¹ complexes is also found here, namely that *trans* N3 coordination is favoured over *trans* N7 coordination, leading generally to short and strong substrate bonds in L⁶ complexes and longer, relatively weaker bonds in L⁷ complexes. This can be seen, for example, in the crystal structures of their Fe(II) complexes^[15].

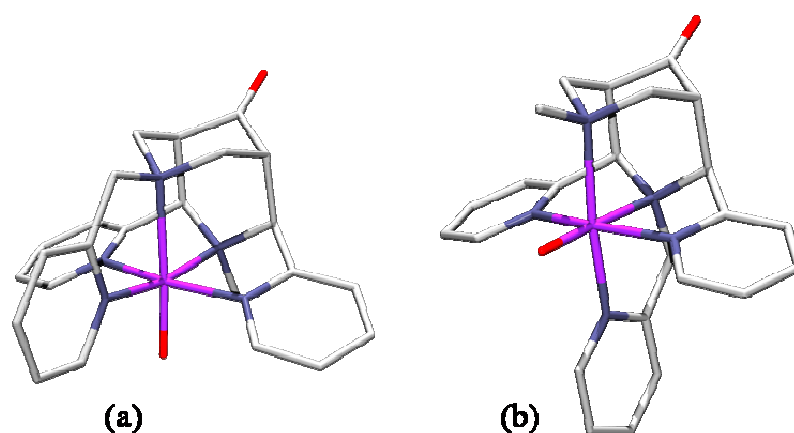


Figure 5.6. Optimised geometries of the S=1 ground states of (a) [L⁷Fe^{IV}(O)]²⁺ and (b) [L⁶Fe^{IV}(O)]²⁺

The calculated structures of [L⁶Fe^{IV}(O)]²⁺ and [L⁷Fe^{IV}(O)]²⁺ are shown in Figure 6.6^[38]. Both isomers have an S=1 ground state with the S=2 state lying 19.8 kJ/mol and 15.8 kJ/mol higher in energy for L⁶ and L⁷ respectively. For both spin states, the L⁶ isomer (oxo *trans* N3) is more stable than the L⁷ isomer (oxo *trans* N7). It is interesting to note also that for both spin states, the Fe–O bond lengths are identical in the L⁶ and L⁷ isomers, which is contrast to the usual tendency for stronger substrate bonding in L⁶ complexes than in L⁷ complexes. This is also reflected in the Fe–O frequencies, which are identical for the two isomers in the S=1 state. This is probably due to the strong Fe=O π -bonding interactions, which override the tendency for stronger substrate binding in the L⁶ complexes than in the L⁷ complexes (due to the restraints of the bispidine backbone).

For L^6 , the spin density profiles in both spin states are practically identical to those of the L^1 complexes. For L^7 , the spin densities on the Fe=O unit agree with those of the L^1 and L^6 complexes, while the spin densities on N3 and N7 are similar to those of the low-spin, *trans* N7 isomer of $[L^2Fe^{IV}(O)]^{2+}$ (again due to the orientation relative to the Fe=O unit). Here the *trans* N7 binding of the oxo ligand does not lead to less delocalisation of the spin density in the S=1 state, as observed in the S=1, *trans* N7 isomer of $[L^1Fe^{IV}(O)]^{2+}$, because the N7–Fe–O is much closer to 180° and efficient orbital overlap is possible.

Comparison of the spin states in the tetradentate and pentadentate $Fe^{IV}=O$ complexes

The difference in spin states between the $Fe^{IV}=O$ complexes of tetradentate and pentadentate bispidine-type ligands can be rationalised in terms of simple ligand field theory. The bispidine ligand imposes a distorted octahedral geometry on the iron centre, which means that the d-orbitals are split into a t_{2g} and an e_g set. However, in bispidine complexes, the degeneracy of the orbitals is completely lifted, due to the different ligand field strengths of the donors. If we define our coordinate system as such that the z-axis lies along the Fe–O bond, the Fe–N_{py} bonds along the x-axis and the Fe–N_{am} bond *cis* to the oxo unit along the y-axis (as shown in Figure 5.2), the d-orbitals will be arranged in the order $d_{xy} < d_{yz} \leq d_{xz} \ll d_{x^2-y^2} < d_{z^2}$ in the L^1 $Fe^{IV}=O$ complexes. This is due the arrangement of the ligands in the spectrochemical series ($\bar{O}H < O^{2-} < OH_2 < CH_3CN < NH_3 < NR_3 \leq py$). While the energy difference between the d_{yz} and d_{xz} orbitals is expected to be small on the basis of the similar donor strengths of tertiary amines and pyridines, it is nonetheless expected due to the restriction imposed by the rigid bispidine backbone, which enforces long metal–N7 bonds and therefore weakens the ligand field in the y-direction. For the d^4 $Fe^{IV}=O$ systems, the S=1 state will have a doubly occupied d_{xy} orbital, an unpaired electron in the d_{yz} and d_{xz} orbitals and empty $d_{x^2-y^2}$ and d_{z^2} orbitals, whereas in the S=2 state, a single electron will occupy all the d-orbitals but the d_{z^2} . The main factor determining the ground spin state is therefore the energy of the $d_{x^2-y^2}$ orbital. Figure 5.7 shows the five molecular orbitals of $[L^1Fe^{IV}(O)(CH_3CN)]^{2+}$ containing the greatest percentage of the respective Fe(d) orbitals, and a comparison of the relative energies of the

corresponding orbitals in $[L^1Fe^{IV}(O)(CH_3CN)]^{2+}$ and $[L^6Fe^{IV}(O)]^{2+}$. In the complexes with L^1 , the $d_{x^2-y^2}$ orbital will have a fairly low energy, due to the fact that there are no restrictions on the length of the Fe–X bond and, more importantly, due to the restrictions of the rigid ligand backbone, which favours large Fe–N7 distances, leading to a decreased repulsion with the $d_{x^2-y^2}$ orbital. Consequently, Δ_o is relatively small in comparison to other systems with similar donor sets and the high-spin state is favoured. Within the series of L^1 complexes, the stabilisation of the high-spin state increases in the order $[L^1Fe^{IV}(O)(CH_3CN)]^{2+} < [L^1Fe^{IV}(O)(OH_2)]^{2+} < [L^1Fe^{IV}(O)(OH)]^+ < [L^1Fe^{IV}(O)]^{2+}$, as the ligand field in the y-direction increases and the $d_{x^2-y^2}$ orbital is destabilised (Δ_o increases).

The $[L^2Fe^{IV}(O)]^{2+}$ complex shows a slightly larger energetic preference for the high-spin state than do the L^1 complexes (there is no S=1 isomer in the favoured *trans* N3 position). This is probably due steric hinderance of the methyl substituents in L^2 , which leads to a distortion from ideal octahedral geometry, in that the Npy–Fe–Npy angle decreases and the N3–Fe–O angle increases. The Npy donors no longer lie directly along the x-axis; there is less repulsion with the $d_{x^2-y^2}$ orbital, which leads to a decrease in its energy. This leads to a decrease in Δ_o relative to the L^1 complex, which favours the high-spin state even more. There is also a slight increase in the Fe–Npy bond distances in L^2 , with respect to L^1 , which contributes to the weakening of the ligand field in the x-direction. In the $[L^2Fe^{IV}(O)(CH_3CN)]^{2+}$ complex, the angular geometry is less affected, but the Fe–Npy bond lengths are significantly increased, leading again to a decrease in the repulsion with, and the energy of, the $d_{x^2-y^2}$ orbital.

In the complexes with the pentadentate ligands, the replacement of the co-ligand X with an addition pyridine donor increases the ligand field in the y-direction, thereby favouring a low-spin (S=1) state. In addition to this electronic effect, the steric effect of the third pyridine donor restricts the length of the Fe–Nam bonds in the y-direction (compare, for example, the Fe–X and Fe–N7 bond lengths in the structures of $[L^1Fe^{IV}(O)(CH_3CN)]^{2+}$ and $[L^6Fe^{IV}(O)]^{2+}$), increasing the ligand field and the energy of the $d_{x^2-y^2}$ orbital even further. This also has the result that relative energies of the d_{yz} and d_{xz} orbitals are inverted (see Figure 5.7).

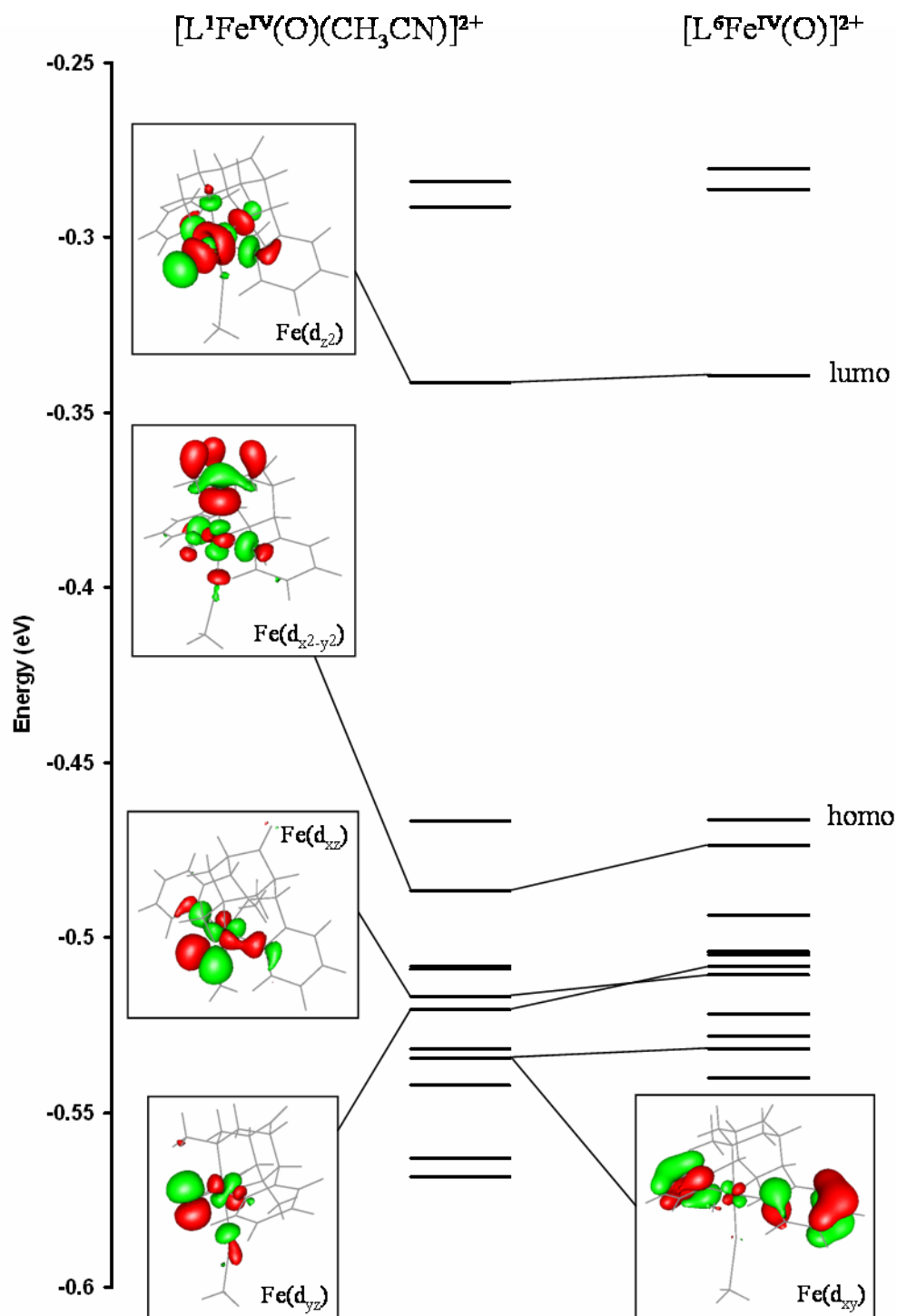


Figure 5.7. Orbital energy levels for the S=2 states of $[L^1Fe^{IV}(O)(CH_3CN)]^{2+}$ and $[L^6Fe^{IV}(O)]^{2+}$

5.4. Conclusion

In summary, a systematic study of the electronic nature of bispidine $\text{Fe}^{\text{IV}}=\text{O}$ complexes was conducted. The results suggest that the $\text{Fe}^{\text{IV}}=\text{O}$ complexes of tetradentate bispidine ligands may have high-spin ($S=2$) ground states, making them attractive synthetic models for the high-spin $\text{Fe}^{\text{IV}}=\text{O}$ intermediates believed to be the active species in the catalytic cycles of many mononuclear non-heme iron enzymes. The rigidity of the bispidine backbone, which enforces long $\text{Fe}-\text{N7}$ bonds, plays a large part in stabilising the high-spin state in the $\text{Fe}^{\text{IV}}=\text{O}$ complexes of tetradentate bispidine ligands. Coordination of weak field co-ligands such as OH^- in the free coordination site helps to further stabilise the high-spin configuration. The $\text{Fe}^{\text{IV}}=\text{O}$ complexes of pentadentate bispidine ligands, on the other hand, are low-spin ($S=1$), which can be explained on the basis of the additional strong-field pyridine donor and the shortening of the $\text{Fe}-\text{N7}$ and $\text{Fe}-\text{X}$ bonds enforced by the steric strain of the pendant arm. A further interesting result is that the spin density profile in the high-spin complexes is practically identical to that observed in a five-coordinate, trigonal-bipyramidal model complex of the TauD iron site, despite the difference in coordination geometries. This suggests that, while a high-spin Fe^{IV} centre does not correspond to a unique type of electron spin density profile, a high-spin $\text{Fe}^{\text{IV}}=\text{O}$ unit does, which implies that the coordination environment of the $\text{Fe}^{\text{IV}}=\text{O}$ unit can be varied to stabilise the high-spin state, without affecting the applicability of the model system to enzymatic high-spin oxoiron(IV) units, such as that of TauD.

5.5. References

- ¹ M. Costas, M.P. Mehn, M.P. Jensen, L. Que Jr., *Chem. Rev.*, **2004**, 104, 939
- ² S.J. Lange, H. Miyake and L. Que, Jr., *J. Am. Chem. Soc.*, **1999**, 121, 6330
- ³ C.A. Grapperhaus, B. Mienert, E. Bill, T. Weyhermüller and K. Weighardt, *Inorg. Chem.* **2000**, 39, 5306
- ⁴ J. Kaizer, E.J. Klinker, N.Y. Oh, J-U. Rohde, W.J. Song, A. Stubna, J. Kim, E. Münck, W. Nam and L. Que, Jr., *J. Am. Chem. Soc.*, **2004**, 126, 472
- ⁵ Meunier, B.; de Visser, S. P.; Shaik, S., *Chem. Rev.*, **2004**, 104, 3947
- ⁶ Green, M. T.; Dawson, J. H.; Grey, H. B., *Science*, **2004**, 304, 1653
- ⁷ K.E. Lui, A.M. Valentine, D. Wang, B.H. Huynh, D.E. Edmondson, A. Salifoglou, S.J. Lippard, *J. Am. Chem. Soc.*, **1995**, 117, 10174
- ⁸ L. Shu, J.C. Nesheim, K. Kaufmann, E. Münck, J.D. Lipscomb, L. Que, Jr., *Science*, **1997**, 275, 515
- ⁹ J.C. Price, E.W. Barr, B. Tirupati, M. Bollinger Jr., C. Krebs, *Biochemistry*, **2003**, 42, 7497
- ¹⁰ J.C. Price, E.W. Barr, T.E. Glass, C. Krebs, J.M. Bollinger, Jr., *J. Am. Chem. Soc.*, **2003**, 125, 13008
- ¹¹ D.A. Proshlyakov, T.F. Henshaw, G.R. Monterosso, M.J. Ryle, R.P. Hausinger, *J. Am. Chem. Soc.*, **2004**, 126, 1022
- ¹² P.J. Riggs-Gelasco, J.C. Price, R.B. Guyer, J.H. Brehm, E.W. Barr, J.M. Bollinger, C. Krebs, *J. Am. Chem. Soc.*, **2004**, 126, 8108
- ¹³ G.H. Posner, J.N. Cumming, P. Ploypradith and C.H. Oh, *J. Am. Chem. Soc.*, **1995**, 117, 5885
- ¹⁴ L. Que Jr., *J. Chem. Soc. Dalton Trans.*, **1997**, 21, 3933; Y. Dong, Y. Zang, K. Kauffmann, L. Shu, E.C. Wilkinson, E. Muenck, L. Que Jr., *J. Am. Chem. Soc.*, **1997**, 119, 12683; H-F Hsu, Y. Dong, L. Shu, V.G. Young, L. Que Jr., *J. Am. Chem. Soc.*, **1999**, 121, 5230; V.L. MacMurdo, H. Zheng, L. Que Jr., *Inorg. Chem.*, **2000**, 39, 2254
- ¹⁵ H. Börzel, P. Comba, K.S. Hagen, Y.D. Lampeka, A. Lienke, G. Linti, M. Merz, H. Pritzkow, L.V. Tsymbal, *Inorg. Chim. Acta*, **2002**, 337, 407
- ¹⁶ J-U. Rohde, J-H. In, M.H. Lim, W.W. Brennessel, M.R. Bukowski, A. Stubna, E. Münck, W. Nam, L. Que Jr., *Science*, **2003**, 299, 1037
- ¹⁷ A. Decker, J-U. Rhode, L. Que Jr., E.I. Solomon, *J. Am. Chem. Soc.*, **2004**, 126, 5378
- ¹⁸ E.J. Klinker, J. Kaizer, W.W. Brennessel, N.L. Woodrum, C.J. Cramer and L. Que, Jr., *Angew. Chem.*, **2005**, 117, 3756

- ¹⁹ T. Wolter, W. Meyer-Klaucke; M. Müther, D. Mandon, H. Winkler, A.X. Trautwein, R. Weiss, *J. Inorg. Biochem.*, **1986**, 78, 7819
- ²⁰ J.E. Penner-Hahn, K. Smith Eble, T.J. McMurry, M. Renner, A.L. Balch, J.T. Groves, J.H. Dawson, K.O. Hodgson, *J. Am. Chem. Soc.*, **1986**, 108, 7819
- ²¹ M. Chance, L. Powers, T. Poulos, B. Chence, *Biochemistry*, **1986**, 25, 1266
- ²² C.E. MacBeth, A.P. Golombek, V.G. Young, Jr., C. Yang, K. Kuczera, M.P. Hendrich, A.S. Borovik, *Science*, **2000**, 289, 938
- ²³ T.J. Collins, K.L. Kosta, E. Münck, E.S. Uffelman, *J. Am. Chem. Soc.*, **1990**, 112, 5637
- ²⁴ K.L. Kostka, B.G. Fox, M.P. Hendrich, T.J. Collins, C.E.F. Rickard, L.J. Wright and E. Münck, *J. Am. Chem. Soc.*, **1993**, 115, 6746
- ²⁵ A. Ghosh, E. Tangen, H. Ryeng and P.R. Taylor, *Eur. J. Inorg. Chem.*, **2004**, 4555
- ²⁶ M.R. Bukowski, P. Comba, A. Lienke, C. Limberg, C. Lopez de Laorden, M. Merz, L. Que Jr., *Angew. Chem.*, *accepted*
- ²⁷ J. Bautz, M.R. Bukowski, A. Stubna, M. Kerscher, A. Lienke, P. Comba, E. Münck and L. Que, Jr., *Angew. Chem.*, *submitted*
- ²⁸ *Gaussian 03, Revision B.03*, M. J. Frisch, G. W. Trucks, H. B. Schlegel, G. E. Scuseria, M. A. Robb, J. R. Cheeseman, J. A. Montgomery, Jr., T. Vreven, K. N. Kudin, J. C. Burant, J. M. Millam, S. S. Iyengar, J. Tomasi, V. Barone, B. Mennucci, M. Cossi, G. Scalmani, N. Rega, G. A. Petersson, H. Nakatsuji, M. Hada, M. Ehara, K. Toyota, R. Fukuda, J. Hasegawa, M. Ishida, T. Nakajima, Y. Honda, O. Kitao, H. Nakai, M. Klene, X. Li, J. E. Knox, H. P. Hratchian, J. B. Cross, C. Adamo, J. Jaramillo, R. Gomperts, R. E. Stratmann, O. Yazyev, A. J. Austin, R. Cammi, C. Pomelli, J. W. Ochterski, P. Y. Ayala, K. Morokuma, G. A. Voth, P. Salvador, J. J. Dannenberg, V. G. Zakrzewski, S. Dapprich, A. D. Daniels, M. C. Strain, O. Farkas, D. K. Malick, A. D. Rabuck, K. Raghavachari, J. B. Foresman, J. V. Ortiz, Q. Cui, A. G. Baboul, S. Clifford, J. Cioslowski, B. B. Stefanov, G. Liu, A. Liashenko, P. Piskorz, I. Komaromi, R. L. Martin, D. J. Fox, T. Keith, M. A. Al-Laham, C. Y. Peng, A. Nanayakkara, M. Challacombe, P. M. W. Gill, B. Johnson, W. Chen, M. W. Wong, C. Gonzalez, and J. A. Pople, *Gaussian, Inc., Pittsburgh PA, 2003*
- ²⁹ C. Lee, W. Yang, R. Parr, *Phys. Rev. B*, **1988**, 37, 785; A.D. Becke, *J. Chem. Phys.*, **1993**, 98, 5648
- ³⁰ A. Schäfer, C. Huber and R. Ahlrichs, *J. Chem. Phys.*, **1994**, 100, 5829
- ³¹ M.T. Cancès, B. Mennucci and J. Tomasi, *J. Chem. Phys.*, **1997**, 107, 3032; M. Cossi, V. Barone, B. Mennucci and J. Tomasi, *Chem. Phys. Lett.*, **1998**, 286, 253; B. Mennuci and J.

Tomasi, *J. Chem. Phys.*, **1997**, 106, 5151; M. Cossi, G. Scalmani, N. Rega and V. Barone, *J. Chem. Phys.*, **2002**, 117, 43

³² P. Comba, A. Lienke, *Inorg. Chem.*, **2001**, 40, 5206

³³ A.J. Boone, C.H. Chang, S.N. Greene, T. Herz, N.G.J. Richards, *Coord. Chem. Rev.*, **2003**, 291, 238

³⁴ Y. Zang, J. Kim, Y. Dong, E.C. Wilkinson, E.H. Appelman and L. Que, Jr., *J. Am. Chem. Soc.*, **1997**, 119, 4197

³⁵ H. Börzel, P. Comba, K.S. Hagen, C. Katsichtis, H. Pritzkow, *Chem. Eur. J.*, **2000**, 6, 914.

³⁶ H. Börzel, P. Comba, K.S. Hagen, M. Kerscher, H. Pritzkow, M. Schatz, S. Schindler, O. Walter, *Inorg. Chem.*, **2002**, 41, 5440

³⁷ P. Comba, B. Martin, A. Prikhod'ko, H. Pritzkow, H. Rohwer, *C.R. Chimie*, **2005**, 8, 1506

³⁸ Calculations performed by Anna Anastasi from the University of York, UK

6. The Electronic Nature of the Iron(III)-hydroperoxo and Iron(III)-peroxo Complexes of 3,7-Diazabicyclo[3.3.1]nonane Derivatives

6.1. Introduction

As the initially formed species in many enzymatic oxidation processes, 1:1 metal-O₂ adducts are of great interest in biological systems. Two binding modes have been identified in 1:1 metal-O₂ complexes, end-on (η^1) and side-on (η^2) (see Figure 2.1 for these and further binding modes for copper(II)). These adducts are generally defined as superoxo or peroxo complexes on the basis of X-ray structural data (O–O bond distances, $r_{\text{O-O}}$) and vibrational spectroscopy (O–O stretching frequencies, $\nu_{\text{O-O}}$)^[1]. Compounds with O–O bond lengths of $\sim 1.4\text{--}1.5$ Å and stretching frequencies of $\sim 800\text{--}930$ cm⁻¹ are thereby defined as peroxides, whereas those with O–O bond lengths of $\sim 1.2\text{--}1.3$ Å and stretching frequencies of $\sim 1050\text{--}1200$ cm⁻¹ are regarded as superoxides^[2]. In the particular case of iron, peroxide-level intermediates have been observed in heme model chemistry (cytochrome P450)^[3] and the formation of an Fe^{III}-superoxo species is the first step in the reaction cycle of DNA cleavage by the antitumor drug bleomycin^[4].

Due to their biological application, the synthesis of ligands able to stabilise 1:1 metal-O₂ adducts and the characterisation of the corresponding complexes has become an important field in bioinorganic chemistry. One of the earliest examples of a synthetic Fe^{III}-peroxo complex is that of [Fe^{III}(EDTA)(O₂)]³⁻, which can be formed by the addition of H₂O₂ to [Fe^{III}(EDTA)]⁻ or KO₂ to [Fe^{II}(EDTA)]²⁻ at elevated pH^[5] and functions as a catalyst for the decomposition of H₂O₂, superoxide dismutation and organic substrate oxidation in the presence of H₂O₂^[6,7].

In recent years, a number of iron complexes with pentadentate ligands containing a mixed amine/pyridine donor set, that react with H₂O₂ to form metastable low-spin Fe^{III}-hydroperoxo (η^1) intermediates with hydroperoxo–Fe^{III} charge transfer bands between 500 and 600 nm, have been extensively characterised^[8]. Deprotonation of these species yields their respective

conjugate bases, which have been spectroscopically characterised as high-spin, side-on (η^2) Fe^{III} -peroxo complexes. Both Fe^{III} -hydroperoxo and Fe^{III} -peroxo intermediates can be formed with the pentadentate bispidine ligands L^6 and L^7 [9], by the reaction of their Fe^{II} precursors with H_2O_2 , and have been characterised by EPR, UV-Vis and resonance Raman spectroscopy. In addition, the structures of the high-spin $\eta^2 \text{Fe}^{\text{III}}$ -peroxo intermediates were optimised using DFT methods and heptacoordination of the metal centre was determined. The reaction of the tetradentate bispidine ligand L^1 with H_2O_2 does not lead to any observable Fe^{III} intermediates, but the direct synthesis of $[\text{L}^1\text{Fe}(\text{O}_2)]^+$ by the addition of KO_2 to a neutral aqueous solution of the Fe^{II} precursor, could be achieved [10]. In addition, an Fe^{III} -alkylperoxo complex of L^1 , $[\text{L}^1\text{Fe}^{\text{III}}(\text{O}t\text{Bu})]^{2+}$, could be isolated and characterised by EPR, UV-Vis and Resonance Raman [11], and has been shown to lie close to the spin crossover limit.

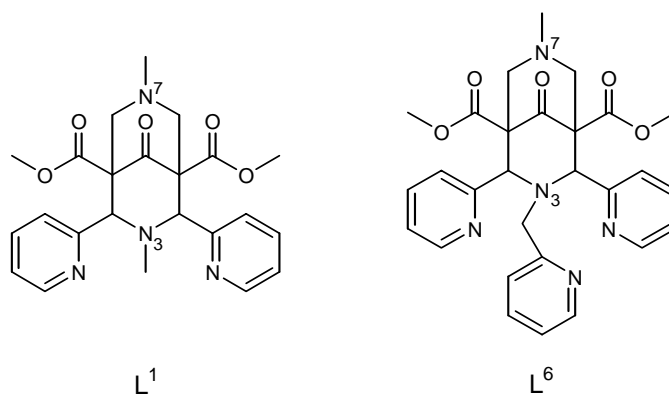


Figure 6.1. The ligands investigated

Here we report DFT calculations of the Fe^{III} -peroxo complexes of the bispidine ligands L^1 and L^6 (see Figure 6.1). Different coordination modes are considered and the electronic nature of the formally Fe^{III} -peroxo species is studied, including bonding interactions between the iron centre and the peroxo unit. Both side-on (η^2) Fe^{III} -peroxo and end-on (η^1) Fe^{II} -superoxo species have been located for $[\text{L}^1\text{Fe}(\text{O}_2)(\text{CH}_3\text{CN})]^+$ and $[[\text{L}^6\text{Fe}(\text{O}_2)]^+$.

6.2. Computational Methods

All calculations were performed with Gaussian03^[12] using DFT methods. Geometries were fully optimised in the gas phase using the B3LYP functional^[13] and a 6-31G(d) basis set. Frequency calculations were performed on the B3LYP optimised structures and force constants and thermodynamic data calculated in the process. Single Point energy calculations were performed on the B3LYP optimised structures using Ahlrich's TZVPP basis set^[14] on all atoms and including solvent effects, using the PCM^[15] with acetonitrile as a solvent. As in Chapters 4 and 5, coordination of CH₃CN and H₂O *trans* to N7, as well as leaving the extra coordination site open, was considered for L¹. The same simplified model system as used in previous Chapters was also used here.

6.3. Results and Discussion

The Fe^{III}-hydroperoxo species

The Fe^{III}-hydroperoxo complexes of L¹, particularly the temperature dependence of their ground spin states, have been discussed in Chapter 4. The Mulliken spin densities are given in Table 6.1 and the geometries are given in Addendum A. The O–O bond distances range between 1.44 and 1.46 Å (S=1/2), 1.44 and 1.45 Å (S=3/2) and 1.41 and 1.43 Å (S=5/2), depending on the co-ligand, while the Fe–O bond distances range between 1.78 and 1.80 Å (S=1/2), 1.76 and 1.78 Å (S=3/2) and 1.83 and 1.86 Å (S=5/2). The Mulliken spin densities on the iron centre are as expected for the S=1/2 (~ 1) and S=3/2 (~ 3) spin states. For the S=5/2 state, the spin densities on the iron centre are lower than the theoretical value of 5 (~ 4), there is significant spin density donation to the hydroperoxo unit (~ 0.4) and some slight donation to the other ligands.

Table 6.1. Mulliken spin densities on the iron and ligands of the LFe^{III}-hydroperoxo species, for L¹ and L⁶

Atoms	Fe	N7	N3	Npy1	Npy2	O1	O2	X
Complexes								
[L ¹ Fe(OOH)] ²⁺ , S=5/2	4.12	0.10	0.08	0.063	0.06	0.39	0.10	-
[L ¹ Fe(OOH)] ²⁺ , S=3/2	2.76	0.07	-0.05	-0.001	-0.00	0.14	0.02	-
[L ¹ Fe(OOH)] ²⁺ , S=1/2	1.023	-0.03	-0.02	-0.016	-0.01	0.04	-0.01	-
[L ¹ Fe(OOH)(CH ₃ CN)] ²⁺ , S=5/2	4.15	0.09	0.06	0.066	0.06	0.38	0.09	0.04
[L ¹ Fe(OOH)(CH ₃ CN)] ²⁺ , S=3/2	2.75	0.09	-0.04	-0.026	-0.03	0.14	0.03	0.04
[L ¹ Fe(OOH)(CH ₃ CN)] ²⁺ , S=1/2	0.81	-0.02	-0.02	-0.006	-0.01	0.21	0.04	-0.01
[L ¹ Fe(OOH)(H ₂ O)] ²⁺ , S=5/2	4.19	0.09	0.07	0.069	0.07	0.34	0.07	0.04
[L ¹ Fe(OOH)(H ₂ O)] ²⁺ , S=3/2	2.79	0.08	-0.05	-0.016	-0.02	0.11	0.02	0.03
[L ¹ Fe(OOH)(H ₂ O)] ²⁺ , S=1/2	0.90	-0.02	-0.02	-0.008	-0.01	0.15	0.02	-0.01
[L ⁶ Fe(OOH)] ²⁺ , S=5/2	4.16	0.08	0.06	0.068	0.06	0.34	0.08	0.08
[L ⁶ Fe(OOH)] ²⁺ , S=3/2	2.77	0.07	-0.04	-0.010	-0.01	0.08	0.00	0.07
[L ⁶ Fe(OOH)] ²⁺ , S=1/2	0.87	-0.01	-0.02	-0.012	-0.01	0.18	0.02	-0.01

The Fe^{III}-peroxo/Fe^{II}-superoxo species

Deprotonation the Fe^{III}-hydroperoxo complex by addition of a strong base leads to a formally Fe^{III}-peroxo species. Three different coordination modes were considered, namely side-on (η^2) coordination in plane with Fe, N3 and N7 (mode (1), denoted as ls/hs(1)), side-on (η^2) coordination in plane with Fe and the pyridine rings (mode (2)) and end-on (η^1) coordination (mode (3)). The geometries and relative energies of the optimised complexes are given in Table 6.2 and Figure 6.2 shows the optimised structures located for $[L^1Fe(O_2)]^+$.

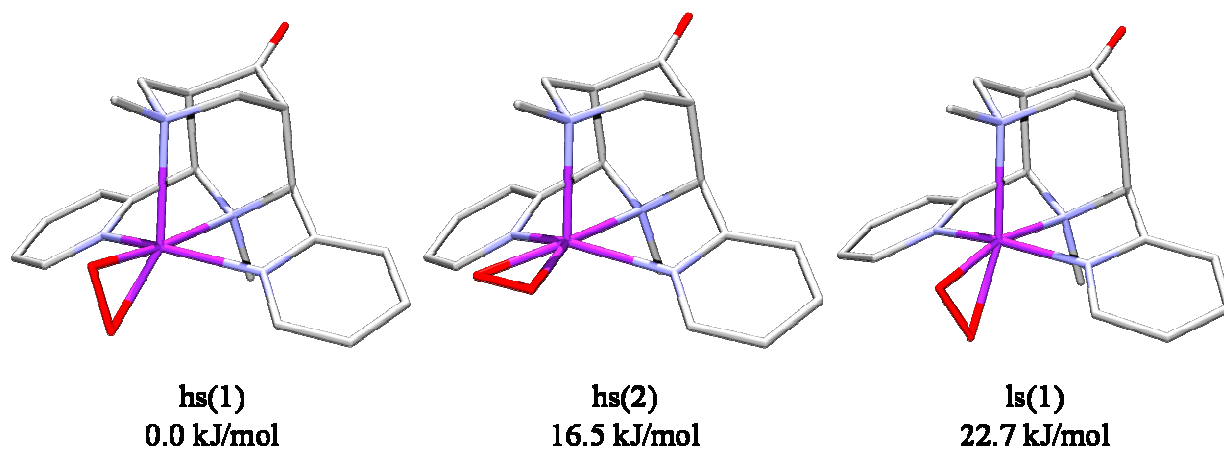


Figure 6.2. The three coordination modes of $[L^1Fe(O_2)]^+$ and their relative energies

The ground state is hs(1), which is 16.5 kJ/mol more stable than the hs(2) and 22.7 kJ/mol more stable than the ls(1) complex. An optimisation starting from an ls(2) structure converges to ls(1). The addition of acetonitrile in the open coordination site *trans* N7 reverses this trend, stabilizing hs(2) by circa 17 kJ/mol relative to hs(1). In fact, the acetonitrile in the hs(1) structure detaches itself from the iron centre and convergence is reached at an Fe–Nac distance of 3.323 Å. This structure is not a minimum, but has one negative frequency (an N7–Fe–Nac bending mode). Two low-spin structures are also found for $[L^1Fe(O_2)(CH_3CN)]^+$, one with a side-on bound peroxo unit (ls(2)) and one with an end-on bound peroxo unit (ls(3)), with energies of 89.5 and 52.1 kJ/mol relative to the hs(2) ground state respectively. These are shown in Figure 6.3. It is interesting to note that in the low-spin state, the end-on binding mode is more stable than the side-on binding mode by about 25 kJ/mol.

Table 6.2. Selected geometric parameters and relative energies of electronic states for the $LFeO_2^+$ complexes of L^1 and L^6

Ligand	$[L^1Fe(O_2)]^+$			$[L^1Fe(O_2)(X)]^+$, X=CH ₃ CN			X=H ₂ O			$[L^6Fe(O_2)]^+$		
	ls(1)	hs(1)	hs(2)	ls(2)	hs(2)	ls(3)	hs(2)	hs(2)	hs(2)	hs(2)	hs(2)	ls(3)
Bond distances (Å)												
Fe-N7	2.156	2.334	2.222	2.160	2.369	2.198	2.277	2.303	2.277	2.303	2.195	2.195
Fe-N3	2.048	2.263	2.299	2.348	2.336	2.062	2.303	2.339	2.303	2.339	2.034	2.034
Fe-Npy1	1.984	2.157	2.210	2.182	2.230	2.000	2.247	2.281	2.247	2.281	1.991	1.991
Fe-Npy2	1.984	2.157	2.210	2.181	2.230	1.981	2.249	2.296	2.249	2.296	1.981	1.981
Fe-O1	1.794	1.927	1.947	1.858	1.964	1.888	1.901	1.910	1.901	1.910	1.872	1.872
Fe-O2	1.829	1.904	1.947	1.858	1.964	2.797	1.935	1.911	1.935	1.911	2.810	2.810
Fe-X	-	-	-	1.930	2.257	1.905	2.301	2.169	2.301	2.169	1.969	1.969
O1-O2	1.414	1.390	1.373	1.397	1.371	1.321	1.420	1.410	1.420	1.410	1.328	1.328
N7..N3	2.888	3.022	3.021	2.998	3.017	2.937	2.998	3.007	2.998	3.007	2.948	2.948
Valence angles (°)												
N7-Fe-N3	86.74	82.19	83.84	83.26	79.75	87.13	81.77	80.74	81.77	80.74	88.30	88.30
Npy1-Fe-Npy2	161.23	146.34	139.22	142.36	143.84	165.14	143.33	144.40	143.33	144.40	166.04	166.04
N7-Fe-O1	108.87	92.47	102.98	90.85	94.38	89.15	98.06	100.90	98.06	100.90	89.85	89.85
N7-Fe-O2	154.81	135.03	102.93	90.87	94.38	100.23	101.09	100.51	101.09	100.51	102.05	102.05
N7-Fe-X	-	-	-	179.15	176.98	175.03	175.23	158.45	175.23	158.45	173.87	173.87
Fe-O1-O2	68.32	67.85	69.35	67.92	69.58	120.24	69.54	68.36	69.54	68.36	121.86	121.86
Torsion angles (°)												
N3-C-C-Npy1/2	36.67	35.02	34.48	39.20	36.68	39.20	37.34	41.16	37.34	41.16	39.51	39.51
N7-Fe-O1-O2	179.99	179.98	94.91	-90.36	91.63	117.92	-97.65	-93.82	-97.65	-93.82	121.74	121.74
Relative Energies (kJ/mol)												
Solvent	22.7	0.0	16.5	89.5	0.0	52.1	0.0	0.0	0.0	0.0	41.6	41.6

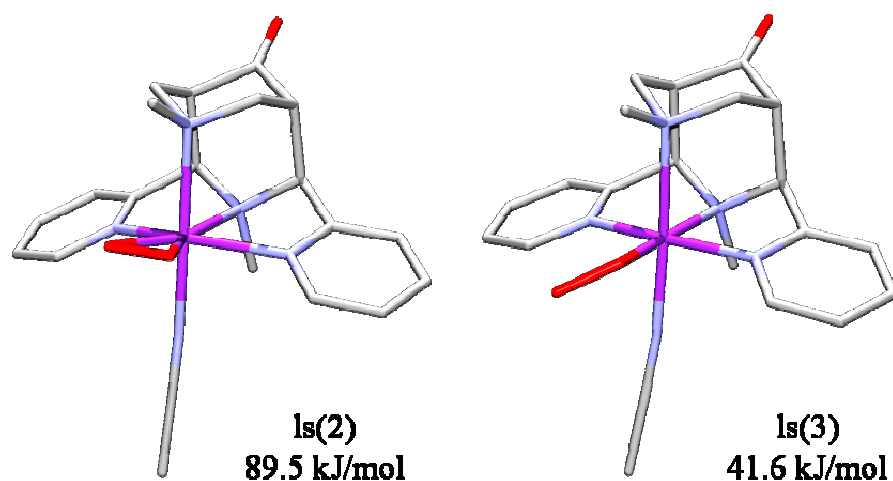


Figure 6.3. The two possible coordination modes for low-spin $[L^1Fe(O_2)]^+$, including the energies relative to the high-spin ground state

For $[L^1Fe(O_2)(H_2O)]^+$, with water coordinated *trans* to N7, only one stable structure was located, namely hs(2). In addition, the ground state, hs(2) structures of $[L^1Fe(O_2)(CH_3CN)]^+$ and $[L^1Fe(O_2)(H_2O)]^+$ are more stable than the combination of hs(1) $[L^1Fe(O_2)]^+$ and an uncoordinated acetonitrile molecule, by around 47 kJ/mol. The combination of these results suggests therefore that the ground state of the $L^1 Fe^{III}$ -peroxo species is a high-spin, heptacoordinate structure with the peroxo unit in plane with the pyridine rings and a solvent molecule coordinated in the *trans* N7 position (hs(2)). This is similar to the optimised structure found for $[L^6Fe(O_2)]^{+[9]}$.

Since a low-spin end-on species was located computationally for $[L^1Fe(O_2)(CH_3CN)]^+$, η^1 coordination of the peroxo unit was also investigated for $[L^6Fe(O_2)]^+$. A local minimum with a low-spin η^1 structure (ls(3)) is indeed located, with an energy of 41.6 kJ/mol relative to the hs(2) ground state. Note that the destabilisation of this local minimum relative to the high-spin ground state is more than 10 kJ/mol less for $[L^6Fe(O_2)]^+$ than for $[L^1Fe(O_2)(CH_3CN)]^+$. This is probably due to the shorter Fe–N7 and Fe–X bond lengths that the additional pyridine donor of L^6 induces, which stabilises the low-spin state, as well as making it more difficult to accommodate heptacoordination of the metal centre, thereby stabilising the end-on hexacoordinate minimum.

The question of the electronic nature of the high-spin η^2 species is an intriguing one, since the Mulliken spin densities are indicative of Fe^{II}-superoxo, rather than Fe^{III}-peroxo species. The Mulliken spin densities are summarised in Table 6.3 for all the calculated bispidine Fe-O₂ species and Figure 6.4 shows the spin densities of hs(1), hs(2) and ls(1) [L¹Fe(O₂)]⁺. All the η^2 high-spin species have spin densities of ~ 3.8–3.9 on the iron centre and ~ 0.5 on each oxygen atom of the peroxo unit. A comparison of the spin density distributions of [L¹Fe(O₂)(CH₃CN)]⁺ and [L⁶Fe(O₂)]⁺ in their ground states reveals also that more spin density is localised on the oxygen atoms in the L¹ complex, than the L⁶ complex. The low-spin η^2 species, on the other hand, all contain one unpaired electron located on the iron and none on the oxygen, as is to be expected for low-spin Fe^{III}.

Table 6.3. Mulliken spin densities on the iron and ligands of the LFe^{III}-peroxo species

Atoms	Fe	N7	N3	Npy1	Npy2	O1	O2	X
Complexes								
[L ¹ Fe(O ₂)] ⁺ , hs(1)	3.86	0.04	0.03	0.03	0.03	0.50	0.51	-
[L ¹ Fe(O ₂)] ⁺ , hs(2)	3.81	0.04	0.03	0.02	0.02	0.53	0.53	-
[L ¹ Fe(O ₂)] ⁺ , ls(1)	0.89	-0.01	-0.01	-0.02	-0.02	0.04	0.11	-
[L ¹ Fe(O ₂)(CH ₃ CN)] ⁺ , hs(2)	3.82	0.03	0.03	0.03	0.03	0.53	0.53	0.02
[L ¹ Fe(O ₂)(CH ₃ CN)] ⁺ , ls(2)	1.15	-0.02	0.03	0.03	0.03	-0.09	-0.09	-0.01
[L ¹ Fe(O ₂)(CH ₃ CN)] ⁺ , ls(3)	0.01	0.00	0.00	0.00	0.00	0.41	0.58	0.00
[L ¹ Fe(O ₂)(H ₂ O)] ⁺ , hs(2)	3.98	0.05	0.03	0.04	0.04	0.44	0.39	0.03
[L ¹ Fe(O ₂)] ⁺ , hs(2)	3.93	0.04	0.03	0.04	0.03	0.45	0.45	0.05
[L ¹ Fe(O ₂)] ⁺ , ls(3)	0.05	0.00	0.00	0.00	0.00	0.410	0.54	0.00

The spin density distribution in the two end-on low-spin structures is also significantly different to the side-on low-spin complexes, with the bulk of the spin localised on the O₂ unit and practically no spin on the iron centre. This is again indicative of Fe^{II}-superoxo, rather than Fe^{III}-peroxo. Here the spin density distribution within the O₂ unit is also asymmetrical, with less spin on the iron-bound oxygen atom, and there is a clear distinction between the two binding modes. The spin density distribution in the high-spin η^2 and low-spin η^1 structures of [L⁶Fe(O₂)]⁺ are also shown in Figure 6.4.

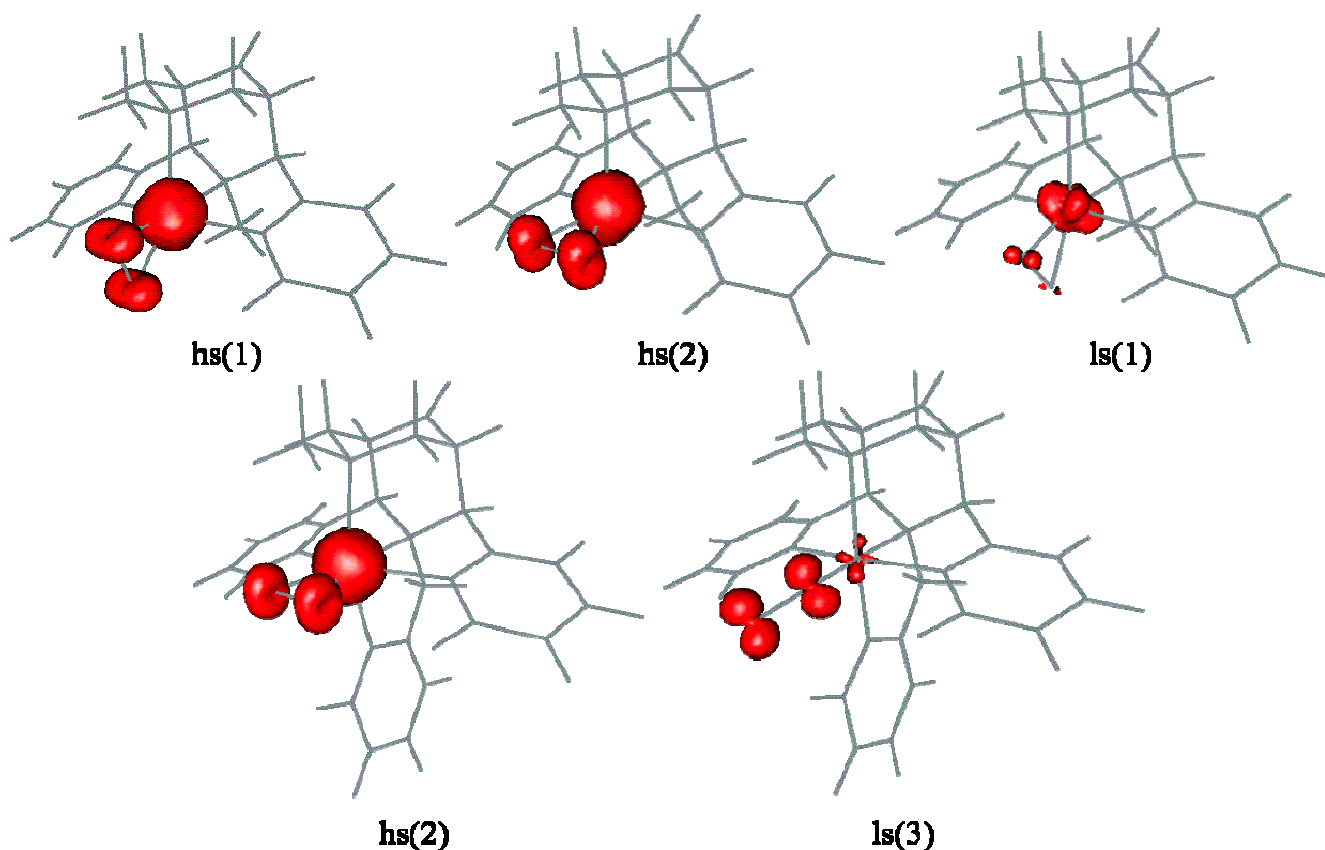


Figure 6.4. Spin densities of the $[L^1Fe(O_2)]^+$ and $[L^6Fe(O_2)]^+$ species in their different coordination modes

Further indication for the electronic nature of the high-spin bispidine Fe-O₂ complexes can be sought in the bond lengths and stretching frequencies of the O–O bond, since, as discussed in the Introduction, both these properties are often used to define the nature of metal-O₂ adducts. Comparing the calculated O–O bond lengths and stretching frequencies of the bispidine systems (see Table 6.4) to the quoted ranges for peroxo and superoxo species respectively reveals that they lie neither in the superoxo nor the peroxo range, but somewhere inbetween, with bond lengths closer to the peroxo range and the frequencies closer to the superoxo range. However, this classification is based on experimentally observed bond lengths and frequencies and it is known that DFT tends to overestimate the bond lengths in transition metal complexes. The actual O–O bond lengths may be somewhat shorter than the calculated ones, bringing them closer to the region of a superoxide. Comparing the bond lengths and stretching frequencies of the bound O₂ units to those of the unbound peroxo and superoxo

species, reveals also that they are much closer to those of superoxide than those of the peroxide. This is demonstrated graphically in Figure 6.5.

One exception is the high-spin $[L^1Fe(O_2)(H_2O)]^+$ species, which has the longest bond length and smallest stretching frequency of all the calculated complexes and therefore lies just outside the peroxo region. This can be attributed however, to a weak hydrogen bond between one of the oxygen atoms of the peroxo species and one of the hydrogen atoms of the coordinated water molecule ($O_{\text{peroxo}} \cdots H_{\text{aqua}} = 2.065 \text{ \AA}$), which weakens the O–O bond and therefore increases the bond length. The Mulliken spin densities in this complex are also the highest on the iron and the lowest on the O_2 unit of all the high-spin Fe– O_2 complexes.

Table 6.4. O–O bond lengths and frequencies of the free and Fe-bispidine O_2 species

Ligand	Bond length (Å)	Frequency (cm^{-1})
Parameters		
Dioxygen species		
O_2	1.215	1626.8
O_2^-	1.353	1188.3
O_2^{2-}	1.618	659.4
Complexes		
$[L^1Fe(O_2)]^+$, hs(1)	1.390	998.44
$[L^1Fe(O_2)]^+$, hs(2)	1.373	1043.24
$[L^1Fe(O_2)]^+$, ls(1)	1.414	942.75
$[L^1Fe(O_2)(CH_3CN)]^+$, hs(2)	1.371	1044.91
$[L^1Fe(O_2)(CH_3CN)]^+$, ls(2)	1.397	1019.32
$[L^1Fe(O_2)(CH_3CN)]^+$, ls(3)	1.321	1197.36
$[L^1Fe(O_2)(H_2O)]^+$, hs(2)	1.420	937.36
$[L^1Fe(O_2)]^+$, hs(2)	1.410	945.79
$[L^1Fe(O_2)]^+$, ls(3)	1.328	1176.68

In contrast to the above considerations, which support a superoxo assignment, the experimental O–O stretching frequency of $[L^6Fe(O_2)]^+$, at 827 cm^{-1} , is significantly lower than the calculated frequency of 946 cm^{-1} . This suggests that the calculated bond strengths are overestimated and that the actual frequencies are lower (and bond lengths correspondingly

longer), bringing them closer again to the peroxo range. The absorption spectrum of $[L^6Fe(O_2)]^+$ has also been measured in methanol and is indicative of an Fe^{III} , rather than an Fe^{II} complex, which supports this view.

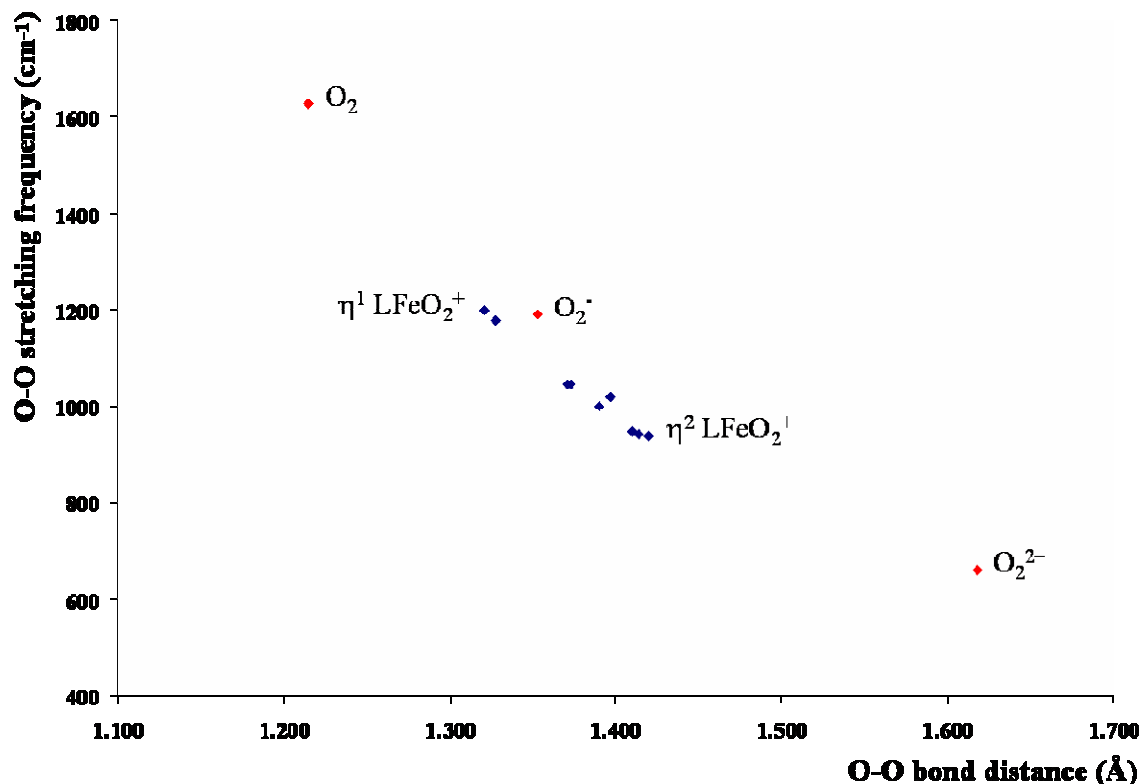


Figure 6.5. Plot of O–O stretching frequencies vs. O–O bond lengths (calculated) for O₂, O₂⁻, O₂²⁻ and the bispidine FeO₂ complexes

The above discussion is based on the assumption that a continuum exists between the peroxo and superoxo states. McGrady and Pantazis argue against this view, stating that peroxide and superoxide are fundamentally different states, both in symmetry and in multiplicity, and that a continuum between the two is therefore not possible^[16]. According to this view, the amount of spin donation from the O₂ unit to the metal centre is not the deciding factor on determining the electronic structure of metal, nor, by implication, are the O–O bond lengths and stretching frequencies.

Figure 6.6 shows the molecular orbitals (MO's) responsible for the interaction between the iron centre and the O₂ ligand, for the high-spin side-on and low-spin end-on states of $[L^6Fe(O_2)]^+$. For high-spin side-on $[L^6Fe(O_2)]^+$, we define our coordinate system so that the

Fe–N7 bond lies approximately along the z-axis, the Fe–N_{py} bonds along the x-axis and the y-axis runs through the Fe and the centre of the O–O bond. The main interaction between the O₂ unit and the iron centre occurs via mixing of the Fe(d_{xy}) orbital and the in-plane π* orbital (π_{in}* in Figure 6.6) and the Fe(d_{xz}) orbital and the out-of-plane π* orbital (π_{out}* in Figure 6.6), forming two pairs of bonding and antibonding orbitals. Beginning from a high-spin Fe^{III} centre and a peroxo unit, the two bonding MO's formed from the interactions described above would be doubly occupied and the two antibonding MO's (the homo and the homo-1 respectively) singly occupied with electrons of parallel spin, leading to a electronic ground state with a total spin of S=5/2. However, beginning from a high-spin Fe^{II} centre and a superoxo unit, the double occupation of highest energy bonding orbital described above, requires that the unpaired electron of the superoxo unit, occupying the in-plane π* orbital, have the opposite spin to the unpaired electron occupying the Fe(d_{xy}) orbital, leading to an electronic ground state with a total spin of S=3/2. In other words, a continuum exists between high-spin Fe^{II}-superoxo and intermediate-spin Fe^{III}-peroxo, which have the same multiplicity, but not between high-spin Fe^{II}-superoxo and high-spin Fe^{III}-peroxo, which have different multiplicities. This implies that the high-spin bispidine complexes described above are Fe^{III}-peroxo complexes, regardless of the amount of spin donation from the peroxo unit to the iron centre (which simply implies a highly covalent interaction).

For low-spin end-on [L⁶Fe(O₂)]⁺, the d-orbital manifold is shifted, so that it is no longer aligned with the metal–bispidine bonds, making the assignment of individual d-orbitals difficult. A tentative assignment is given in Figure 6.6. The main interaction occurs via mixing of the Fe(d_{xy}) orbital and the out-of-plane π* orbital (π_{out}*), forming a bonding (homo-4) and an antibonding (homo) pair of molecular orbitals. In both the Fe^{III}-peroxo and Fe^{II}-superoxo extremes, the single unpaired electron is located in the antibonding MO described above and the resulting electronic states have the same multiplicity, so that a continuum may exist between them. Combined with the Mulliken spin density distribution, this continuity implies that the low-spin end-on [L⁶Fe(O₂)]⁺ state is, in fact, best described as an Fe^{II}-superoxo complex.

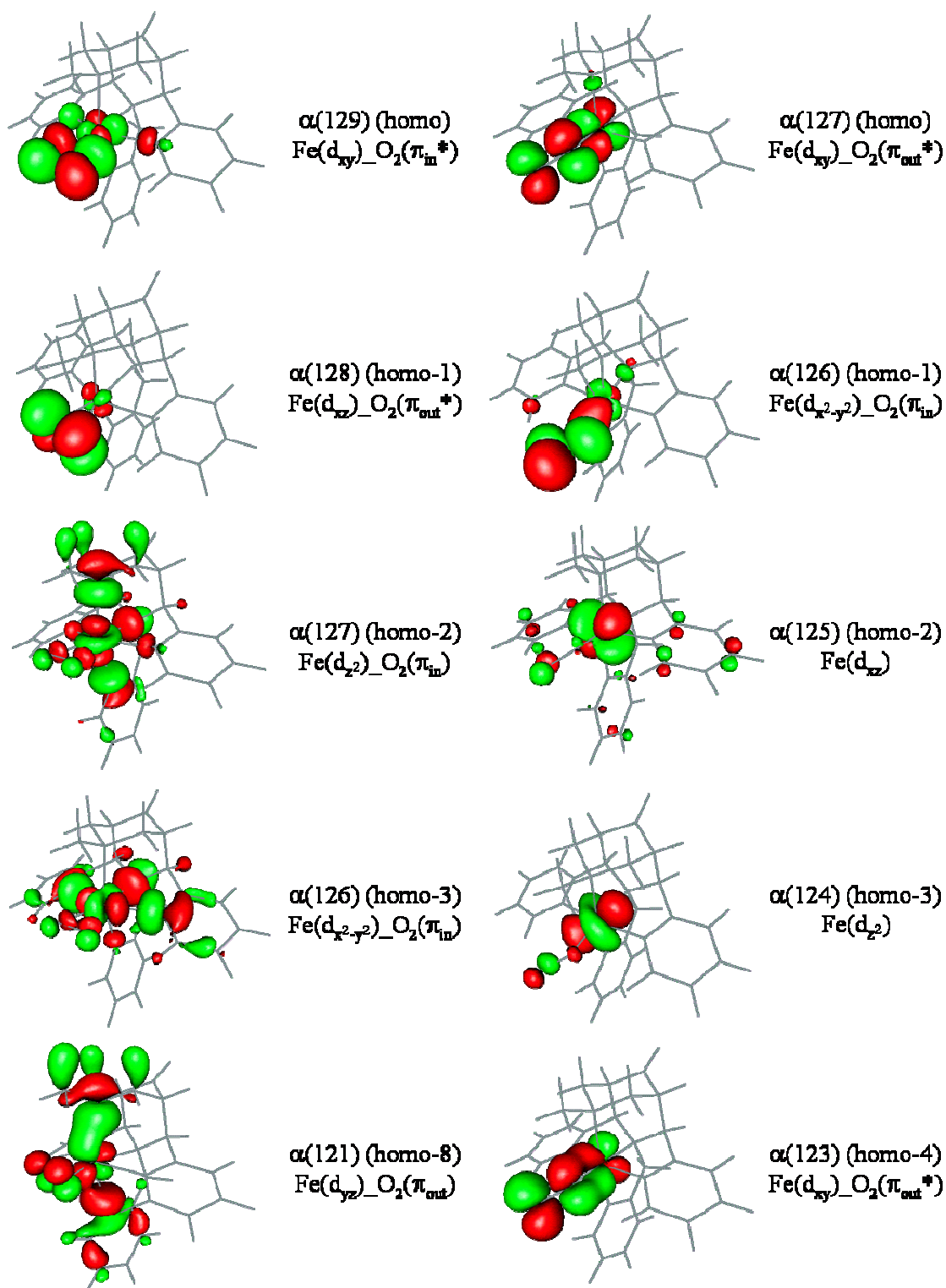


Figure 6.6. The molecular orbitals involved in the interaction of the iron centre and O₂ in high-spin side-on and low-spin end-on [L⁶Fe(O₂)]⁺

6.4. Conclusions

The ground state of the $LFeO_2^+$ complex of L^1 is a high-spin seven-coordinate species with the O_2 unit in plane with the pyridine rings and a solvent molecule coordinated in the *trans* N7 position, similar to the calculated ground state of $[L^6Fe(O_2)]^{+[9]}$. Mulliken spin densities, O–O bond lengths and O–O stretching frequencies suggest that the Fe^{III} -peroxo complexes of L^1 have significant Fe^{II} -superoxo character, but arguments based on symmetry and multiplicity support the view of an Fe^{III} -peroxo species with a high degree of covalency in the Fe– O_2 bonding. Regardless of the classification as superoxo or peroxo however, the significant result remains the same, namely that a large amount of spin density is localised on the O_2 unit of these complexes.

In addition to the side-on Fe^{III} -peroxo binding mode, end-on low-spin local minima have also been located for $[L^6Fe(O_2)]^+$ and $[L^1Fe(O_2)(CH_3CN)]^+$, and these can be unambiguously classified as Fe^{II} -superoxo complexes on the basis of the Mulliken spin densities and symmetry and multiplicity arguments. This is in contrast to the side-on low-spin complexes, which are clearly Fe^{III} -peroxo species.

A comparison of the spin density and the molecular orbital array shows that the spin on the O_2 unit in the high-spin complexes is mainly due to the charge transfer from O_2 to the iron centre via two molecular orbitals composed of the antibonding combination of the $Fe(d_{xy})$ and $Fe(d_{xz})$ orbitals with the in-plane and out-of-plane $O_2(\pi^*)$ orbitals respectively. The spin on the O_2 unit in the low-spin end-on complexes is due to a single molecular orbital, which is the antibonding combination of an $Fe(d_{xy})$ and an out-of-plane $O_2(\pi^*)$ orbital, as one would expect for a system with a single unpaired electron.

6.5. References

- ¹ J.S. Valentine, *Chem. Rev.*, **1973**, 73, 235
- ² C.J. Cramer, W.B. Tolman, K.H. Theopold and A.L. Rheingold, *PNAS*, **2003**, 100, 3635
- ³ M. Sono, M.P. Roach, E.D. Coulter, J.H. Dawson, *Chem. Rev.*, **1996**, 96, 2841
- ⁴ L. Que, Jr, R.Y.N. Ho, *Chem. Rev.*, **1996**, 96, 2607; E.I. Solomon, T.C. Brunold, M.I. Davis, J.N. Kemsley, S-K. Lee, N. Lehnert, F. Neese, A.J. Skulan, Y-S. Yang, J. Zhou, *Chem. Rev.*, **2000**, 100, 235
- ⁵ K.L. Cheng, P.F. Lott, *Anal. Chem.*, **1956**, 28, 462
- ⁶ C. Walling, M. Kurz, H.J. Schugar, *Inorg. Chem.*, **1970**, 9, 931
- ⁷ G.J. McClune, J.A. Fee, G.A. McClusky, J.T. Groves, *J. Am. Chem. Soc.*, **1977**, 99, 5220
- ⁸ G. Roelfes, V. Vrajmasu, K. Chen, R.Y.N. Ho, J-U. Rohde, C. Zondervan, R.M. la Crois, E.P. Schudde, M. Lutz, A.L. Spek, R. Hage, B.L. Feringa, E. Munck, L. Que, Jr., *Inorg. Chem.*, **2003**, 42, 2639; A.J. Simaan, S. Döpner, F. Banse, S. Bourcier, G. Bouchoux, A. Boussac, P. Hildebrandt, J-J. Girerd, *Eur. J. Inorg. Chem.*, **2000**, 1627; Y. Zang, J. Kim, Y. Dong, E.C. Wilkinson, E.H. Appelman, L. Que, Jr., *J. Am. Chem. Soc.*, **1997**, 119, 4197; A.J. Simaan, F. Banse, J-J. Girerd, K. Wieghart and B. Eckhard, *Inorg. Chem.*, **2001**, 40, 6538
- ⁹ M.R. Bukowski, P. Comba, C. Limberg, M. Merz, L. Que, Jr., T. Wistuba, *Angew. Chem. Int. Ed.*, **2004**, 43, 1283
- ¹⁰ Jochen Bautz, *PhD Thesis*, Ruprecht-Karls Universität Heidelberg, **2006**
- ¹¹ J. Bautz, P. Comba and L. Que, Jr., *Inorg. Chem.*, *submitted*
- ¹² *Gaussian 03, Revision B.03*, M. J. Frisch, G. W. Trucks, H. B. Schlegel, G. E. Scuseria, M. A. Robb, J. R. Cheeseman, J. A. Montgomery, Jr., T. Vreven, K. N. Kudin, J. C. Burant, J. M. Millam, S. S. Iyengar, J. Tomasi, V. Barone, B. Mennucci, M. Cossi, G. Scalmani, N. Rega, G. A. Petersson, H. Nakatsuji, M. Hada, M. Ehara, K. Toyota, R. Fukuda, J. Hasegawa, M. Ishida, T. Nakajima, Y. Honda, O. Kitao, H. Nakai, M. Klene, X. Li, J. E. Knox, H. P. Hratchian, J. B. Cross, C. Adamo, J. Jaramillo, R. Gomperts, R. E. Stratmann, O. Yazyev, A. J. Austin, R. Cammi, C. Pomelli, J. W. Ochterski, P. Y. Ayala, K. Morokuma, G. A. Voth, P. Salvador, J. J. Dannenberg, V. G. Zakrzewski, S. Dapprich, A. D. Daniels, M. C. Strain, O. Farkas, D. K. Malick, A. D. Rabuck, K. Raghavachari, J. B. Foresman, J. V. Ortiz, Q. Cui, A. G. Baboul, S. Clifford, J. Cioslowski, B. B. Stefanov, G. Liu, A. Liashenko, P. Piskorz, I. Komaromi, R. L. Martin, D. J. Fox, T. Keith, M. A. Al-Laham, C. Y. Peng, A. Nanayakkara, M. Challacombe, P. M. W. Gill, B. Johnson, W. Chen, M. W. Wong, C. Gonzalez, and J. A. Pople, *Gaussian, Inc., Pittsburgh PA, 2003*

¹³ A.D.J. Becke, *J. Chem. Phys. B*, **1993**, 98, 5648; C. Lee, W. Yang, R.G. Parr, *Phys. Rev. B*, **1988**, 37, 785

¹⁴ A. Schäfer, C. Huber and R. Ahlrichs, *J. Chem. Phys.*, **1994**, 100, 5829

¹⁵ M.T. Cancès, B. Mennucci and J. Tomasi, *J. Chem. Phys.*, **1997**, 107, 3032; M. Cossi, V. Barone, B. Mennucci and J. Tomasi, *Chem. Phys. Lett.*, **1998**, 286, 253; B. Mennucci and J. Tomasi, *J. Chem. Phys.*, **1997**, 106, 5151; M. Cossi, G. Scalmani, N. Rega and V. Barone, *J. Chem. Phys.*, **2002**, 117, 43

¹⁶ P.R. Howe, J.E. McGrady and C.J. McKenzie, *Inorg. Chem.*, **2002**, 41, 2026; D.A. Pantazis and J.E. McGrady, *Inorg. Chem.*, **2003**, 42, 7734

Addendum A:
**Calculated geometries of possible intermediates in the
reaction of L¹ with H₂O₂**

Table A1. Calculated geometries of $[L^1Fe^{II}(HOOH)]^{2+}$, $[L^1Fe^{II}(HOOH)(CH_3CN)]^{2+}$ and $[L^1Fe^{II}(HOOH)(H_2O)]^{2+}$, for S=0, 1, 2

Complex Parameter	$[L^1Fe(HOOH)]^{2+}$			$[L^1Fe(HOOH)(CH_3CN)]^{2+}$			$[L^1Fe(HOOH)(H_2O)]^{2+}$		
	S=0	S=1	S=2	S=0	S=1	S=2	S=0	S=1	S=2
Bond distances (Å)									
Fe-N7	2.056	2.272	2.189	2.208	2.559	2.377	2.153	2.466	2.317
Fe-N3	1.960	1.980	2.164	2.010	2.040	2.206	1.993	1.990	2.195
Fe-Npy1	1.994	2.020	2.126	2.013	1.986	2.160	1.999	2.016	2.160
Fe-Npy2	1.993	2.017	2.124	2.004	1.980	2.159	1.997	2.015	2.151
Fe-O4	2.204	2.005	2.216	2.067	2.157	2.232	2.077	2.040	2.349
Fe...O5	2.147	2.818	2.878	3.065	3.156	3.173	3.040	3.063	3.298
Fe-X	-	-	-	1.928	2.132	2.187	2.060	2.334	2.173
N3...N7	2.847	2.956	3.034	2.913	3.041	3.031	2.892	3.006	3.016
N1...N2	3.955	3.948	4.101	3.986	3.938	4.220	3.964	3.997	4.204
O4-O5	1.455	1.468	1.454	1.462	1.457	1.452	1.473	1.479	1.456
O5...H _x	-	-	-	-	-	-	1.905	2.083	1.959
Valence angles (°)									
N3-Fe-N7	90.25	87.80	88.35	87.23	81.97	82.71	88.39	84.13	83.86
Npy1-Fe-Npy2	165.53	155.93	149.61	165.89	166.32	155.41	165.55	165.01	154.29
N7-Fe-O4	116.60	97.44	108.23	91.51	84.48	91.78	92.48	90.04	92.48
N7-Fe-X	-	-	-	175.88	167.83	174.58	174.23	169.24	166.83
N3-Fe-O4	152.82	174.11	162.30	173.43	164.96	174.16	175.81	172.76	174.45
Fe-O4-O5	68.36	107.45	101.29	119.62	120.44	117.31	116.79	120.19	118.32
Torsion angles (°)									
N3-C-C-Npy1	38.52	31.27	36.02	38.27	33.57	39.14	37.73	33.57	38.65
N3-C-C-Npy2	-38.49	-31.87	-36.69	-38.04	-33.04	-38.43	-38.81	-33.53	-37.96
N7-Fe-O4-O5	175.42	162.27	148.98	123.31	103.45	128.50	151.72	144.41	154.88
Relative Energy (kJ/mol)									
Solvent	65.88	45.73	0.00	47.41	63.70	0.00	63.59	71.36	0.00

Table A2. Calculated geometries of [L¹Fe^{II}(OOH)]⁺, [L¹Fe^{II}(OOH)(CH₃CN)]⁺ and [L¹Fe^{II}(OOH)(H₂O)]⁺, for S=0, 1, 2

Complex Parameter	[L ¹ Fe(OOH)] ⁺			[L ¹ Fe(OOH)(CH ₃ CN)] ⁺			[L ¹ Fe(OOH)(H ₂ O)] ⁺	
	S=0	S=1	S=2	S=0	S=1	S=2	S=1	S=2
Bond distances (Å)								
Fe-N7	2.091	2.340	2.256	2.222	2.475	2.411	2.155	2.360
Fe-N3	2.012	2.039	2.284	2.057	2.060	2.315	2.033	2.286
Fe-Npy1	1.961	1.997	2.168	1.987	1.993	2.168	1.974	2.160
Fe-Npy2	1.953	1.969	2.158	1.975	1.980	2.172	1.971	2.174
Fe-O1	1.903	1.795	1.897	1.896	1.815	1.902	1.914	1.916
Fe...O2	2.021	2.796	2.417	2.849	2.853	2.777	2.830	2.815
Fe-X	-	-	-	1.896	2.546	2.238	2.056	2.296
N3...N7	2.872	2.979	3.017	2.940	3.008	3.023	2.918	3.015
N1...N2	3.882	3.913	4.131	3.930	3.936	4.186	3.912	4.184
O1-O2	1.482	1.475	1.484	1.483	1.478	1.472	1.500	1.479
O2...H _x	-	-	-	-	-	-	1.620	1.746
Valence angles (°)								
N3-Fe-N7	88.81	85.45	83.28	86.71	82.55	79.31	88.31	80.89
Npy1-Fe-Npy2	165.04	161.28	145.44	165.52	164.39	149.36	165.30	149.79
N7-Fe-O1	108.41	103.28	107.61	88.06	95.86	94.68	90.11	95.96
N7-Fe-X	-	-	-	176.18	177.78	175.25	174.57	174.69
N3-Fe-O1	162.77	169.01	167.83	171.91	171.00	170.22	176.56	176.68
Fe-O1-O2	72.12	117.15	90.45	114.45	119.72	110.18	111.44	111.43
Torsion angles (°)								
N3-C-C-Npy1	38.43	35.82	34.79	38.35	35.00	-38.46	38.50	-38.78
N3-C-C-Npy2	-38.65	-34.53	-37.90	-38.91	-34.66	37.87	-39.55	38.42
N7-Fe-O1-O2	176.61	69.38	158.28	137.48	116.56	129.94	152.59	148.71
Relative Energy (kJ/mol)								
Solvent	68.44	34.61	0.00	65.88	48.74	0.00	46.26	0.00

Table A3. Calculated geometries of [L¹Fe^{III}(OOH)]²⁺, [L¹Fe^{III}(OOH)(CH₃CN)]²⁺ and [L¹Fe^{III}(OOH)(H₂O)]²⁺, for S=1/2, 3/2, 5/2

Complex Parameter	[L ¹ Fe(OOH)] ²⁺			[L ¹ Fe(OOH)(CH ₃ CN)] ²⁺			[L ¹ Fe(OOH)(H ₂ O)] ²⁺		
	S=1/2	S=3/2	S=5/2	S=1/2	S=3/2	S=5/2	S=1/2	S=3/2	S=5/2
Bond distances (Å)									
Fe-N7	2.059	2.196	2.123	2.181	2.340	2.300	2.131	2.334	2.252
Fe-N3	2.023	2.014	2.173	2.056	2.035	2.233	2.041	2.026	2.214
Fe-Npy1	1.980	2.022	2.115	1.992	2.026	2.141	1.992	2.041	2.142
Fe-Npy2	1.993	2.017	2.113	1.996	2.012	2.133	1.999	2.030	2.126
Fe-O1	1.804	1.760	1.829	1.775	1.777	1.852	1.790	1.784	1.862
Fe...O2	2.016	2.559	2.805	2.761	2.737	2.856	2.740	2.734	2.841
Fe-X	-	-	-	1.951	2.415	2.216	2.024	2.284	2.201
N3...N7	2.854	2.957	3.020	2.915	2.968	3.003	2.898	2.955	2.998
N1...N2	3.918	3.915	4.035	3.945	3.986	4.155	3.944	4.025	4.148
O1-O2	1.462	1.450	1.416	1.442	1.438	1.414	1.460	1.450	1.428
O2...H _x	-	-	-	-	-	-	1.753	1.941	1.898
Valence angles (°)									
N3-Fe-N7	88.71	89.15	89.36	86.88	85.13	82.97	87.95	85.01	84.34
Npy1-Fe-Npy2	160.91	151.52	145.21	162.97	161.60	152.88	162.48	162.92	152.66
N7-Fe-O1	105.48	93.66	111.55	86.75	94.00	92.91	89.36	93.25	95.73
N7-Fe-X	-	-	-	177.86	179.22	177.68	176.06	175.84	178.11
N3-Fe-O1	165.80	176.94	159.09	173.16	172.16	175.79	175.77	173.29	179.93
Fe-O1-O2	75.41	105.32	119.13	117.86	94.00	121.42	114.50	115.11	118.82
Torsion angles (°)									
N3-C-C-Npy1	37.01	32.00	35.66	37.34	34.82	38.276	37.17	35.87	37.88
N3-C-C-Npy2	-37.55	-31.85	-36.22	-38.06	-34.45	-38.87	-39.03	-35.97	-40.07
N7-Fe-O1-O2	175.86	-173.47	172.58	154.10	81.52	143.88	155.45	135.93	152.50
Relative Energy (kJ/mol)									
Solvent	9.50	0.00	0.89	2.31	12.37	0.00	10.94	12.55	0.00

Table A4. Calculated geometries of $[\text{L}^1\text{Fe}^{\text{IV}}(\text{O})]^{2+}$, $[\text{L}^1\text{Fe}^{\text{IV}}(\text{O})(\text{CH}_3\text{CN})]^{2+}$, $[\text{L}^1\text{Fe}^{\text{IV}}(\text{O})(\text{H}_2\text{O})]^{2+}$, $[\text{L}^1\text{Fe}^{\text{IV}}(\text{O})(\text{OH})]^+$ for S=0, 1, 2

Complex Parameter	$[\text{L}^1\text{Fe}(\text{O})]^{2+}$			$[\text{L}^1\text{Fe}(\text{O})(\text{CH}_3\text{CN})]^{2+}$		$[\text{L}^1\text{Fe}(\text{O})(\text{H}_2\text{O})]^{2+}$		$[\text{L}^1\text{Fe}(\text{O})(\text{OH})]^+$	
	S=0	S=1	S=2	S=1	S=2	S=1	S=2	S=1	S=2
Bond distances (Å)									
Fe-N7	2.035	2.040	2.184	2.148	2.321	2.099	2.281	2.295	2.363
Fe-N3	2.123	2.030	2.056	2.105	2.097	2.100	2.082	2.133	2.200
Fe-Npy1	1.978	2.000	2.002	1.987	2.036	1.990	2.032	1.984	2.202
Fe-Npy2	1.978	2.000	2.002	1.987	2.036	1.987	2.030	1.983	2.202
Fe-O1	1.560	1.579	1.614	1.621	1.613	1.617	1.615	1.615	1.615
Fe-X	-	-	-	1.980	2.302	2.069	2.335	1.849	1.808
N3...N7	2.868	2.868	2.991	2.922	2.975	2.920	2.969	2.961	2.958
N1...N2	3.782	3.937	3.888	3.929	4.015	3.928	4.002	3.922	4.294
O5...H _x	-	-	-	-	-	2.483	2.550		2.448
Valence angles (°)									
N3-Fe-N7	87.18	89.61	89.66	86.77	84.49	88.12	85.64	83.84	80.74
Npy1-Fe-Npy2	146.00	159.48	152.25	162.85	160.89	161.94	160.17	162.74	154.39
N7-Fe-O1	105.86	118.00	101.34	91.16	93.48	93.54	95.31	91.19	91.61
N7-Fe-X	-	-	-	179.73	178.88	178.13	177.92	172.31	172.28
N3-Fe-O1	166.96	152.39	169.00	177.93	177.97	178.34	179.05	175.03	172.34
Torsion angles (°)									
N3-C-C-Npy1	32.83	38.04	33.99	39.22	36.88	39.34	36.61	38.78	43.37
N3-C-C-Npy2	-32.83	-38.04	-33.99	-39.22	-36.89	-40.38	-37.03	-38.77	-43.37
Relative Energy (kJ/mol)									
Solvent	110.67	24.99	0.00	0.50	0.00	14.23	0.00	21.00	0.00

Table A5. Calculated geometries of $[L^1Fe^{IV}(OH)_2]^{2+}$, for S=0, 1, 2

Complex	$[L^1Fe(OH)_2]^{2+}$		
Parameter	S=0	S=1	S=2
Bond distances (Å)			
Fe-N7	2.378	2.231	2.253
Fe-N3	2.036	2.063	2.143
Fe-Npy1	1.985	1.988	2.171
Fe-Npy2	1.975	1.987	2.194
Fe-O1	1.726	1.750	1.766
Fe-O2	1.720	1.782	1.771
N3...N7	2.909	2.919	2.935
Npy1...Npy2	3.934	3.926	4.260
Valence angles (°)			
N3-Fe-N7	82.06	85.57	83.75
Npy1-Fe-Npy2	166.99	162.10	154.83
N7-Fe-O1	82.06	86.73	87.15
N7-Fe-O2	174.34	177.12	178.51
N3-Fe-O1	163.70	172.28	170.82
N3-Fe-O2	92.78	94.99	94.94
Torsion angles (°)			
N3-C-C-Npy1	34.26	37.55	40.98
N3-C-C-Npy2	-34.87	-36.57	-40.84
Relative Energy (kJ/mol)			
Solvent	98.10	0.00	11.24

Table A6. Calculated geometries of $[\text{L}^1\text{Fe}^{\text{V}}(\text{O})]^{3+}$, $[\text{L}^1\text{Fe}^{\text{V}}(\text{O})(\text{CH}_3\text{CN})]^{3+}$, $[\text{L}^1\text{Fe}^{\text{V}}(\text{O})(\text{H}_2\text{O})]^{3+}$ and $[\text{L}^1\text{Fe}^{\text{V}}(\text{O})(\text{OH})]^{2+}$, for $S=3/2$

Complex	$[\text{L}^1\text{Fe}(\text{O})]^{3+}$	$[\text{L}^1\text{Fe}(\text{O})(\text{CH}_3\text{CN})]^{3+}$	$[\text{L}^1\text{Fe}(\text{O})(\text{H}_2\text{O})]^{3+}$	$[\text{L}^1\text{Fe}(\text{O})(\text{OH})]^{2+}$
Parameter	S=3/2	S=3/2	S=3/2	S=3/2
Bond distances (Å)				
Fe–N7	2.057	2.154	2.121	2.255
Fe–N3	2.026	2.068	2.111	2.094
Fe–Npy1	1.962	1.962	1.993	1.980
Fe–Npy2	1.962	1.962	2.002	1.980
Fe–O4	2.597	1.640	1.612	1.623
Fe–X	-	2.006	2.055	1.767
N3···N7	2.914	2.926	2.946	2.935
Npy1···Npy2	3.827	3.892	3.945	3.928
Valence angles (°)				
N3–Fe–N7	91.10	87.74	88.25	84.77
Npy1–Fe–Npy2	154.43	165.19	162.00	165.52
N7–Fe–O4	116.92	90.79	92.53	90.85
N7–Fe–X	-	178.39	177.93	173.93
N3–Fe–O4	151.98	178.52	179.11	175.63
N3–Fe–X	-	93.88	91.45	89.15
Torsion angles (°)				
N3–C–C–Npy1	35.82	39.48	38.06	40.22
N3–C–C–Npy2	-35.81	-39.48	-39.08	-40.22